THE INFLUENCE OF COASTAL WETLANDS ON HURRICANE

SURGE AND DAMAGE WITH APPLICATION TO PLANNING

UNDER CLIMATE CHANGE

A Dissertation

by

CELSO MOLLER FERREIRA

Submitted to the Office of Graduate Studies of
Texas A&M University
in partial fulfillment of the requirements for the degree of

DOCTOR OF PHILOSOPHY

August 2012

Major Subject: Civil Engineering

The Influence of Coastal Wetlands on Hurricane Surge and Damage with Application to

Planning under Climate Change

THE INFLUENCE OF COASTAL WETLANDS ON HURRICANE

SURGE AND DAMAGE WITH APPLICATION TO PLANNING

UNDER CLIMATE CHANGE

A Dissertation

by

CELSO MOLLER FERREIRA

Submitted to the Office of Graduate Studies of
Texas A&M University
in partial fulfillment of the requirements for the degree of

DOCTOR OF PHILOSOPHY

Approved by:

Co-Chairs of Committee,	Francisco Olivera
	Jennifer L. Irish
Committee Members,	Anthony Cahill
	Emily Zechman
	Steven Quiring
Head of Department,	John Niedzwecki

August 2012

Major Subject: Civil Engineering

ABSTRACT

The Influence of Coastal Wetlands on Hurricane Surge and Damage with Application to

Planning under Climate Change.

(August 2012)

Celso Moller Ferreira, B.S., Federal University of Santa Catarina; M.Sc., Federal

University of Santa Catarina; M.E., Centro de Estudios y Experimentación de Obras

Públicas

Co-Chairs of Advisory Committee: Dr. Francisco Olivera
                                 Dr. Jennifer L. Irish

Coastal storm surges from hurricanes are one of the most costly natural disasters in the

United States (US). Current research arguably indicates a mean sea-level (MSL) increase

due to global warming, as well as an increase in damages caused by hurricanes under

climate change. The objectives of this research are: 1) to develop a framework that

integrates Geographical Information Systems (GIS) with hurricane storm surge

numerical models; 2) to quantify the uncertainty derived from coastal land cover spatial

data on hurricane storm surge; and 3) to investigate the potential impacts of SLR

changes on land cover to hurricane storm surge and coastal damages.

Numerical analysis is an important tool for predicting and simulating storm surges for

coastal structure design, planning and disaster mitigation. Here we proposed a

framework to integrate Geographical Information Systems (GIS) with computational

fluid dynamic (CFD) models used to simulate hurricane storm surge. The geodatamodel "Arc StormSurge" is designed to store geospatial information for hurricane storm surge modeling and GIS tools are designed to integrate the high performance computing (HPC) input and output files to GIS; pre-process geospatial data and post-process model results, thereby, streamlining the delineation of coastal flood maps.

Georeferenced information of land cover is used to define the frictional drag at the sea bottom and to infer modifications to the momentum transmitted to the water column by the winds. We investigated uncertainties in the surge response arising from land cover for Texas central bays considering several land cover datasets. The uncertainties were quantified based on the mean maximum surge response and inundated area extent.

Considering projected SLR, wetland composition and spatial distribution are also expected to change with coastal environmental conditions. Our results showed that wetland degradation by SLR increased the mean maximum surge for coastal bays. Direct damage to buildings and businesses was also significantly increased by the loss of wetlands due to SLR. Here, we demonstrated the importance of considering the effects of land cover and SLR to hurricane storm surge simulations for coastal structure design, floodplain delineation or coastal planning.

DEDICATION

This dissertation is dedicated to the woman of my life.

ACKNOWLEDGEMENTS

NOMENCLATURE

ADCIRC	Advanced Circulation model
ANOVA	Analysis of Variance
C-CAP	Coastal Change Analyses Program
DFIRM	Digital Flood Insurance Rate Maps
EDC	EROS Data Center
ETM	Enhanced Thematic Mapper
FEMA	Federal Emergency Management Agency
FIA	Federal Insurance Administration
GAP	Gap Analyses Program
GIS	Geographical Information Systems
HAZUS	Hazards US Multi Hazard
HPC	High Performance Computing
IPCC	International Panel on Climate Change
MSL	Mean Sea-level
NAVD	National Vertical Datum
NLCD	National Land Cover Dataset
NOAA	National Oceanic and Atmosphere Administration
NRC	National Research Council
NWI	National Wetlands Inventory
PBL	Planetary Boundary Layer

RMSE	Root Mean Square Error
SLR	Sea-level Rise
SWAN	Simulating Waver Near Shore
US	United States
USACE	United States Army Corps of Engineering
USGS	United States Geological Survey
ζ_{mmsa}	Mean maximum surge neglecting land cover effects
V_f	Hurricane forward speed
υ_{mmsa}	Mean maximum surge increment due to land cover effects
h	Water depth
t	Time
ζ	Surge elevation above mean sea-level
$\vec{U}$	Depth-averaged horizontal velocity vector
p	Barometric pressure
f	Coriolis force
$\vec{k}$	Vertical unit vector
τ_s	Free-surface shear stress
τ_b	Bottom shear stress
τ_w	Wave radiation stress
ρ	Water density
N	Wave action density spectrum
C_g	Wave group velocity

C_σ	Propagation velocity
σ	Relative frequency
θ	Wave direction
C_θ	Wave propagation velocity
S_{tot}	Wave growth caused by the wind
C	Current velocity
C_f	Friction coefficient
g	Gravitational constant
n	Manning's n roughness coefficient
u and v	Horizontal velocity components
a_i	Area of the raster cell inside the node influence area
a_t	Total area of the raster cell
j	Number of cells inside a given node area of influence
SC	Surface canopy parameter
z_0	Land roughness surface parameter
$\mu_{residual}$	Mean surge residual
k	Number of recording locations
m	Number of storms
$\zeta_{k(dataset)}$	Surge level at a given location for a given land cover database
$\mu_{\zeta max}$	Mean maximum surge in m

p-value:	Probability value
μ_{mmsa}	Mean maximum surge anomaly
$\Delta\Phi_{SLR}$	SLR increment
$\Psi_{residual}$	Flooded area extent residual
Ψ_{flood}	Total flooded area in km^2
Ψ_{surge}	Flooded area extent caused by storm surge
Ψ_{SLR}	Flooded area extent caused by eustatic SLR
C_p	Hurricane central pressure
V_f	Hurricane forward speed
η	Mean Manning's n value (dimensionless)
Υ	Model uncertainties due to other factors (*e.g.,* hurricane land fall location)
e	Prediction model error
λ	Surge anomaly
ζ_{SLR}	Surge calculated under SLR
ζ_{MSL}	Surge calculated at MSL
$\vec{V_g}$	Geostrophic velocity vector at the low center
$\vec{V}$	Wind averaged horizontal velocity vector
ρ_{air}	Air density
C_p	Pressure representing the tropical cyclone

$\vec{V_c}$	Velocity vector of the moving reference system
C_D	Wind drag coefficient
H	Depth of the PBL layer
$\Omega_{building}$	Expected direct damage to building residual
$\Gamma_{\%}$	Estimated building damage increase in percentage due to land cover changes
$\Gamma_{\%}$	Estimated building damage increase in percentage due to land cover changes

TABLE OF CONTENTS

LIST OF FIGURES

LIST OF TABLES

CHAPTER I

INTRODUCTION

Hurricanes are the primary natural hazard threatening many coastal cities around the world. In the United States (US), coastal flooding caused by hurricanes is one of the most costly natural disasters (Lott and Ross 2006). For example, Hurricane Katrina was responsible for financial damages over a hundred billion dollars (USGS, 2005); other significant events were: Hurricane Andrew in 1992 ($40 billion), Hurricane Ike in 2008 ($27 billion), Hurricane Wilma in 2005 ($17 billion) and Hurricane Rita in 2005 ($17 billion) (Lott and Ross 2006). The state of Texas, in particular, has historically faced severe hurricanes, with Ike being the most recent major storm to hit the State.

Studies by Emanuel (2005) have shown an increasing destructiveness of tropical cyclones over the past 30 years. While hurricanes are a recurrent threat to coastal communities, climate research arguably indicates a potential increase in the mean sea-level (MSL) due to global warming (Church *et al.* 2008; Intergovernmental Panel on Climate Change 2007; Nichols and Cazenave 2010) and hurricane intensification over the next century (Knutson *et al.* 2010; Elsner *et al.* 2008). The combined effect of stronger storms with sea-level rise (SLR) is expected to increase hurricane storm surge risk in coastal areas (Lin *et al.* 2012). Predictions by Hallegatte (2012) indicate that,

_____

This dissertation follows the style of *Journal of Hydrologic Engineering*.

at a global level, economic losses due to tropical cyclones might increase from today's average of $26 billion per year to $100 billion per year by 2100. Thus, correctly understanding the potential impact of climate change and SLR on hurricane storm surge damage is crucial to protect society against major economic, social and infrastructure losses.

This dissertation investigates the influence of coastal wetlands under climate change on hurricane surge and damage with application to planning. The objectives of this research are:

1) To develop a framework that integrates Geographical Information Systems (GIS) and hurricane storm surge numerical models;

2) To quantify the uncertainty derived from coastal land cover spatial data on hurricane storm surge;

3) To investigate the potential impacts of SLR changes on land cover to hurricane storm surge and coastal damages.

To manage a potentially increasing coastal flooding hazard, the U.S. invests a considerable amount of resources in mapping floodplains and risk areas. Improvements in the understanding of the physics of storm surge processes have led to the development of hydrodynamic models capable of accurately estimating hurricane flood elevations and floodplains (Resio and Westerink, 2008). However, increasingly higher resolution and complex numerical methods require the use of High Performance Computing (HPC), or

supercomputing, for numerical simulation of hurricane storm surge (e.g., Westerink *et al* [2008], Tanaka *et al.* [2011]), which makes running these models not user-friendly.

To facilitate the assimilation of geospatial information in hurricane storm surge simulation, we propose a novel framework to integrate GIS and hurricane models. In Chapter 2, ***Arc StormSurge: Integrating Hurricane Storm Surge Modeling and GIS,*** we describe a geodatabase schema specifically designed to support hurricane storm surge modeling and coastal flood mapping. As part of this framework, a set of ArcGIS tools were developed to pre- and post-process model input/output by connecting the GIS interface with the supercomputing environment and streamlining the coastal floodplain mapping process. A case study simulation of Hurricane Bret is presented to demonstrate the tool's functionality. This framework is also used throughout this dissertation.

Through the integration of GIS with the hurricane computational models, it is possible to take full advantage of geospatial information to better represent the physical process involved in calculating storm surge and delineating flooded areas. For example, it is expected that land cover impacts the forcing and dissipation mechanisms of hurricane storm surge, first by interference in the transfer of momentum from the wind to the water column, and second by the dissipation due to frictional drag at the sea bottom.

To correctly evaluate the effects of land cover, namely wetlands and other coastal vegetation, on hurricane surge and damage, it is crucial to recognize its spatial location

and composition. For the State of Texas, three types of datasets from different agencies are available for selected time periods:

    1) The National Land Cover Dataset (NLCD) of 1992, 2001 and 2006;

    2) The Coastal Change Analyses Program (C-CAP) of 1996, 2001 and 2006;

    3) The National Wetlands Inventory (NWI) from 2011.

In Chapter 3, ***quantification of uncertainty in hurricane storm surge response due to land cover specification,*** we investigate the effects of these different datasets, as well as the time periods represented, on the surge response for coastal bays in mid Texas coast. We also present a case study for Hurricane Bret, comparing the simulated surge response to measured data.

SLR is expected to impact hurricane storm surge in coastal bays by the changes in the bays' geometry (i.e., deeper water depth and larger water surface area) and also by changes to the land cover (i.e., wetlands loses due to permanent inundation) with potential impacts to surge heights and inundation, and most importantly, to damages in coastal communities. The potential of wetlands to reduce storm surge in Louisiana was investigated by Wamsley *et al.* (2010), and the studies carried out by Loder *et al.* (2009), demonstrated the importance of correctly representing wetlands when making storm surge simulations. In Chapter 4, ***Effects of sea-level rise on hurricane storm surge and coastal damage in coastal bays,*** we quantify the impacts of wetlands degradation by SLR on hurricane storm surge and damage in coastal bays. These impacts are quantified

by residuals in the mean maximum surge, the inundated area, by the potential damage to buildings, population and businesses affected.

This dissertation is organized into one introductory chapter (this chapter), followed by three subsequent chapters as described above. The final chapter brings a summary and the overall conclusions of this research.

CHAPTER II

ARC STORMSURGE: INTEGRATING HURRICANE STORM SURGE MODELING AND GIS

INTRODUCTION

Hurricanes are a major cause of loss of human life and property in many coastal cities around the world. In the United States, in particular, coastal flooding caused by hurricanes has been one of the most costly natural disasters totaling approximately $370 billion dollars in the last 20 years (Lott and Ross 2006). It is, therefore, indispensable to accurately predict storm surge in an efficient working framework in order to assess an area's flood risk and to facilitate planning and design to minimize its impact.

The historical record of storms is too short and too sparse to support reliable statistical predictions of hurricane surge levels; therefore, numerical analysis is used for simulating and predicting flooding in coastal areas. In recent years, improvements in the understanding of the physics of storm surge processes have led to the development of computationally intensive hydrodynamic models capable of estimating hurricane flood elevations (Resio and Westerink 2008). However, entering the input to and interpreting the output from these models can be difficult and tedious, and, usually, the model output is not in a ready format for conveying findings to the public and decision-makers. In this context, Geographical Information Systems (GIS) can play an important role in pre- and post-processing spatial information and supporting input/output visualization.

This chapter discusses the development of a data model and set of tools to ease the preparation of the input files of the coupled *AD*vanced **CIRC**ulation and unstructured-grid version of *S*imulating *WA*ves *N*earshore (SWAN+ADCIRC) hydrodynamic and wave models through an automated file conversion between the GIS and model formats and the visualization of the results through maps. As part of this working framework, we propose the use of a geodatabase specifically designed to store the spatial information needed for modeling storm surges. Examples of the application of our framework to storm surge simulations for Hurricane Bret in Corpus Christi, Texas, are also included.

BACKGROUND

A review of integration of Computational Fluid Dynamics (CFD) and GIS is presented by Wong *et al.* (2007). Specifically, regarding coastal hydrodynamics, a storm surge numerical forecast model was developed by Yu *et al.* (2001) and integrated with GIS for querying and visualizing spatial information. In their work, they used two sub-systems: a numerical scheme to calculate the surge and GIS to visualize the results. Another example of CFD and GIS integration is presented by Ng *et al.* (2009) in which a GIS interface is used to pre- and post-process spatial information for and from a complex coastal three-dimensional hydrodynamic sediment and heavy metal transport numerical model. They developed a user-friendly interface to generate input files for the numerical model, and they incorporated functionality to process 3D results and convert point time series into raster time series. Zerger and Wealands (2004) presented an integration of GIS and numerical model results to support stakeholders' decision-making based on

static coastal flood risk maps. They used digital look-up maps, which were the result of pre-processing a set of storms, and stored the resulting surges in a raster database. They also reported the difficulty of managing the large amounts of information involved. Irby *et al.* (2009) used hurricane computational model results and GoogleEarth to develop visualization techniques to help raise public awareness of hurricane storm surge risk. Commercial software packages are also available to pre- and post-process hurricane computational models files and help visualize the model results (e.g., SMS [Aquaveo 2012]).

There are many numerical models that simulate hurricane storm surges. The ADCIRC model (Luettich and Westerink 2004), the Sea, Lake, and Overland Surge from Hurricane model (SLOSH) (Jelesnianski *et al.* 1992), the fully non-linear Finite Volume Coastal Ocean Model (FVCOM) (Chen *et al.* 2003), the Eulerian-Lagrangian CIRCulation (ELCIRC) model (Zhang *et al.* 2004) and the SWAN+ADCIRC coupled surge and wave model (Dietrich *et al.* 2011) are examples of such models. The framework presented here has been developed to work specifically with the SWAN+ADCIRC model; however, this framework may be readily modified to work with other computational models. The selection of the SWAN+ADCIRC model responds to the recommendation of the National Research Council's Committee on the Federal Emergency Management Agency (FEMA) Flood Maps for using coupled 2-D surge and wave models to calculate base flood elevations (BFEs) to decrease the uncertainty in determining water levels for coastal flooded areas (National Research Council 2009).

The SWAN+ADCIRC modeling framework has been successfully applied nationwide for storm surge studies in a number of locations (e.g., Ratcliff and Smith 2011; and Dietrich *et al.* 2011).

The ADCIRC model (Luettich and Westerink 2004) is a physically based, finite-element, shallow-water model that solves for water levels and currents at a range of scales. The SWAN model is a third-generation spectral wave model that computes random, short crested wind-generated waves, and wave transformation in nearshore and inland waters (Booij *et al.* 1999). For storm surge modeling, the 2-Dimensional Depth Integrated version of ADCIRC is typically used; this version solves the vertically integrated mass (Eq. 2.1) and the momentum (Eq. 2.2) equations, which are

$$\frac{\partial h}{\partial t} + \nabla_h\left(\vec{U}h\right) = 0 \tag{2.1}$$

$$\frac{\partial \vec{U}}{\partial t} + \left(U \bullet \nabla_h\right)\vec{U} = -g\nabla_h\left(\zeta + \frac{p(x,y)}{g\rho}\right) + f\,\hat{k}\times\vec{U} + \frac{\vec{\tau_s}}{h\rho} - \frac{\vec{\tau_b}}{h\rho} + \frac{\vec{\tau_w}}{h\rho} \tag{2.2}$$

where h is the water depth, t is the time, ζ is the surge elevation above mean sea-level, $\vec{U}$ is the depth-averaged horizontal velocity vector, p is the barometric pressure, f is the Coriolis force, $\hat{k}$ is a vertical unit vector, τ_s is the free-surface shear stress, τ_b is the

bottom shear stress, τ_w is the wave radiation stress, and ρ is the water density. For wave

modeling, the spectral wave model SWAN uses the following equation (Eq. 2.3)

$$\frac{\partial N}{\partial t}+\nabla_{\vec{x}}\left[\left(\vec{c_g}+\vec{C}\right)N\right]+\frac{\partial c_\theta N}{\partial \theta}+\frac{\partial c_\sigma N}{\partial \sigma}=\frac{S_{tot}}{\sigma} \tag{2.3}$$

where N is the wave action density spectrum , C_g is the wave group velocity, C_σ is the

propagation velocity, σ is the relative frequency, θ is the wave direction, C_θ is the

wave propagation velocity, S_{tot} is the wave growth caused by the wind, and C is the

current velocity. A more detailed discussion of the governing equations used in

ADCIRC and SWAN can be found in Luettich and Westerink (2004) and Booij *et al.*

(1999), respectively. For storm surge simulation, ADCIRC is forced by the wind and

pressure fields and the wave radiation stress resulting from the wave model. Tides and

river inflow can also be added as boundary conditions. SWAN, in turn, is forced by the

wind field and uses the water elevations from the surge model as input to define wave

characteristics. The coupled SWAN+ADCIRC model (Dietrich *et al.* 2011) uses the

same unstructured mesh of finite elements for both the wave and hydrodynamic models.

In this study we will consider the SWAN+ADCIRC input and output files presented in

Table 2.1.

Table 2.1: SWAN+ADCIRC files names and description.

name	model	description
fort.15	input	ADCIRC model control file and periodic boundary conditions
fort.14	input	mesh and boundary information
fort.13	input	nodal attributes (e.g., Manning's *n*)
fort.22	input	single meteorological forcing
fort.221	input	meteorological forcing wind fields
fort.222	input	meteorological forcing pressure fields
fort.61	output	water elevation time series at recording points
fort.62	output	depth average velocity time series at recording points
fort.63	output	water elevation time series in all nodes
fort.64	output	depth average velocity time series at all nodes
fort.71	output	atmospheric pressure time series at recording points
fort.72	output	wind time series at recording points
fort.73	output	atmospheric pressure time series at all nodes
fort.74	output	wind time series at all nodes
swan_DIR.63	output	wave direction at all nodes
swan_HS.63	output	wave height at all nodes
swan_TM01.63	output	wave period at all nodes
fort.26	input	SWAN model control file

Data models are database schemas used to store information on real-world systems in an organized framework. A geographic data model, or *geodatamodel*, specifically, can store geographic information and relate geographic features to GIS cartographic features (Maidment 2002). In a geodatamodel, the modeler can additionally embed meaning to GIS features, incorporating systems states, properties and behaviors for a specific application (Glennon 2010). Examples of geodatamodels for water resources and marine sciences are Arc Hydro (Maidment 2002) and Arc Marine (Wright *et al.* 2007), respectively. The Environmental Systems Research Institute (ESRI) has also developed thematic geodatamodels for different types of applications (ESRI 2012a).

According to Goodchild (2005), the coupling of numerical models with GIS can be done in three ways: (1) *embedded*, in which the model is entirely within the GIS system; (2) *closely coupled*, in which both the GIS and the model read from and write to the same files; and (3) *loosely integrated*, in which the model runs separately from the GIS and the communication is done via input and output files. In the first two cases, numerical models specifically developed to work with GIS are needed; in the third case, GIS is used to pre- and post-process information but requires the development of specific code to ensure an efficient communication channel.

To the best of our knowledge, there is no application that integrates the SWAN+ADCIRC with GIS for hurricane storm surge modeling. Arc StormSurge is a loosely integrated approach that allows the use of the already established storm surge model SWAN+ADCIRC and GIS to pre- and post-process the spatial information.

ARC STORMSURGE DATA MODEL

Arc StormSurge includes a data model, in geodatabase format, specifically designed to store the spatial information needed for ADCIRC and SWAN. Figure 2.1 shows the Arc StormSurge framework. The Arc StormSurge geodatabase schema was designed with the Unified Modeling Language (UML). In the geodatabase, the feature dataset, feature class, attribute, and relationship class names are predefined to ensure its functionality.
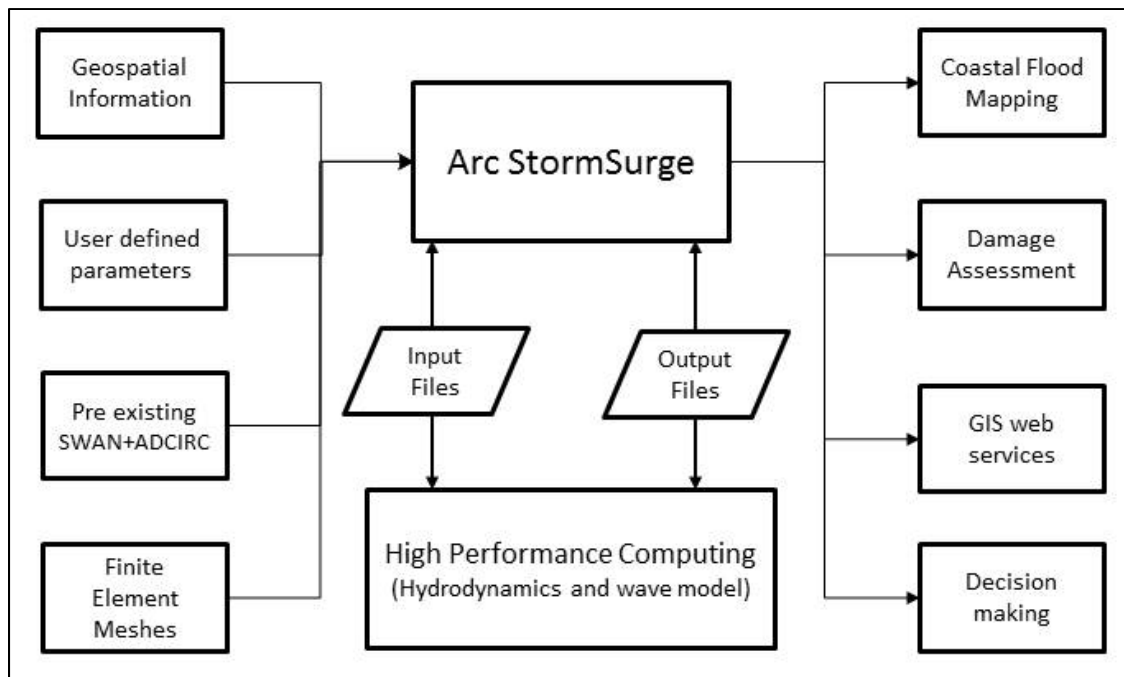
Figure 2.1: Arc StormSurge framework.

The geodatamodel includes feature datasets, tables (which were grouped in table sets), grids, raster catalogs and relationship classes (Figure 2.2). Even though *table set* is not a standard ArcGIS concept, it has been used here for clarity purposes. The geodatamodel is described below using the following nomenclature: {*feature dataset, table set or raster catalog*}, [*feature class, table or raster*], <*attribute*> and |*relationship class*|. Some attribute names are self-explanatory and their definitions will be omitted for the sake of space, so they are not included here. A detailed description of the geodatamodel is provided on Appendix A.
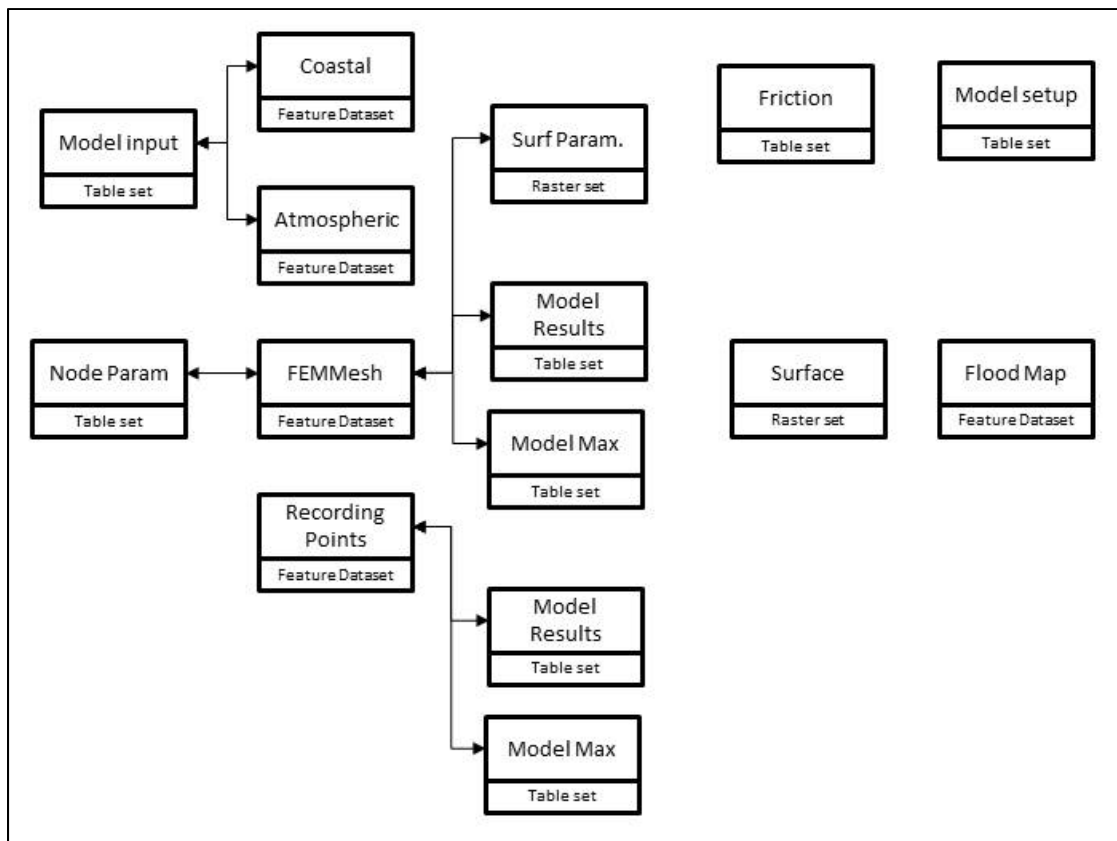
Figure 2.2: Arc StormSurge geodatabase schema.

The geodatamodel includes five feature datasets. The **{Atmospheric}** feature dataset stores storm and weather station information. This information includes the storm track, size, forward speed and central pressure over time. **{Atmospheric}** also includes the location of weather stations in the study area. The **{Coastal}** feature dataset stores data related to the coastal environment. This information includes the shoreline, bathymetry, and locations of tide and current monitoring stations. The **{FEMMesh}** feature dataset stores information about the SWAN+ADCIRC mesh (which, in the following will be called "mesh"). This information includes data about the mesh nodes, edges and

elements, as well as the type and location of model boundaries. The boundary types can be external (i.e., with no normal flow, with specified normal flow, or external barrier) or internal (i.e., island with no normal flow or barriers). The **{RecordingPoints}** feature dataset stores the location of the points for which model results, such as water levels, current velocities, wave characteristics, wind velocities, and barometric pressures, are recorded (which, in the following will be called recording points). The **{FloodMap}** feature dataset stores the extent of flooded areas, as well as the delineation of areas based on any user defined parameter and threshold (e.g., areas defined by waves higher and lower than 1 m, respectively [National Research Council 2009]). **{FloodMap}** also includes cross sections for which flood levels and wave heights can be visualized.

The geodatamodel also includes six table sets. The **{ModelInput}** table set stores observed time series of wind velocity and hurricane barometric pressure at the weather stations and current velocity and tides at the coastal stations. The **{NodeParam}** table set stores mesh-node parameters, including *initial submergence status* (i.e., dry or wet), *directional effective roughness length*, *wind shielding* (by canopy) status, *Manning's n*, *initial sea surface elevation*, *average horizontal eddy viscosity*, and whether or not *wave refraction* is included in the analysis. The **{Friction}** table set stores lookup tables that relate the terrain land cover at the mesh nodes to friction parameter values such as *Manning's n*, *surface canopy* factor and *surface roughness length* factor. Terrain land cover categories from the National Land Cover Dataset (NLCD) for years 1992 (Vogelmann *et al.* 2001), 2001 (Homer *et al.* 2004), and 2006 (Fry *et al.* 2009), the

National Wetlands Inventory (NWI) for year 1993 (U.S. Fish and Wildlife Service 2012) and the Coastal Change Analysis Program (C-CAP) for years 1996, 2001 and 2006 (NOAA 2012a) were included. Each land cover dataset parameters were obtained from Leuttich and Westerink (2004), Tsihrintz and Madiedo (2000), Bunya *et al.* (2010), Wamsley *et al.* (2009), Atkinson *et al.* (2011) and Arcement and Scneider (1989). The tables, though, can be edited if site-specific data are available. The **{ModelControl}** table set stores information related to the computational simulations including the number of days of the simulation, the time step and the map coordinate system. The **{ModelResults}** table set stores time series generated by the computational model including depth-averaged current velocities, water levels and depths, wind and pressure, and wave characteristics (i.e., direction, height and period) at the mesh nodes and recording points. The **{ModelMax}** table set is similar to the previous table set, but it stores maximum values, rather than complete time series, at both mesh nodes and the recording points.

The geodatamodel includes four raster catalogs (i.e., grids of time series) and twelve grids. The four raster catalogs store interpolated values of the water elevation, water depth, wave height and wave period over time. Four of the grids store maximum water elevation, maximum water depth, maximum wave height and period from the corresponding catalogs. Other grids store the mesh resolution and friction parameters (i.e., Manning's *n*, surface canopy factor and wind direction reduction factor). Additionally, ground elevation and land cover grids are stored in the geodatamodel.

The geodatamodel also includes seven relationship classes that relate tables to feature classes in feature datasets. These relationship classes relate wind and pressure data in **{ModelInput}** to the weather stations in **{Atmospheric}**, and water elevation, current velocity, wave characteristics (i.e., height, direction and period) and tide data in **{ModelInput}** to the gauge stations in **{Coastal}**. They also relate the node parameters in **{NodeParam}** to the nodes in **{FEMMesh}**; the model output in **{ModelResults}** and **{ModelMax}** to the nodes in **{FEMMesh}** and points in **{RecordingPoints}**; and the boundary type in **{FEMMesh}** to the model settings in **{ModelSetup}**.

ARC STORMSURGE TOOLS

The Arc Storm Surge tools facilitate the exchange of information between the hydrodynamic models and the geodatabase. The tools were developed using the PYTHON programming language with the NumPY and SciPY libraries, and Arc Objects with the Arc PY library for ArcGIS 10. They are available in three formats: as PYTHON scripts, as ArcGIS 10 tool boxes that can be used with Model Builder, and as an ArcGIS 10 toolbar. The tools can be classified into pre-processing and post-processing tools, plus one tool that creates on-the-fly an empty Arc StormSurge geodatabase in a user-defined folder. We describe the tool names with the following notation '*Toolname*' and the SWAN+ADCIRC files with */filename/*.

Pre-processing Tools

The pre-processing tools are organized in five groups: (1) mesh tools; (2) spatial parameter tools; (3) monitoring station and recording point tools; 4) computational model setting tools; and 5) atmospheric forcing tools. A summary of the tools is presented in Appendix B.

The mesh tools populate **{FEMMesh}** based on a \fort.14\ file, or create a new \fort.14\ file based on a **{FEMMesh}** or **{Coastal}**. Some of the tools also allow editing of **{FEMMesh}**, which automatically updates the corresponding \fort.14\ file (Table 2.1).

The spatial parameter tools create friction parameter grids (i.e., Manning's *n*, surface canopy factor and surface roughness length) based on a land cover grid and the lookup tables in **{Friction}**, and populate the mesh node friction parameters in **{NodeParam}** based on a weighted average of the parameter grid values in their area of influence (i.e., the geometric locus of the points that are closer to a node than to any other node). These tools also populate **{NodeParam}** based on a \fort.13\ file, and create/update a \fort.13\ file based on user modification to **{NodeParam}**.

The recording point tools populate **{RecordingPoints}** based on a \fort.15\ file, and update a \fort.15\ file based on **{RecordingPoints}**. The model setting tools populate **{ModelControl}** based on the /fort.15/ and /fort.26/ files. This information can later be used to create metadata for the post-processed files.

The atmospheric forcing tools populate **{Atmospheric}** based on the Atlantic Best Track data files (HURDAT) (NOAA 2012b) or the Oceanweather Inc. /trop.file/, as well as from already existent wind/pressure fields files /fort.221/ and /fort.222/.

Post-processing Tools

The post-processing tools are organized in three groups: 1) tools that import computational model results; 2) tools that process computational model results; and 3) tools that map inundated areas from model results. A summary of the tools is presented in Appendix B.

The tools that import computational model results populate **{ModelResults}** based on files /fort.63/, /fort.64/, /swan_DIR.63/, /swan_HS.63/ and /swan_TM01.63/, /fort.73/ and /fort.74/ for the mesh nodes, and /fort.61/, /fort.62/, /fort.71/ and /fort.72/ for the recording points. They also populate **{ModelMax}** based on the maximum values of the **{ModelResults}** time series for both mesh nodes and recording points.

The tools that process model results create raster catalogs based on **{ModelResults}** and grids based on **{ModelMax}**. To ease the analysis, all raster catalogs and grids have the same cell size and are snapped to the ground elevation grid. These tools also query **{ModelResults}** and **{ModelMax}** and can identify, for example, areas that will be flooded with a water depth greater than a given value for a period longer than a given value. Finally, time series plots can be generated based on **{ModelResults}**.

The tools that map floodplains populate **{FloodMap}** based on the difference between the water levels in **{ModelMax}** and ground elevation raster surface, which should be stored in the geodatabase. The tools may also be used to classify the simulated flooded areas into V- and A-zones (e.g., areas defined by waves higher and lower than 1 m, respectively [National Research Council 2009]) depending on the simulated wave heights in **{ModelMax}**, and to view model results using cross-sectional cuts.

APPLICATION

The Arc StormSurge data model and tools were used in the simulation of Hurricane Bret, which made landfall in 1999 close to the city of Corpus Christi on the Texas Gulf Coast. Corpus Christi is located on the margins of Corpus Christi Bay and Nueces Bay, which are connected to the open sea through Aransas Pass and protected by a barrier island. Hurricane Bret was a Category 3, according to the National Hurricane Center, with winds around of 185.2 km/h at landfall and minimum pressure of 944 mb (NOAA 2001). This storm caused damages to southern Texas and northern Mexico. We used this simulation to delineate the inundated areas in the city of Corpus Christi, which was impacted by Hurricane Bret. The city of Corpus Christi has faced a number of hurricane-related damage episodes in recent decades (e.g., Hurricane Beulah in 1967, Hurricane Bret in 1999 and, most recently, Hurricane Alex in 2010).

The purpose of this case study is to illustrate the application of Arc StormSurge to a real-world case. Because of the number of different tools included in Arc StormSurge, only a

few of them are presented here, namely, the ones that best illustrate the SWAN+ADCIRC and GIS integration.

In this study, the TC96 model (Thompson and Cardone, 1996) was used to estimate wind and pressure fields of Hurricane Bret from a historical best track data file developed by Oceanweather, Inc. The 'ReadHURDAT' tool was used to read the best track data file, extract the hurricane meteorological information (i.e., forward speed, central pressure, size and location) and create a number of points that represent the position of the hurricane at different times, which were stored in the [HurricaneEyePath] feature class. The 'CreateTrack' tool was used to create a line that represents the hurricane track, which was stored in the [hurricaneTrack] feature class of {Atmospheric}. The 'ImportWindPressure' tool was used to read the TC96 model result files /fort.221/ and /fort.222/ (Table 2.1), which store wind and pressure field information, and populate the [windTB] and [pressureTB] feature classes of {modelInput}. This wind and pressure field information was used to force the SWAN+ADCIRC simulations. Figure 2.3 presents a graphical representation of Hurricane Bret as it progresses towards landfall, and meteorological parameters.
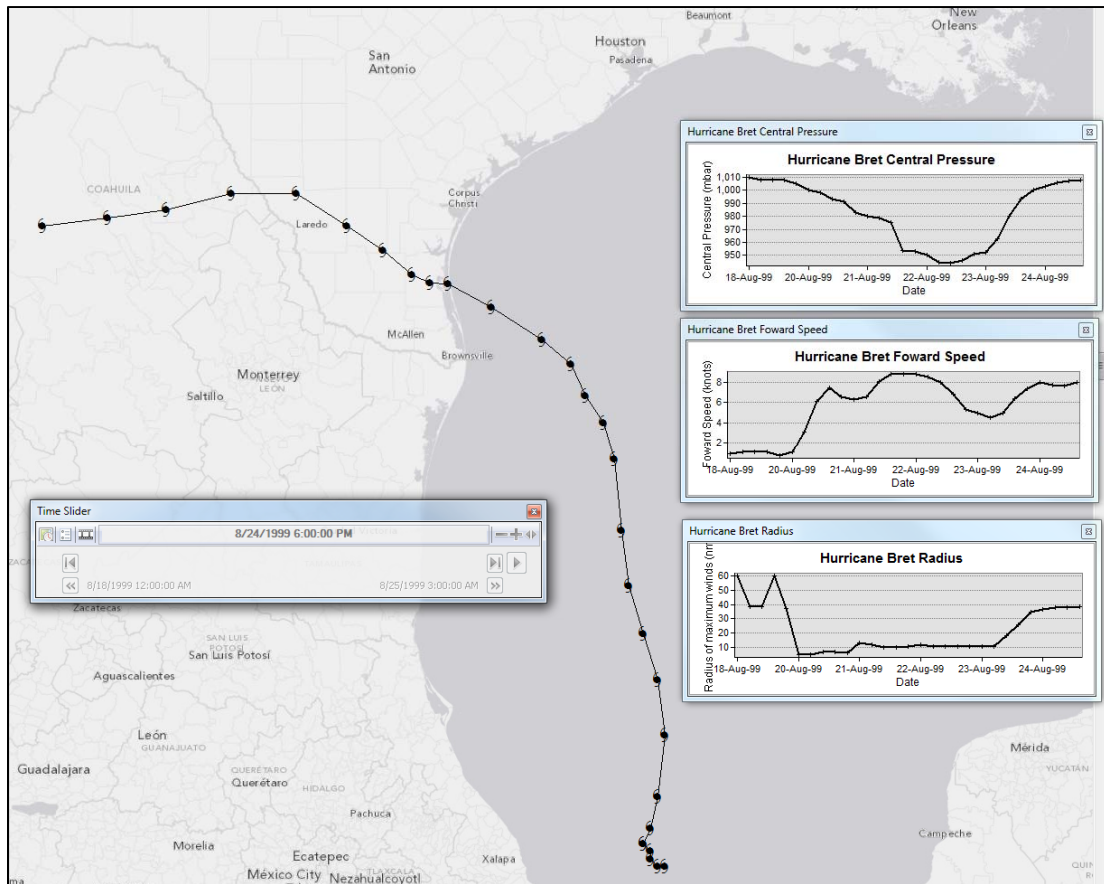
Figure 2.3: Hurricane Bret track created from the HURDAT (NOAA) best track information database using the 'ReadHURDAT' and 'Create Track' tools and stored at [hurricane EyePath] and [hurricaneTrack] feature datasets. Plotted using the time aware feature and graphics representing it central pressure, forward spend and radius to maximum wind speeds.

To improve the performance of SWAN+ADCIRC without sacrificing accuracy, one might need to combine existing computational meshes so that the appropriately refined resolution is used in the areas of interest, while computational efficiency is retained by using lower resolution elsewhere. In this application, a mesh that combines two pre-existing and validated computational meshes was developed. One of these two meshes is the Texas Mesh (Dietrich *et al.*, 2011), which is an unstructured grid with 3.3 million

nodes and 6.6 million elements covering the Gulf of Mexico and part of the Atlantic Ocean. It has a high resolution along the Texas coast and inland areas (up to 50 m); however, because of its high resolution, SWAN+ADCIRC simulations can consume up to 2,500 computational hours per day of storm duration. The other mesh is the East Coast Mesh (2001), which has 250,000 nodes and 500,000 elements covering the Gulf of Mexico and the East Coast of the US, without inland areas. This mesh allows numerical simulations in approximately 150 computational hours per storm day simulated.

Arc StormSurge is used to import both meshes to respective feature classes in {FEMMesh}. In this process, all boundary conditions were recognized and the 'createMesh' tool created /fort.14/ files similar to the original meshes for testing purposes. Once the two meshes were imported into the geodatabase, standard GIS functions were used to edit the nodes, removing or adding nodes to the mesh, increasing resolution in the areas of interest and decreasing resolution elsewhere. The areas around Baffin, Corpus Christi, Nueces, San Antonio and Matagorda Bays were represented using high resolution information, while, lower resolution was used in other coastal areas and offshore (Figure 2.4). Mesh triangulation was performed using the constrained Delaunay method (ESRI, 2012b), and subsequent manual TIN editing was necessary to ensure numerical stability. Standard GIS functions were used to modify the mesh elements editing the TIN itself, adjusting the elements sizes, swapping nodes/edges, changing nodes locations and adding/deleting elements.
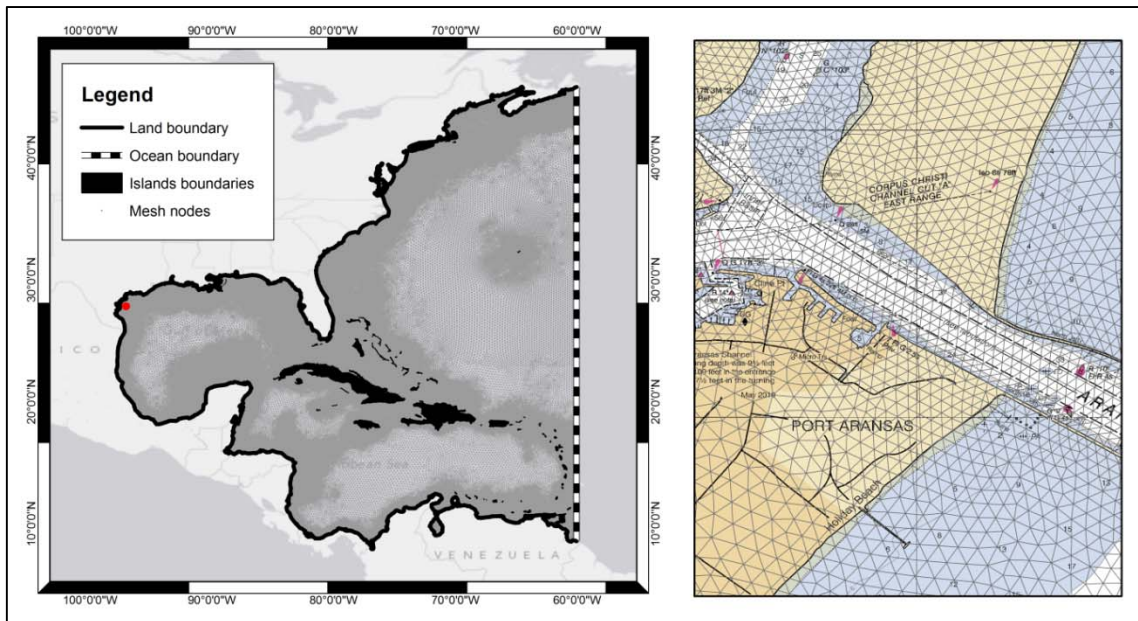
Figure 2.4: a) The finite element mesh created with Arc StormSurge stored in {FEMMesh} feature dataset, including the [meshnodes], [boundaryLine], [island] and [meshEdge] feature datasets. **b)** Detail of the mesh resolution on Aransas Pass

The 'TINtoMesh' tool was used to convert the TIN feature class to the {numericalMesh} elements. The mesh [domain] feature class is extracted from the TIN domain and is also used to create the [boundaryLine] and [boundaryNode]. The TIN nodes and elements are extracted to the [meshElement] and [meshNode] feature classes. The boundary conditions types were manually defined afterwards.

The new mesh with 1.3 million nodes and 2.5 million elements was converted to the SWAN+ADCIRC \fort.14\ file. For the new mesh (referred from here on as Arc StormSurge mesh), the computational run time is approximately 460 computational

hours per storm-day; this represents an 80% reduction with respect to the 2,500 hours required when using the Texas Mesh.

Here, we imported the geospatial parameters from the Texas Mesh and created a similar file matching Arc StormSurge mesh. The geospatial parameters (e.g., Manning's *n*) were extracted using the tools 'ImportGeospatialParameters', 'CreateFrictionalRaster', 'FrictionTonodes', and a new /fort.13/ file for SWAN+ADCIRC was created. The spatial representation of frictional drag at the sea bottom, represented by Manning's *n*, and wind blocking areas (*surface canopy* coefficient) are presented in Figure 2.5.

Figure 2.5: Geospatial representation of the frictional drag at the sea bottom by the Manning's *n* parameter (left) and the wind stress reduction trough the surface canopy coefficient (right).

To validate the Arc StormSurge mesh, we created 22 recording points with the 'Update Recording Points' tool (Figure 2.6). We simulated Hurricane Bret using the same model set-up, running on the same platform (Texas A&M supercomputer *eos*) for each computational mesh.
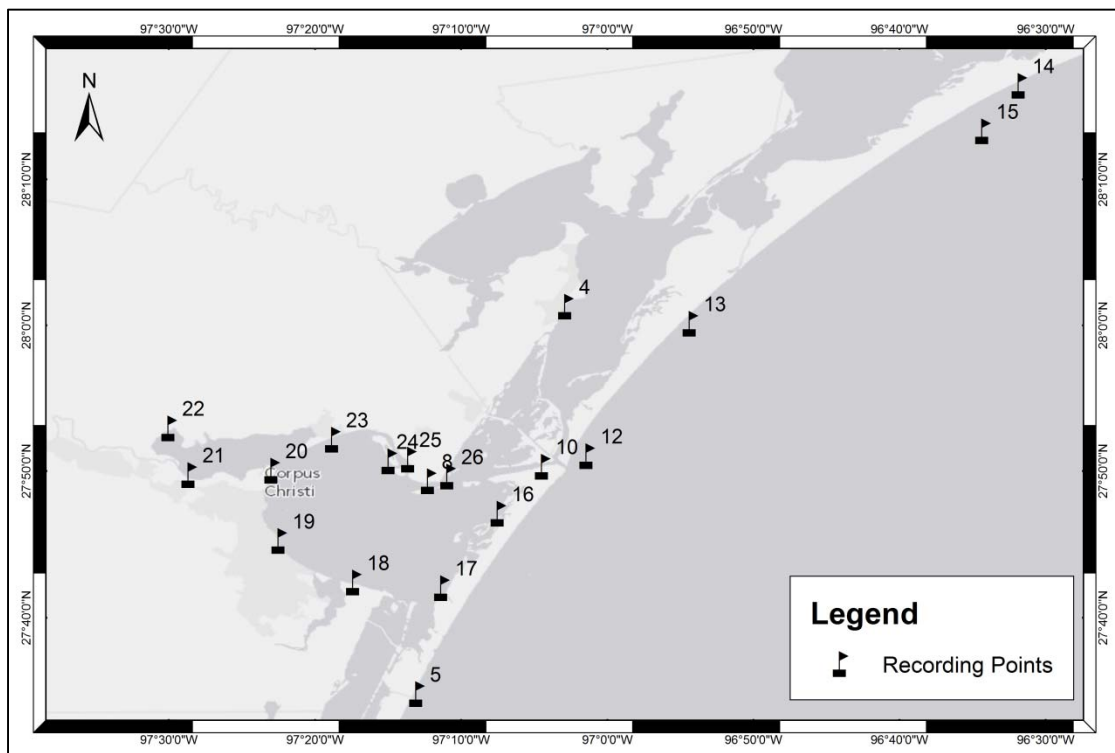
Figure 2.6: Recording points stored in the [stWaterLevel] feature dataset.

We extracted water levels time series for each recording point from both simulations. A sample of these time series is presented in Figure 2.7. Each plot represents the water level above MSL (surge) over the simulation time for one recording point. Within our

study area, the Arc StormSurge mesh presented a very good match with the validated

Texas mesh as can be verified in the Figure 2.7.
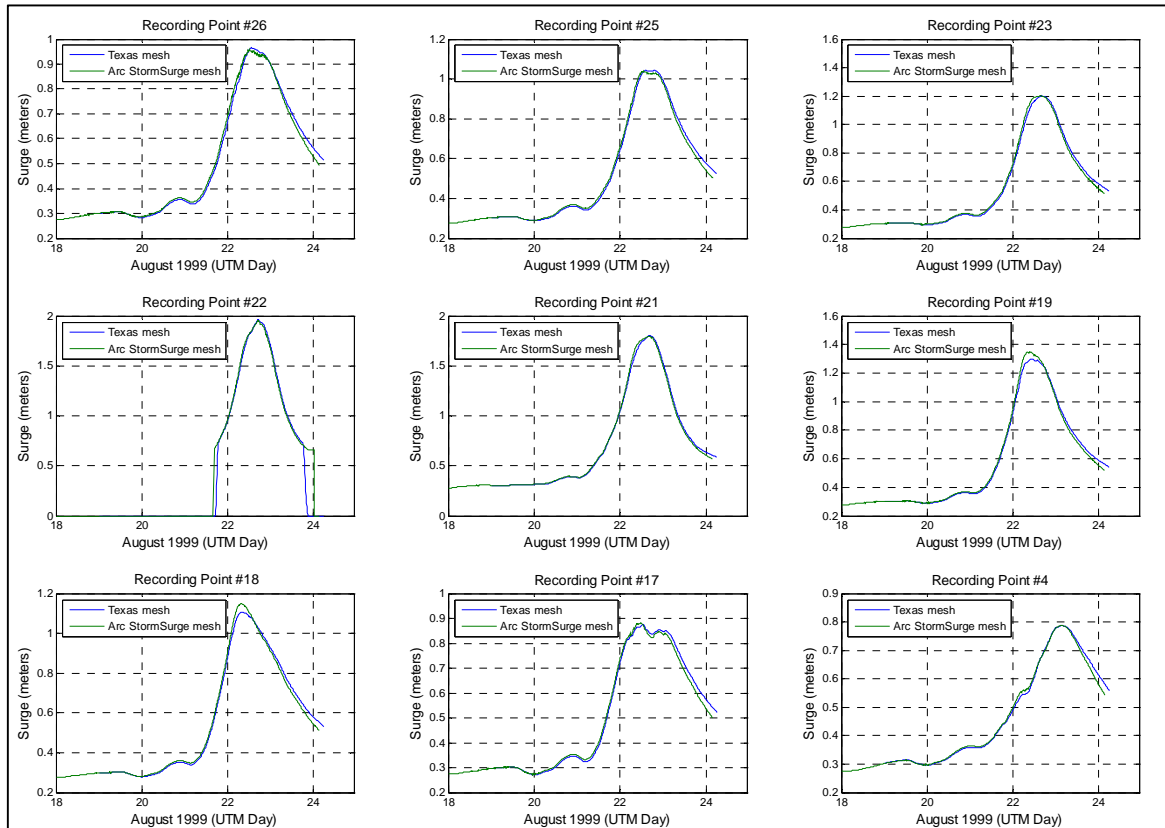
Figure 2.7: Validation of the Arc StormSurge mesh against the Texas mesh using Hurricane Bret. Water levels from the hurricane surge during the entire simulation. Blue line is the result from the Texas mesh and the green line the result from Arc StormSurge mesh.

When considering the peak surge at the 22 stations, the overall root mean square error

(RMSE) was 0.05 m, which given other model uncertainties, is insignificant. The overall

correlation coefficient R^2 was 0.96. A comparison of the maximum peak surges for each

recording point from the Arc StormSurge and the Texas mesh simulations is presented in

Figure 2.8.
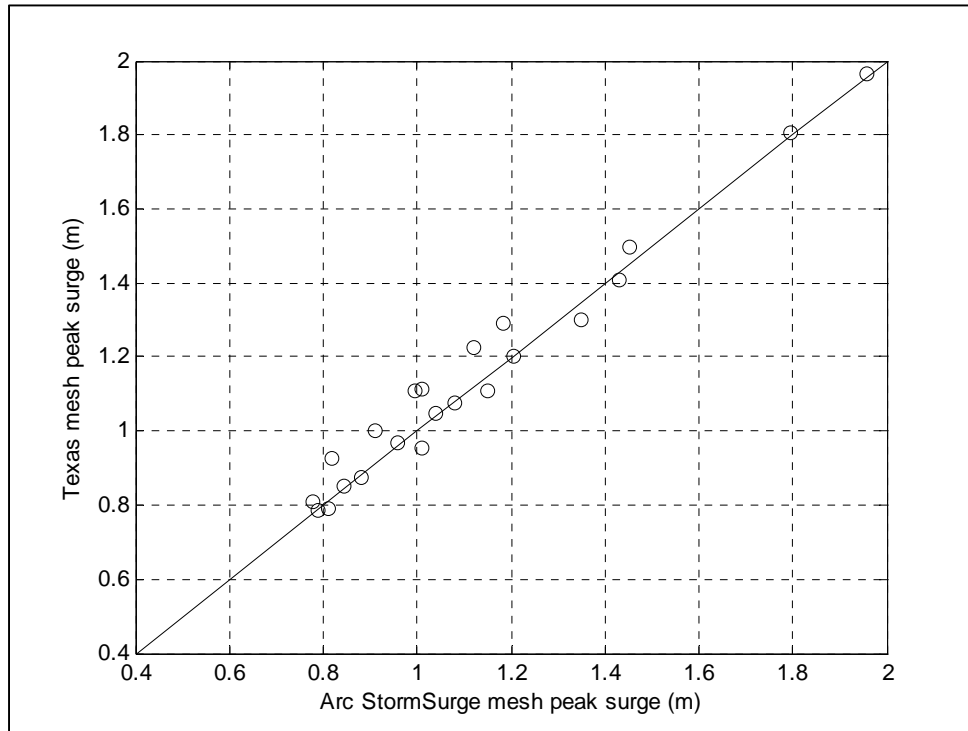
Figure 2.8: Maximum surge results from the Arc StormSurge mesh and the Texas mesh for 22 recording points.

The 'ImportMeshWaterLevel' tool was used to import the water levels calculated by

SWAN+ADCIRC at every mesh node to the [meshWater] table and the 'ImportWaveHs'

tool to import the wave heights stored at the [meshWaveHs] table. The

'ExtractMeshMAXws' and 'ExtractMeshMAXwhs' tools were applied to extract the

maximum water levels and wave heights for the entire simulation period and store them

in the [meshMAXWater] and [meshMAXWaveHs] tables. These tables are related to the mesh nodes [meshNode] feature class by the {resultsTomesh} relationship classes. The 'CreateSurface' tool was used to create grids. The conversion from point to raster was accomplished using one of the default ArcGIS 10 interpolation algorithms (i.e., natural neighbor), but other interpolation algorithms could also have been used. It is recommended to snap the created grids to the existing DEM ({coastal} [DEM]) to ease the ensuing analysis. Given the nature of the unstructured mesh (variable resolution), the {surface} raster resolution (cell size), a user-defined parameter, should be consistent with the model resolution in the area of interest. For this study we used topography data from the National Elevation Dataset (USGS 2012) with a resolution of 30 m.

The delineation of flood polygons is automated with an algorithm that combines the mapping of wet and dry areas (taking advantage of ADCIRC wetting and drying scheme [Blain *et al.* 2010]) and the flooding depths from the model results and the DEM topography. This algorithm excludes from the flood polygons: (1) areas that have a lower elevation than the water level, but are isolated from any water body; and (2) areas whose elevation is greater than the calculated flood level, as they could have been inaccurately included in the wetted area of influence of a node. The resulting flood polygons from the Hurricane Bret simulation are shown in Figure 2.9.
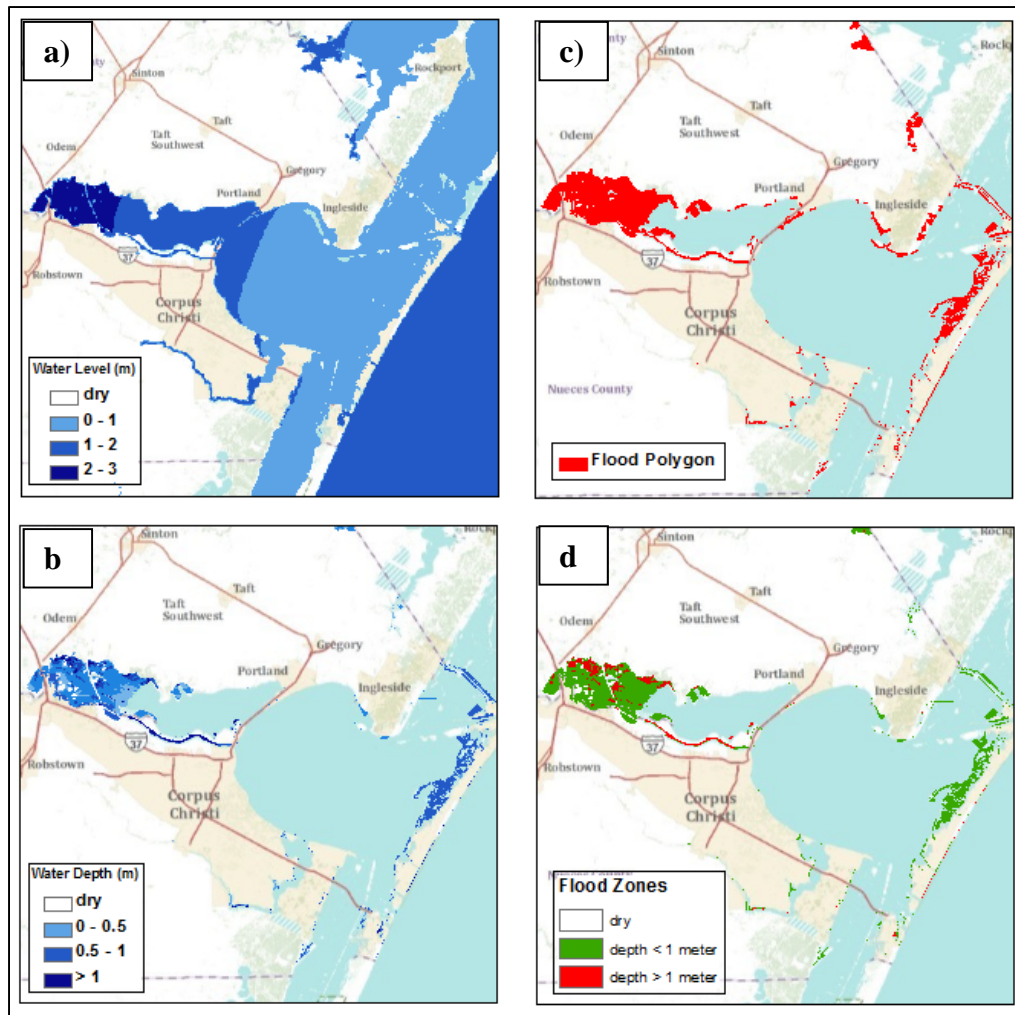
Figure 2.9: a) Maximum water levels extracted from the model results files using 'Extract mesh MAX ws' tool and interpolated by 'Create Surface' tool. **b)** Water depth over flooded areas created using the 'Calculate MAX water depth' and interpolated by 'Create Surface' tool. **c)** Flood polygons delineated by the 'Delineate Flood Polygons'. **d)** Flood zones classified by a water depth threshold of 1 m using the 'Classify flood zones' tool.

Here we demonstrate the classification of the flooded areas based on a given water depth. It consists of querying [surfMaxWaterLevel], identifying the areas that satisfy certain condition (i.e., greater or less than one m) and storing the resulting polygons in a

temporary polygon feature class [tempClassify]. The result of the intersection of [tempClassify] and [floodArea] is stored in the [floodClass] polygon feature class with the attribute <floodZone> representing the classified area. A similar procedure could be applied to define the FEMA V-zone (wave heights higher than 1 m) or A-zone (wave heights less than 1 m) areas from a given simulation.

SUMMARY AND CONCLUSIONS

Arc StormSurge is a tool to integrate GIS and high performance supercomputing modeling of hurricane storm surge. It can be used to accomplish model setup, or for post-processing simulation results, streamlining coastal flood map delineation and sharing. Arc StormSurge is a geodatamodel specifically designed to support hurricane storm surge applications and to connect a commonly used numerical model for hydrodynamics and storm surge calculation (ADCIRC) coupled with a wave model (SWAN) to GIS. A set of pre and post-processing GIS tools are developed to facilitate the integration of geospatial data to numerical modeling and to stream line the coastal flood delineation process.

Coastal surges are one of the most costly and dangerous aspects of hurricanes that strike the United States. Therefore the ability to geospatially understand flooding extents and magnitude is crucial to better protect coastal infrastructure and populations. The integration of state-of-the-art hurricane storm surge models with GIS is critical for

enhancing geospatial analyses of surge events, conveying information to government officials, stakeholders, and the general public.

The case study for Corpus Christi demonstrated that is possible to use Arc StormSurge to develop a mesh by combining two pre-existing and validated meshes, in order to reduce computational time by an order of magnitude, while maintaining high resolution and accuracy inside the study areas. The flood zones were delineated using the automated mapping capabilities of Arc StormSurge and displayed using ArcGIS Server and a FLEX API application to demonstrate the data sharing capabilities of the framework.

The outreach capacity of GIS with its web applications, GIS servers, GIS in the cloud and GIS web services is enormous. Considering that planning, prevention, management and mitigation of natural disasters such as hurricanes are highly dependent on geospatial information and especially the web, Arc StormSurge demonstrates the potential for easily conveying hurricane storm surge modeling information. Its applications can be used for real time alert systems, coastal community planning, to support FEMA maps modernization programs, ecosystems and natural resources analyses, and regional planning.

CHAPTER III

QUANTIFICATION OF UNCERTAINTY IN HURRICANE STORM

SURGE RESPONSE DUE TO LAND COVER SPECIFICATION

INTRODUCTION

Hurricane storm surge is one of the most costly natural disasters in the United States, as shown by (Lott and Ross 2006) from 1980 to 2006. According to Resio and Westerink (2008), an improved understanding of the physics of storm surge has led to the development of reliable physics-based numerical models for storm surge simulation. The use of numerical methods to model this phenomenon is of utmost importance for predicting and simulating storm surges, as historical data on surges is limited in both the number of storms and the number of locations to support reliable statistical predictions. Many studies investigated storm surges using this physically-based numerical models (Irish *et al.* 2005; Mattocks and Forbes 2008; Rego and Li 2010; Westerink *et al.* 2008; Ebersole *et al.* 2010; Xu *et al.* 2010; Chen *et al.* 2007; Huang *et al.* 2010; Dietrich *et al.* 2010; Bunya *et al.* 2010; Dietrich *et al.* 2011).

Among other variables, we expect that land cover plays an important role in the forcing and dissipation mechanisms of storm surge in coastal bays (Westerink *et al.* 2008). A methodology for extracting friction parameters from land cover datasets is presented by Atkinson *et al.* (2011). Recent studies discussed how land cover information can be incorporated in hurricane storm surge modeling and, more specifically, how land cover

type data can be mapped into georeferenced friction parameters (Westerink *et al.* 2008; Wamsley *et al.* 2009; Bunya *et al.* 2010; Dietrich *et al.* 2011). The impact of land cover changes (i.e., wetlands loss due to sea-level rise) on hurricane storm surge modeling has also been investigated (Wamsley *et al.* 2009; Smith *et al.* 2010; Loder *et al.* 2009; Wamsley *et al.* 2010).

A better understanding of uncertainty in estimating hurricane surge flooding from numerical analyses is crucial for determining more realistic confidence intervals on storm surges used for forecasting, planning and design efforts along the coast. (Resio *et al.,* in review, 2012) demonstrated the importance of quantifying uncertainty for design applications, showing that surge results could be underestimated by up to one m for the New Orleans area, considering annual exceedance probabilities in the 0.01 to 0.05 range. Cardone and Cox (2012) studied uncertainties in the surge response due to different wind field models. Among the many sources of uncertainty (e.g., uncertainty in terrain characteristics and bathymetry, meteorological conditions, and model errors), in this paper, we investigate the influence of land cover specification on hurricane storm surge response and quantify the uncertainty generated by different land cover datasets. The study area includes the coastal bays and estuaries in the Corpus Christi area. We also compared the simulated surge using different land cover datasets to measured data from Hurricane Bret.

MID TEXAS COAST BAYS

Texas has faced a number of hurricanes throughout its history, from the 1900 Galveston Hurricane, the deadliest hurricane in U.S. history, to more recent events such as Hurricane Ike in 2008 and Rita in 2005. Many of them have caused losses on the order of a billion dollars (Lott and Ross 2006). Texas also faces nearly yearly episodes of more moderate tropical storms and weak hurricanes, for example in the most recent years, Tropical Storm Don in 2011, Hurricane Alex and Tropical Storm Hermine in 2010, and Hurricane Ida in 2009.

We concentrate our study on the mid Texas coastal bays, namely Matagorda, Lavaca, San Antonio, Copano, Corpus Christy and Baffin Bays (Figure 3.1). The mid Texas coast has a complex system of bays and estuaries. The Colorado River is the main affluent to Matagorda Bay, which is separated from the Gulf of Mexico by a narrow barrier island and connected to Lavaca Bay forming an estuary with Chocolate Bay, Cox Bay and Keller Bay. Another major Texas river, the Guadalupe River, drains into the system at San Antonio Bay, also separated from the coast by the barrier island Matagorda Island. The barrier islands offer natural protection to the entire bay system, which is hydraulically connected behind the barrier island and through the Intercoastal Waterway. Tidal inlets offer water exchanges points with the Gulf of Mexico, with Aransas Pass being one of the most important exchange points.
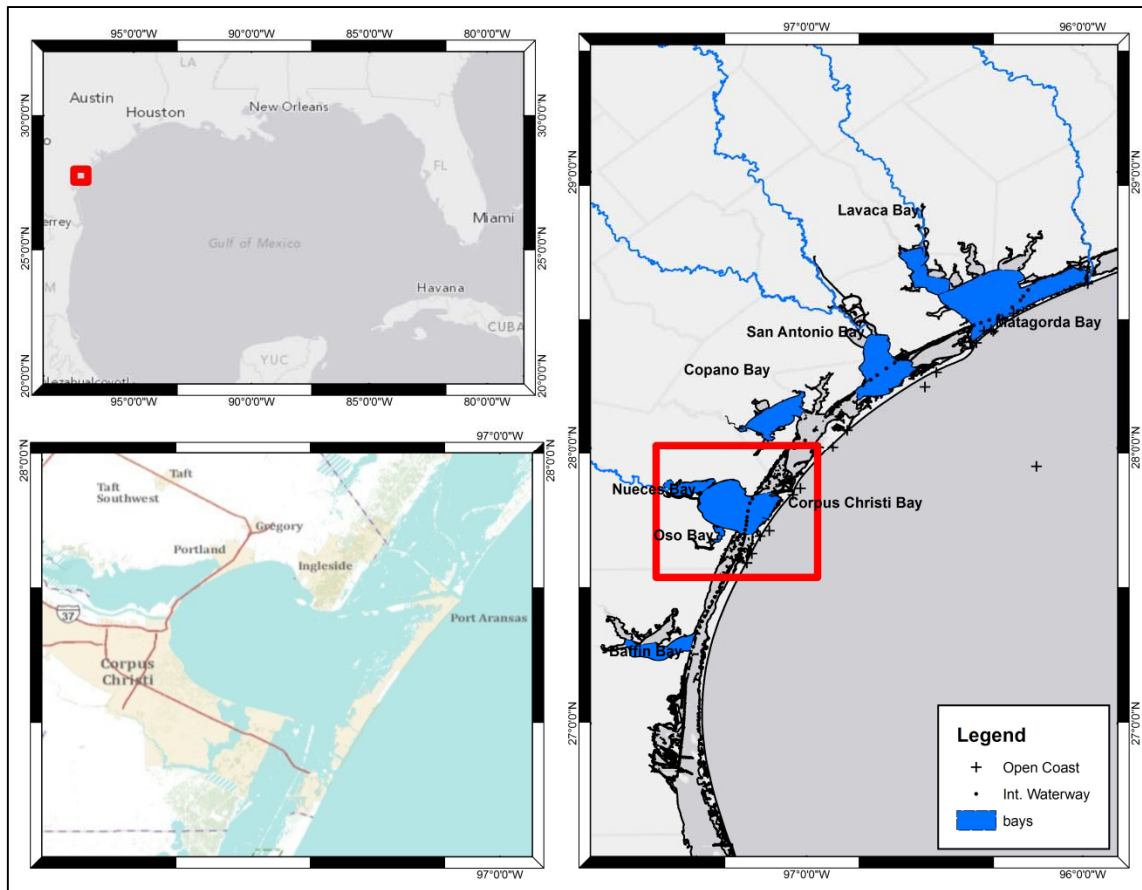
Figure 3.1: Study area location. The mid Texas coast location on the Gulf of Mexico. The coastal bays and major rivers. The location of the cities of Corpus Christi, Ingleside, and Port Aransas.

The main economical center of this region is the City of Corpus Christi with a population of approximately three hundred thousand people. Corpus Christi is home to the Naval Air Station Corpus Christi and the fifth largest port in the nation, the Port of Corpus Christi. Also in the region are the cities of Port Aransas, Rockport, Port Lavaca and Aransas Pass. This area has been impacted by a number of hurricanes (i.e., Hurricane Beulah in 1967, Hurricane Bret in 1999 and, most recently, Hurricane Alex in 2010).

LAND COVER DATASETS

We considered three land cover datasets: 1) the National Land Cover Dataset (NLCD) (USGS 2011b); 2) the Coastal Change Analyses Program (C-CAP) (National Oceanic and Atmosphere Administration, 2012a); and 3) the National Wetlands Inventory (NWI) (U.S. Fish and Wildlife Service 2012). Although the Gap Analyses Program (GAP) (USGS 2011a) would potentially offer a fourth dataset, our study region was not covered by any regional GAP project, and therefore we could not include this dataset in the analyses.

The National Land Cover Dataset (NLCD) is available at a spatial resolution of 30 m for the years of 1992, 2001 and 2006. The 1992 dataset, developed by the U.S. Geological Survey (USGS) EROS Data Center (EDC) in the late 2000s, uses the land use classification of the early 1990s Landsat Thematic Mapper and other sources of data (Vogelmann *et al.* 2001). This classification included 21 classes, which resulted from merging the Dobson *et al.* (1995) and the Anderson (1976) classification protocols. The 2001 dataset improves the 1992 dataset by using the classification of the 2001 Landsat Enhanced Thematic Mapper (ETM) satellite data. This product resulted in 16 classes (Holmer *et. al.* 2004). The 2006 dataset used the same 16 classes of the 2001 classification and was derived from the circa 2006 Landsat Enhanced Thematic Mapper+ (ETM+). The three datasets represent land cover changes over the period of 2001 to 2006 (Fry *et al.* 2009).

The C-CAP dataset was developed by the NOAA Coastal Services Center at a 30-m resolution for the entire U.S. and is available for years 1996, 2001 and 2006 (NOAA 2011a). All three datasets use the same 25-class land use classification (Anderson *et al.* 1976 for upland and Cowardin *et al.* 1979 for wetlands) produced under a standardized procedure for all time periods for the coastal regions. These products are also incorporated into the NLCD (2001) dataset, although NOAA makes more detailed descriptions of coastal features such as wetlands.

The NWI was developed by the U.S. Fish and Wildlife Service from 1977 to the present, and is available at a 1:24.000 scale. The mapping was mostly performed by photo-interpretation and field work (Wilen and Tiner 1989), and a dataset dated in 1993 is available for the study area. The classification follows the Cowardin, *et al.* (1979) system which is hierarchical with five major groups, further divided into subsystems, classes and sub-classes.

COMPUTATIONAL METHODS

Surge model

We performed the hurricane storm surge simulations using the hydrodynamic model ADCIRC (Luettich and Westerink 2004). ADCIRC is a finite-element, shallow-water model that solves for water levels and current velocities at a range of scales, and is widely used for storm surge modeling (*e.g.,* Irish *et al.* 2005; Westerink *et al.* 2008; Ebersole *et al.* 2010; Dietrich *et al.* 2010, Bunya *et al.* 2010, and Dietrich *et al.* 2011).

We used the two dimensional depth integrated version of ADCIRC that solves the vertically integrated mass (Eq. 3.1) and the momentum equations (Eq. 3.2).

$$\frac{\partial h}{\partial t} + \nabla_h \left(\vec{U} h \right) = 0 \tag{3.1}$$

$$\frac{\partial \vec{U}}{\partial t} + \left(U \bullet \nabla_h \right) \vec{U} = -g \nabla_h \left(\zeta + \frac{p(x,y)}{g\rho} \right) + f \, \hat{k} \times \vec{U} + \frac{\vec{\tau_s}}{h\rho} - \frac{\vec{\tau_b}}{h\rho} \tag{3.2}$$

where h is the water depth, t is the time, ζ is the surge elevation above mean sea-level, $\vec{U}$ is the depth-averaged horizontal velocity vector, p is the barometric pressure, f is the Coriolis force, $\hat{k}$ is a vertical unit vector, τ_s is the free-surface shear stress, τ_b is the bottom shear stress and ρ is the water density.

We used a steady-state dynamical model, the TC96 developed by Thompson and Cardone (1996), to create the wind and pressure fields. The model computes wind stress, average wind speed and direction inside the Planetary Boundary Layer (PBL). The model assumes that the tropical cyclone structure changes slowly; thus, it can be represented using snapshots (e.g., 6 hours intervals) of its meteorological conditions: hurricane central pressure, radius of maximum speeds, storm track, Holland B parameter, and storm forward speed. The wind and pressure fields were generated every 15 min and interpolated between each snapshot. The model is based on the equation of

horizontal momentum, vertically averaged through the depth of the PBL (Thompson and Cardone 1996) (Eq. 3.3):

$$f \hat{k} \times \left(\vec{V} - \vec{V_g} \right) = -\frac{1}{\rho_{air}} \nabla C_p - \frac{C_D}{H} \left| \vec{V} - \vec{V_c} \right| \left(\vec{V} - \vec{V_c} \right) \tag{3.3}$$

where $\vec{V_g}$ is the geostrophic velocity vector at the low center, $\vec{V}$ is the averaged horizontal velocity vector, ρ_{air} is the air density, C_p is the pressure representing the tropical cyclone, $\vec{V_c}$ is the velocity vector of the moving reference system, C_D is the drag coefficient, and H is the depth of the PBL layer. A more detailed description of the TC96 model can be found at Thompson and Cardone (1996).

The numerical simulations were carried out using a validated computational mesh (Dietrich *et al.* 2011) for the State of Texas. This mesh contains approximately three million nodes with resolution up to 50 m in the study area and 2 km in the Atlantic Ocean. The tides were neglected due to their small amplitude (e.g., 0.17 m at NOAA station Port Ingleside in Corpus Christi Bay [NOAA 2012d]). The river inflows and wave setup were also neglected to simplify the analysis.

We reviewed the historical hurricane record (NOAA 2012c) and identified Hurricanes Bret (1999), Beulah (1967), Allen (1980) and Carla (1961) as indicative of typical hurricane meteorological conditions for the study area. Based on these storms, we

selected key meteorological hurricane parameters (central pressure, forward speed and radius to maximum wind). The TC96 steady-state dynamical model, developed by Thompson and Cardone (1996), was used to develop nine hypothetical storms based on historical parameters. The hypothetical storms represent three landfall locations (Figure 3.2), considering two maximum forward speeds (11.11 and 37.04 km/h), two maximum lower central pressure (930 and 960 mb) and one hurricane radius to maximum winds (31.48 km) (Table 3.1). These values represent common mid-range hurricane conditions for the study area (Resio *et al*. 2007). The storm ID represents its track, forward speed and central pressure.

Table 3.1: Meteorological parameters used to create the hypothetical storms (a)

ID	Track	Radius to maximum winds (km)	Forward Speed (km/h)	Central Pressure (mb)
A-11-960	A	31.48	11.11	960
A-37-960	A	31.48	37.04	960
A-37-930	A	31.48	37.04	930
B-11-960	B	31.48	11.11	960
B-37-960	B	31.48	37.04	960
B-37-930	B	31.48	37.04	930
C-11-960	C	31.48	11.11	960
C-37-960	C	31.48	37.04	960
C-37-930	C	31.48	37.04	930

The TC96 model was also used to generate wind and pressure fields for historical Hurricane Bret based on best historical track information (Andrew Cox, Oceanweather

Inc., personal communications, 2008) with six-hourly hurricane position, forward speed, size and central pressure, among other variables (Figure 3.2).
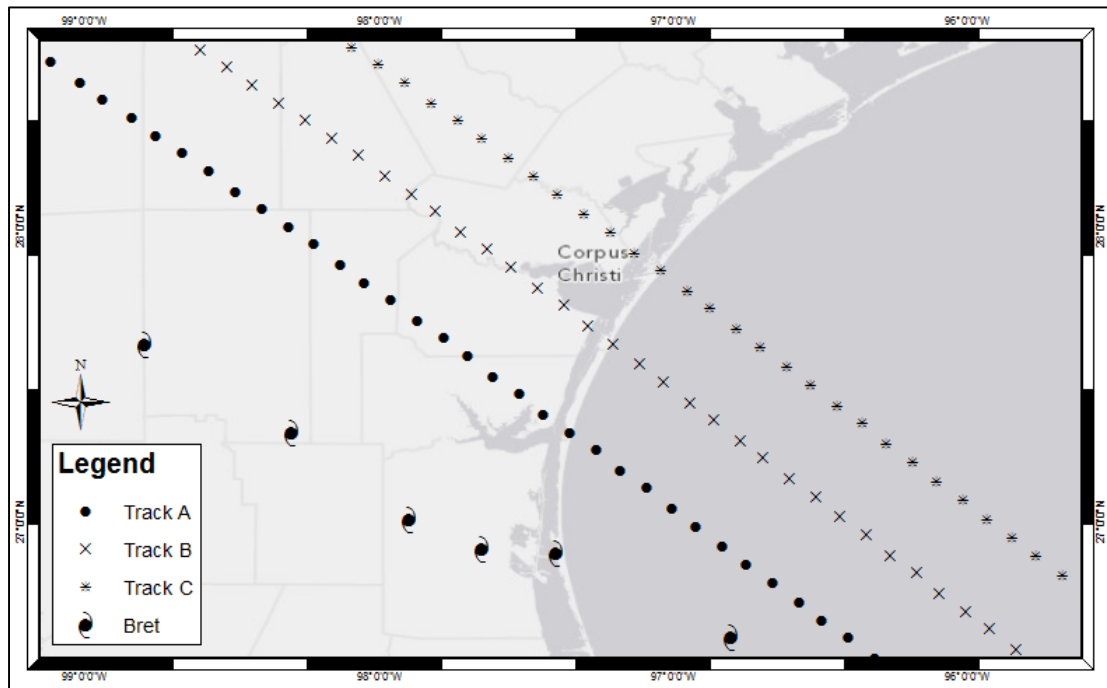
Figure 3.2: Synthetic storms tracks and the best track data for Hurricane Bret.

Effects of land cover

The dissipation mechanisms impacted by land cover are represented in the numerical model by the frictional drag at the sea bottom. The forcing mechanisms impacted by land cover are represented in the numerical model by changes in the transfer of momentum transmitted to the water column by the wind. These factors are spatially quantified by ADCIRC in three georeferenced parameters: 1) frictional drag at the sea

bottom (*Manning's n*); 2) the blocking effect of wind momentum transfer to the water column by vegetation and the built environment in the vicinity of the computational node (*Surface canopy*); and 3) the reduction of wind momentum transfer to the water column due to vegetation and the build environment upwind of a given computational node (*Land roughness length*). These parameters are assigned to each node in the mesh. A detailed description of the physics considered in defining land cover effects in ADCIRC is provided by Atkinson *et al.* (2011), and is summarized below.

a) *Frictional drag at the sea bottom*

The frictional drag at the sea bottom is incorporated into the momentum equation (Eq. 3.2) via the bottom shear stress term (τ_b). We considered the ADCIRC bottom friction formulation that uses Manning's *n* to represent the surface roughness of different land cover types. We adopted the following non-linear quadratic formulation for calculating the friction coefficient (Eq. 3.4)

$$C_f = g * \frac{n^2}{h^{(1/3)}}$$
(3.4)

where C_f is the friction coefficient, *g* is the gravitational constant; and *n* is the Manning's *n* roughness coefficient. The friction coefficient is incorporated into the bottom shear stress formulation by (Eq. 3.5):

$$\overline{\tau_b} = \frac{C_f \overline{U} |\overline{U}|}{h}$$

(3.5)

b) *Wind momentum transfer*

The changes in the momentum transferred by the wind to the water column are accounted for in ADCIRC in two ways:

1) Negligible penetration of momentum from the wind to the water column due to dense and high canopy vegetated areas and due to the built environment. To account for this effect, ADCIRC includes a *Surface Canopy* parameter, which modifies the free-surface shear stress term, τ_s, in the momentum equation (Eq. 3.2). The free-surface shear stress term can be represented by (Eq. 3.6):

$$\tau_s = \frac{C_d \rho_{air}}{h\rho} \|V\| V$$

(3.6)

The *Surface Canopy* parameter is set to zero in areas where the momentum transfer is blocked, resulting in zero wind shear stress (τ_s) at the nodes within these areas, and is set to one elsewhere.

2) Land cover also affects the wind speed due to increased frictional resistance to the air. To account for land cover effects on the wind speed, the full marine wind speed (V)

calculated by the TC96 model is replaced by a reduced wind speed (V_{land}) over the land (Eq. 3.7):

$$V_{land} = f_d V \qquad (3.7)$$

where the ratio of the full marine wind velocity and the wind velocity over the land (f_d) can be represented by (Eq. 3.8):

$$f_d = \left(\frac{Z_{marine}}{Z_0} \right)^{0.0706} \qquad (3.8)$$

where Z_{marine} and Z_o are the *marine* and *land roughness length* parameters, which are defined by the HAZUS software program (Federal Emergency Management Agency 2012) for each land cover type.

Georeferenced parameters

The Manning's *n*, *surface canopy* and the Z_o parameters values are specified based on the land cover type. For the C-CAP datasets (1996, 2001 and 2006) we used the values previously published by Dietrich *et al.* (2011) (Appendix D-1). The NLCD datasets have a different set of classes for the years of 1992 (23 classes), 2001 (29 classes) and 2006 (18 classes) resulting in three relational tables. Furthermore, for the 1992 dataset, slightly different values were presented by Atkinson *et al.* (2011) and Bunya *et al.*

(2010) compared to Wamsley *et al.* (2010). We selected our values to closely match the previous studies Appendix D-2. A set of suggested values is presented at the ADCIRC manual (Luettich and Westerink 2004) for the NLCD database of 2001 (Appendix D-3). We did not find any published values of Manning's *n*, *surface canopy* or Z_o for the NLCD of 2006. Although Dietrich *et al.* (2011) and Bunya *et al.* (2010) published values for some land cover classes that are also present in the NWI, a complete reference for this dataset was not found in any previously published study.

The Manning's *n* values that we estimated were selected based on the USGS Manning's *n* selection guide (Arcement and Schneider 1989). The values for the Z_o parameter estimated for land cover classes that were not available in the Federal Emergency Management Agency HAZUS publication (FEMA 2012) were obtained based on a linear regression relationship between existing Z_o values in HAZUS and subsequent Manning's *n* values. This linear regression is well correlated with an R^2 of 0.92. The adopted values for the NLCD 2006 and the NWI are presented in Appendix D-4 and Appendix D-5 respectively.

The Manning's *n* and surface canopy parameters are assigned unique values per mesh node. These values represent the entire area of influence of the given node, which is variable given the unstructured nature of the numerical mesh. We developed a Geographical Information System (GIS) framework to extract the friction information from the land cover datasets and to create the ADCIRC georeferenced parameters files.

We used an area weighted average approach modified from Atkinson *et al.* (2011). The Manning's *n* assigned to each node is based on Eq. 3.9 and the Surface Canopy parameter is assigned based on Eq. 3.10 as follows.

$$node_{Mannings'n} = \frac{\sum_1^j \left(\frac{(a_i * n)}{a_t} \right)}{\sum_1^j a_i} \tag{3.9}$$

$$node_{SurfaceCanopy} = \begin{cases} 0, & \frac{\sum_1^j \left(\frac{(a_i * SC)}{a_t} \right)}{\sum_1^j a_i} < 0.75 \\ 1, & \frac{\sum_1^j \left(\frac{(a_i * SC)}{a_t} \right)}{\sum_1^j a_i} \geq 0.75 \end{cases} \tag{3.10}$$

where *n* is the Manning's *n* values in a given raster cell, a_i is the area of the raster cell inside the node influence area, a_t is the total area of the raster cell, *j* is the number of cells inside a given node area of influence, and *SC* is the surface canopy value for a given raster cell. The extraction of the Z_0 parameter per node was performed based on the Atkinson *et al.* (2011) methodology resulting in twelve values per mesh node. These twelve values represent the weighted average of the Z_o parameter in a radius of 3km from the node, equally divided in 12 sectors. These sectors represent all possible upwind directions from each computational node.

Manning's n variation by land cover dataset

Spatially variable parameter values were generated for Manning's *n*, the surface canopy coefficient and the z_o, considering each of the seven land cover datasets. There is a direct relation between the three parameters due to their dependence on land cover type, resulting in similar spatial patterns for each parameter. Thus, the following discussion focuses on the Manning's *n* parameter. We calculated the Manning's *n* variances resultant from the datasets, representing the spatial difference between two datasets for a given parameter.

The results showed that, with the C-CAP datasets, it is very hard to discern a change in the parameters within its time period. We found the same mean Manning's *n* value (μ_n=0.055, s_n=0.032) for the 1996, 2001 and 2006 datasets. Most of the changes, between the years of 1996 and 2001, are in areas not susceptible to flooding, with the exception of some small areas in Matagorda Island. From 2001 and 2006, although it is possible to observe some spatial differences in Manning's *n,* which decreases by (-0.05) on the barrier islands fronting Corpus Christi Bay and areas north of Baffin Bay, and increases by (+0.05) in Port Ingleside, and Oso Bay, the overall mean value is the same.

Unlike the C-CAP datasets, there are greater differences in Manning's *n* among the NLCD datasets. It is important to note that there is a change in the classification scheme from 1992 to 2001; thus, the comparison might be misleading in some cases, but areas of clear change can still be identified. The overall mean Manning's *n* varied from

(μ_n=0.048,σ_n=0.021) in 1992 to (μ_n=0.041,σ_n=0.022) in 2001 and (μ_n=0.044,σ_n=0.029) in 2006. The reduction in Manning's n from 1992 to 2001 occurred mostly in wetland areas around the Aransas Pass and Corpus Christi Bay regions. From 2001 to 2006 the mean Manning's n increased mainly due to changes in areas of Aransas Bay.

When comparing the current datasets, the NWI (2011) has the highest Manning's n mean (μ_n=0.0757, σ_n=0.040). The greater detail in wetland delineation from the NWI leads to higher Manning's n areas inside the bays, especially in the Aransas Pass area and behind Matagorda Island.

STORM SURGE VALIDATION

Hurricane Bret made landfall in 1999, in south Texas, close to the City of Corpus Christi. Hurricane Bret was a category 3, with winds of around 185 km/h, and central pressure of 944 mb (NOAA, 2001). This storm caused significant damage to southern Texas and northern Mexico coastal communities. We compared the simulated data with recorded water levels from the Texas Coastal and Oceanic Observation Network (TCOON) (7 stations) and from NOAA (2 stations) (Figure 3.3). Seven separate simulations were made, such that each land cover dataset is represented.
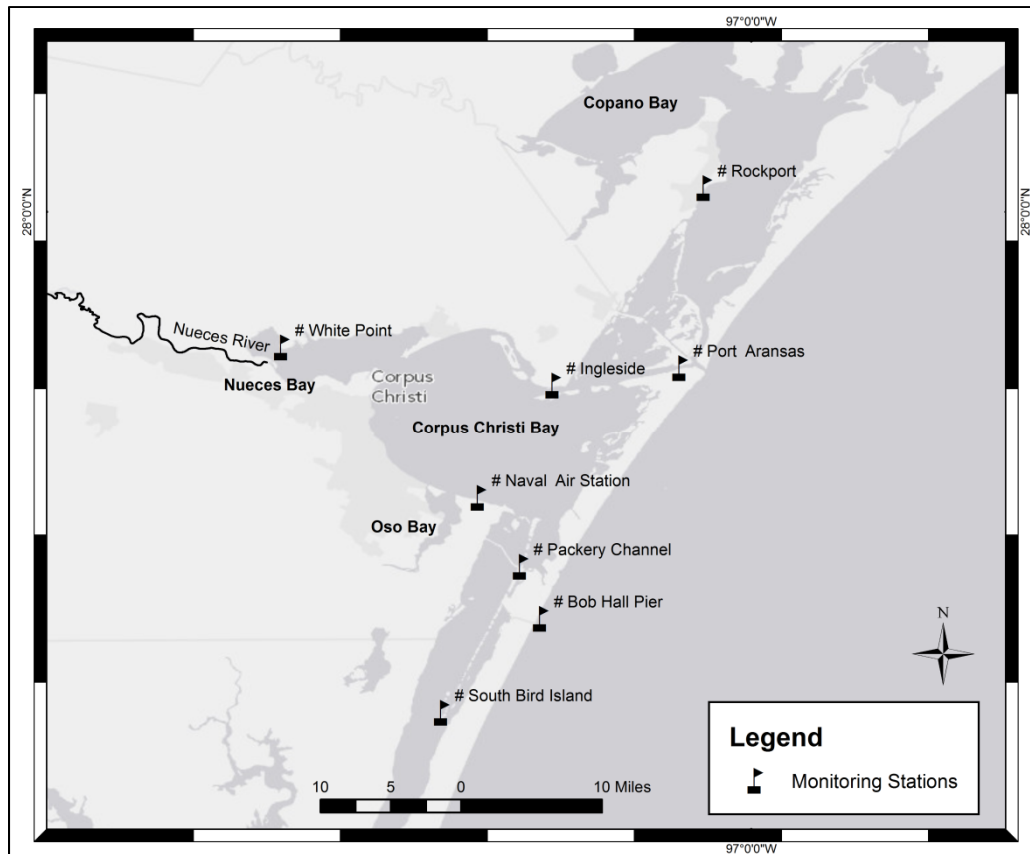
Figure 3.3: The Texas Coastal and Oceanic Observation Network (TCOON) gage stations with recorded data for Hurricane Bret.

The land cover dataset did not impact the simulated surge at the Bob Hall Pier location. This result was expected as for all simulations there is no land cover changes off shore. All simulations underestimated the peak surge by 0.20 m at the open coast station (Bob Hall Pier). In the Naval Air Station, all the datasets underestimated the peak surge. The C-CAP datasets and the NLCD 2001 and the NWI were 0.10 m below the recorded value. The other datasets were only 0.05 m below the recorded value. In Rockport, the NLCD 2006 and 1992 were only 0.50 m below the recorded value and the other datasets were approximately 0.10 m below the recorded value. In Port Aransas, the peak surges

were overestimated by approximately 0.10 m by all the datasets. In Ingleside, the NWI and the C-CAP matched exactly the measured value. The other datasets were at most 0.05 m off. In South Bird Island all the simulations overestimated the peak by approximately 0.10 to 0.15 m.

A root mean square error (RMSE) of around 0.1 m was registered for almost all simulations. In Figure 3.4, a scatter plot comparing the measured and simulated peak surges at each station is presented. The lowest RMSE was found with the NLCD 2001 dataset (RMSE=0.0848), which also presented the lowest mean surges in the study regions. As Hurricane Bret made landfall in 1999, the time period of this dataset is the closest to the hurricane landfall date, demonstrating the importance of correctly representing land cover for storm surge modeling. The NWI dataset resulted in the second lowest error (RMSE=0.0956), which we attribute to the higher resolution defining wetlands and other coastal vegetation. We could not identify a trend towards a positive or negative bias when using any particular land cover dataset. The worst matching (~0.20m) was found at Packery channel, which is the result of the changes in bathymetry caused by the construction of Packery channel (circa 2005) included in the computational mesh, but inexistent during Hurricane Bret passage.
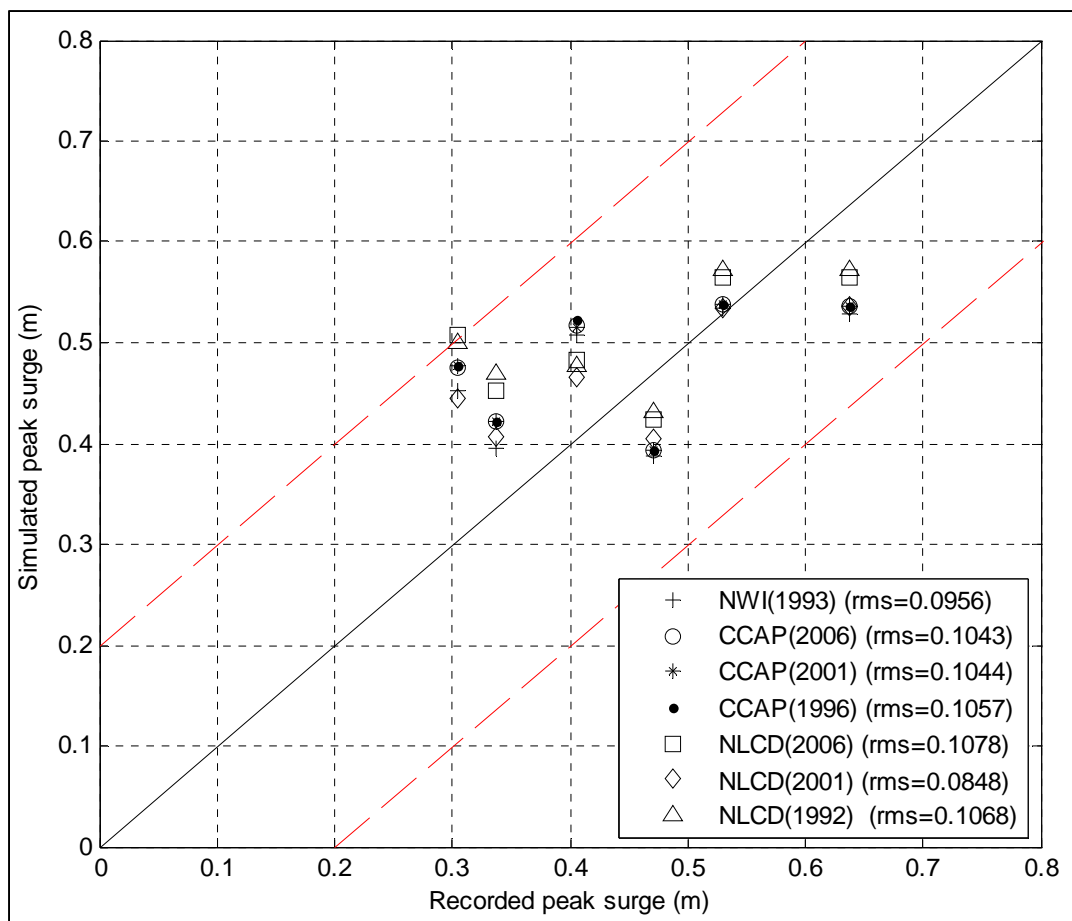
Figure 3.4: Simulated and measured peak surge for 7 TCOON stations and 2 NOAA stations considering the seven land cover datasets for Hurricane Bret.

RESULTS AND DISCUSSION

Influence of land cover specification on surge height predictions

The maximum surge height was measured at 688 locations, throughout eleven sub regions of the study area (sub regions are presented in Figure 3.5):
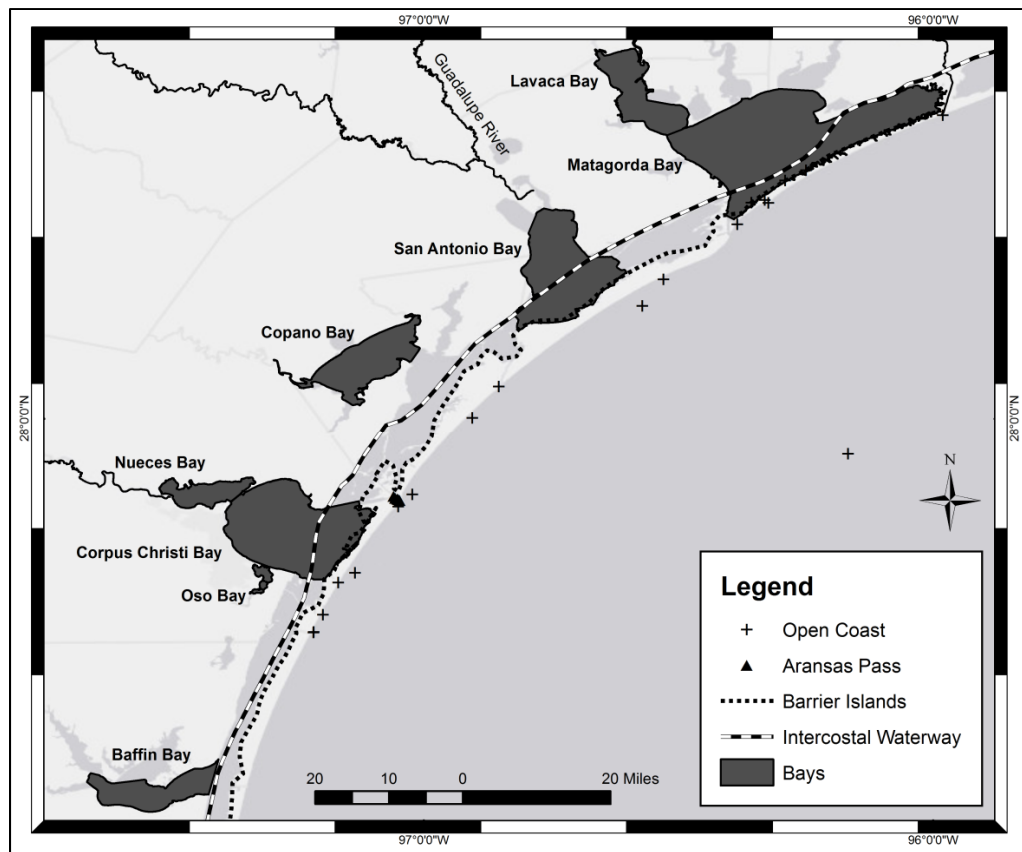
Figure 3.5: Central Texas bays and the study area locations divided by the sub-regions: 8 bays, areas behind the barrier island, the open coast, Aransas Pass and the Intercoastal Waterways.

1) Along the Intercoastal Waterway (90 points);

2) Aransas Pass (28 points);

3) Corpus Christi Bay (54 points);

4) Nueces Bay (40 points);

5) Oso Bay (36 points);

6) Locations immediately behind the barrier island (102 points);

7) Along the margins of the Corpus Christi Bay (55 points);

8) Along the margins of Nueces Bay (30 points);

9) Matagorda Bay (59 points);

10) Copano Bay (48 points);

11) Along the open coast (22 points);

A detailed view of the recording points within the bays is presented in Figure 3.6.
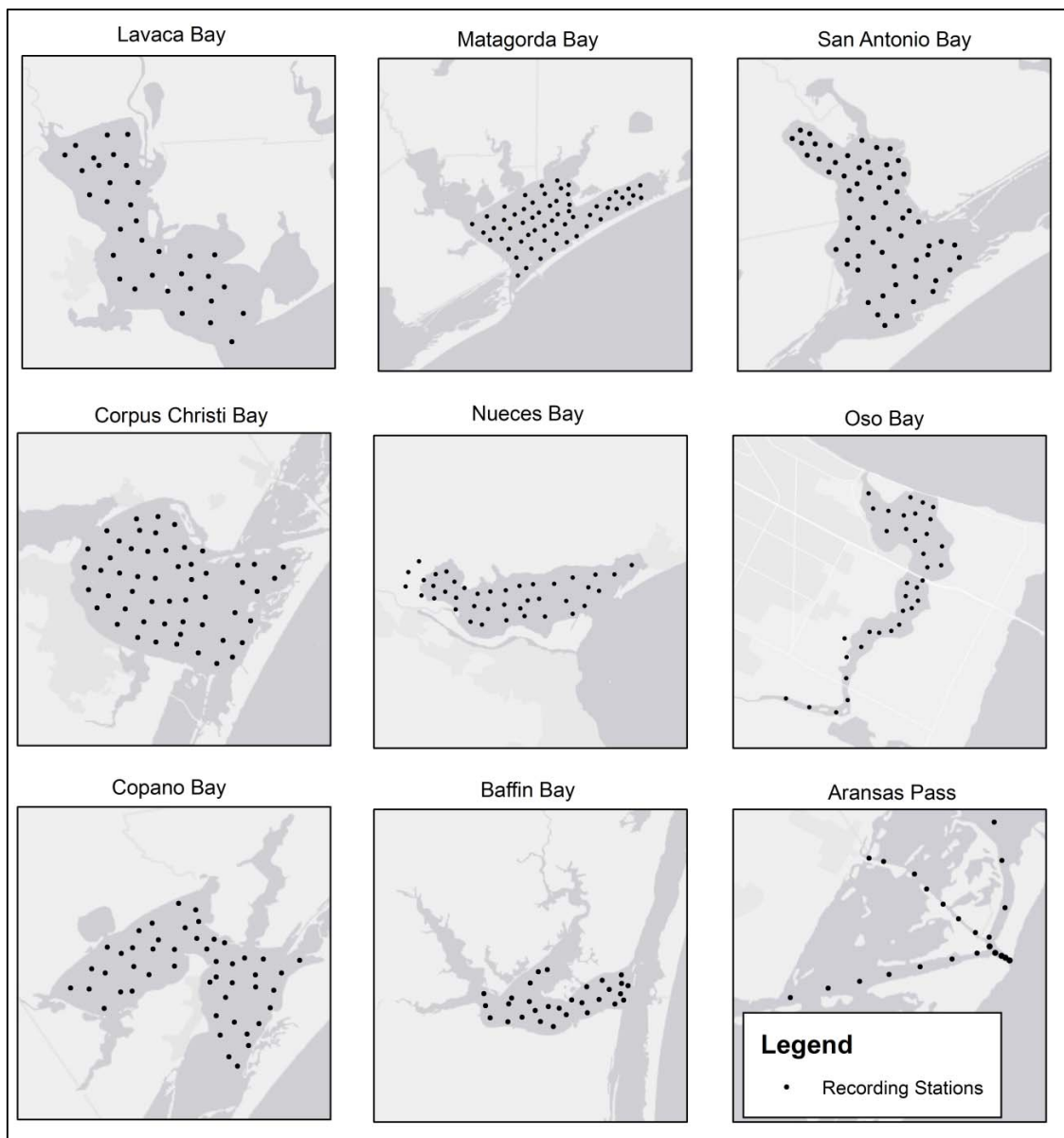
Figure 3.6: Placement of recording points within the coastal bays (a).

Here, the mean maximum surge ($\mu_{\zeta max}$) is the average of the maximum surge recorded within the points of each sub-region. We applied Analysis of Variance (ANOVA) to compare the mean maximum surge response from the 7 land cover datasets for each storm condition. To investigate if the land cover affected the mean maximum surge response, the null hypothesis is that all the means are the same for a given sub-region under a given storm condition. The null hypothesis would be rejected if at least one mean is different under a 95 % confidence:

H_o: $\mu_{ccap1996} = \mu_{ccap2001} = \mu_{ccap2006} = \mu_{nlcd1992} = \mu_{nlcd2001} = \mu_{nlcd2006} = \mu_{nwi2011}$;

H_1: *at least one mean is different*; $p < 0.05$.

The null hypothesis was rejected with 95% confidence in all bays for at least one storm condition, leading to the conclusion that the land cover dataset choice does significantly impact the surges at these locations. The null hypothesis could not be rejected for the open coast, Intercoastal Waterway and Aransas Pass sub regions, indicating that land cover changes do not significantly impact the mean maximum surge along the open coast (Table 3.2). These results were expected once the off-shore regions are not affected by the differences in the land cover datasets. The frictional drag at the sea bottom and the momentum transmitted to the water column is the same for all simulations off shore. As expected, land cover plays an important role only in the locally generated surge.

Table 3.2: ANOVA test results when comparing the mean surge for the NLCD (1992, 2001, and 2006), C-CAP (1996, 2001, and 2006) and NWI (2011) datasets. (p-values)

Storm / Location	A-11-960	A-37-960	A-37-930	B-11-960	B-37-960	B-37-930	C-11-960	C-37-960	C-37-930
Intercoastal Waterway	0.44	0.40	0.17	0.90	0.83	0.35	0.80	0.62	0.10
Aransas Pass	0.98	0.95	0.77	0.99	0.79	0.39	1.00	1.00	0.87
Corpus Christi Bay	0.17	0.51	0.21	0.40	0.25	0.00	0.77	0.30	0.29
Nueces Bay	0.07	0.00	0.00	0.00	0.00	0.00	0.69	0.00	0.00
Oso bay	0.44	0.00	0.00	0.27	0.00	0.00	0.20	0.00	0.00
Barrier Island	0.24	0.65	0.32	0.49	0.72	0.15	0.77	0.43	0.02
Margins of Corpus Christi Bay	0.95	0.65	0.17	0.02	0.01	0.00	1.00	0.45	0.46
Margins of Nueces Bay	0.46	0.05	0.02	0.00	0.00	0.00	1.00	0.00	0.00
Matagorda Bay	1.00	0.16	1.00	0.99	0.17	0.00	0.99	0.12	0.00
Copano Bay	0.00	0.03	0.95	0.01	0.00	0.00	0.05	0.00	0.00
Open Coast	1.00	1.00	1.00	1.00	1.00	1.00	1.00	1.00	1.00
Lavaca Bay	0.99	0.50	0.02	0.97	0.38	0.23	0.91	0.34	0.03
San Antonio Bay	0.56	0.50	0.98	0.75	0.11	0.00	0.85	0.00	0.00
Baffin Bay	0.02	0.75	0.87	0.16	0.60	0.90	0.03	0.18	0.74

We also compared the mean maximum surge within the C-CAP dataset 10-year time interval (1996~2006). The variances in the surge response due to changes in land cover within this period were compared considering the null hypothesis that all the means are the same. The null hypothesis would be rejected if at least one mean is different.

H_o: $\mu_{ccap1996} = \mu_{ccap2001} = \mu_{ccap2006}$

H_1: *at least one mean is different* under a 95 % confidence ($p < 0.05$).

We could not find a significant difference in the mean surge response when comparing the C-CAP datasets for different time periods (Table 3.3). The null hypothesis (all the means are the same) could not be rejected with a confidence of 95% for all the meteorological conditions tested at each of the study locations. This result was expected and aligns with negligible Manning's *n* changes over time in this dataset. In summary, the coastal land cover changes captured in this dataset from 1996 to 2006 were not sufficient to affect the mean maximum surge within the study area.

Table 3.3: ANOVA test results when comparing the mean surge for the C-CAP (1996, 2001, and 2006) datasets. (p-values)

Storm / Location	A-11-960	A-37-960	A-37-930	B-11-960	B-37-960	B-37-930	C-11-960	C-37-960	C-37-930
Intercoastal Waterway	1.00	1.00	1.00	1.00	1.00	1.00	1.00	1.00	1.00
Aransas Pass	1.00	1.00	1.00	1.00	1.00	1.00	1.00	1.00	1.00
Corpus Christi Bay	1.00	1.00	0.99	1.00	1.00	0.95	1.00	1.00	1.00
Nueces Bay	1.00	1.00	0.98	1.00	0.96	0.81	0.99	1.00	0.92
Oso bay	1.00	1.00	1.00	1.00	1.00	1.00	1.00	1.00	1.00
Barrier Island	1.00	1.00	1.00	1.00	1.00	0.99	1.00	0.99	0.99
Margins of Corpus Christi Bay	1.00	1.00	0.99	1.00	1.00	0.97	1.00	1.00	1.00
Margins of Nueces Bay	1.00	1.00	1.00	1.00	0.99	0.95	1.00	1.00	1.00
Matagorda Bay	1.00	1.00	1.00	1.00	1.00	1.00	1.00	1.00	1.00
Copano Bay	1.00	1.00	1.00	1.00	1.00	0.97	1.00	0.98	0.97
Open Coast	1.00	1.00	1.00	1.00	1.00	1.00	1.00	1.00	1.00
Lavaca Bay	1.00	1.00	1.00	1.00	1.00	1.00	1.00	1.00	1.00
San Antonio Bay	1.00	1.00	1.00	1.00	1.00	0.92	1.00	0.97	0.84
Baffin Bay	1.00	1.00	1.00	1.00	1.00	1.00	1.00	1.00	1.00

In contrast to the C-CAP analysis, the land cover changes captured in the NLCD between 1992 and 2006 do significantly affect the mean surge in the study area. The variances in the surge response due to changes in land cover within this time period were compared with the null hypothesis that all the means are the same and the null hypothesis would be rejected if at least one mean is different.

H_o: $\mu_{nlcd1992}=\mu_{nlcd2001}=\mu_{nlcd2006}$

H_1: *at least one mean is different* under a 95 % confidence (p < 0.05)

Note that the change in the classification scheme between NLCD 1992 and 2001 might have affected the friction parameter values at specific points and this change could have also impacted the surge response. Similar to when comparing all the datasets, the locations that were most significantly affected by the changes in land cover were Oso Bay, Nueces Bay, Matagorda Bay and Copano Bay. There were no significant changes in the mean maximum surge in the Intercoastal Waterway, behind the barrier islands, Lavaca Bay, Baffin Bay and Aransas Pass (Table 3.4). Lavaca and Baffin bays are the most distant bays from any simulated landfall location, thus it is expected that they would be less sensitive to the impacts of the hurricanes. Although in all the bays sub regions there was a mean surge reduction from 1992 to 2001, Matagorda and Copano bays presented a slight increase from 1992 to 2006 (~0.1 m). In Oso Bay, the mean surge decreased, from 1992 to 2001, on the order of 0.5 m and then followed a slight

increase of 0.1 m from 2001 to 2006 for the stronger storms. The same trend was observed for other storms, but with a slightly smaller surge reduction of 0.3 m.

Table 3.4: ANOVA test results when comparing the mean surge for the NLCD (1992, 2001, 2006) datasets. (p-values)

Storm / Location	A-11-960	A-37-960	A-37-930	B-11-960	B-37-960	B-37-930	C-11-960	C-37-960	C-37-930
Intercoastal Waterway	0.41	0.34	0.59	0.66	0.61	0.55	0.65	0.56	0.56
Aransas Pass	0.58	0.60	0.52	0.72	0.47	0.43	0.79	0.78	0.67
Corpus Christi Bay	0.04	0.38	0.46	0.19	0.44	0.15	0.90	0.27	0.44
Nueces Bay	0.72	0.58	0.52	0.01	0.00	0.00	0.70	0.00	0.00
Oso bay	0.15	0.00	0.00	0.11	0.00	0.00	0.19	0.00	0.00
Barrier Island	0.56	0.44	0.78	0.54	0.37	0.57	0.66	0.45	0.52
Margins of Corpus Christi Bay	0.89	0.78	0.66	0.08	0.15	0.16	0.96	0.23	0.30
Margins of Nueces Bay	0.67	0.60	0.91	0.03	0.04	0.05	0.95	0.01	0.01
Matagorda Bay	0.87	0.10	0.86	0.80	0.07	0.01	0.71	0.11	0.00
Copano Bay	0.05	0.03	0.53	0.09	0.00	0.00	0.15	0.00	0.00
Open Coast	0.99	1.00	1.00	1.00	1.00	1.00	1.00	1.00	1.00
Lavaca Bay	0.88	0.76	0.62	0.85	0.69	0.42	0.79	0.62	0.24
San Antonio Bay	0.51	0.51	0.95	0.63	0.42	0.02	0.75	0.40	0.12
Baffin Bay	0.88	0.95	0.94	0.97	0.79	0.85	0.88	0.65	0.76

In order to evaluate the variance within the most current coverage of each dataset, we compared if there is a significant difference in the mean maximum surge response. The null hypothesis for this analysis is that the mean maximum surge of the NLCD (2006), C-CAP (2006) and NWI (2011) are the same and the null hypothesis would be rejected if at least one mean is different.

H_o: $\mu_{ccap2006} = \mu_{nlcd2006} = \mu_{nwi2011}$

H_1: *at least one mean is different* under a 95 % confidence (p < 0.05)

The null hypothesis was rejected with 95% confidence for all study locations except the open coast and the Aransas Pass for at least one storm condition. At the Intercoastal Waterway, the storms with lower central pressure produced significantly different mean surges (95% confidence). In Corpus Christi Bay, we found significant differences in the mean surge for all three lower central pressure storms and the fast moving storm in the central track (B). In Nueces Bay, almost every storm produced significantly different results with the exception of the weaker and slow moving storms on tracks A and C. In Oso Bay, the lower pressure and fast moving storms on tracks B and C produced significantly different mean surges. Immediately behind the barrier island, the stations registered significantly different mean surges for all the lower pressure storms and also for the western (track C) fast moving storms. In Matagorda Bay, the lower pressure and fast moving storms on tracks B and C produced statistically different mean surges. In Copano Bay, we found significantly different mean surges for all storms besides the lower pressure storm on the track A (Table 3.5).

To quantify the impacts of the differences in the frictional drag at the sea bottom represented by the Manning's *n* parameter from the land cover datasets; we calculated the mean Manning's *n* value for each dataset. As expected, the increase in friction

reduced the mean maximum surge. We found a negative linear relationship between the

datasets mean Manning's *n* values and the mean maximum surge (Figure 3.7).

Table 3.5: ANOVA test results when comparing the mean surge for the NLCD (2006), C-CAP (2006) and NWI (2011) datasets. (p-values)

Storm / Location	A-11-960	A-37-960	A-37-930	B-11-960	B-37-960	B-37-930	C-11-960	C-37-960	C-37-930
Intercoastal Waterway	0.20	0.10	0.02	0.56	0.35	0.07	0.50	0.17	0.01
Aransas Pass	0.96	0.93	0.71	0.99	0.68	0.29	0.99	0.90	0.52
Corpus Christi Bay	0.12	0.13	0.02	0.25	0.04	0.00	0.49	0.11	0.06
Nueces Bay	0.15	0.03	0.00	0.00	0.00	0.00	0.47	0.00	0.00
Oso bay	0.60	0.46	0.17	0.48	0.00	0.00	0.35	0.03	0.02
Barrier Island	0.21	0.21	0.06	0.29	0.38	0.03	0.54	0.10	0.00
Margins of Corpus Christi Bay	0.78	0.54	0.05	0.06	0.00	0.00	0.87	0.20	0.12
Margins of Nueces Bay	0.46	0.20	0.07	0.02	0.00	0.00	0.91	0.01	0.00
Matagorda Bay	0.88	0.07	0.86	0.85	0.05	0.00	0.79	0.02	0.00
Copano Bay	0.05	0.04	0.66	0.08	0.00	0.00	0.11	0.00	0.00
Open Coast	0.99	1.00	0.99	1.00	1.00	1.00	1.00	1.00	1.00
Lavaca Bay	0.81	0.33	0.04	0.76	0.25	0.09	0.64	0.19	0.01
San Antonio Bay	0.25	0.24	0.74	0.34	0.03	0.00	0.43	0.00	0.00
Baffin Bay	0.03	0.55	0.47	0.11	0.46	0.74	0.03	0.19	0.58

This relationship can be expressed by (Eq. 3.11) with an R^2 of 0.91:

$$\mu_{\zeta\max} = -9.767 * \eta + 1.889 \tag{3.11}$$

where $\mu_{\zeta\max}$ is the mean maximum surge in m and η is the mean Manning's *n* value.
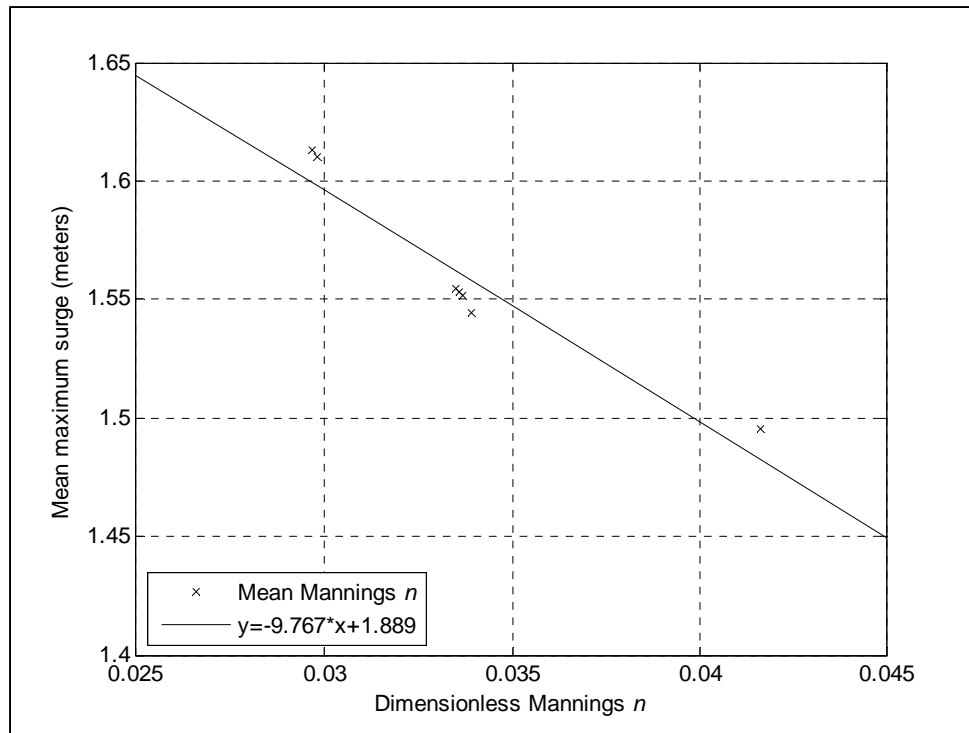
Figure 3.7: Relationship between the mean Manning's *n* value for a dataset and the mean maximum surge for all 6003 recording stations.

Influence of land cover specifically on extent of inundation

Similar to the mean maximum surge results, there is no significant difference in the inundated area when considering the C-CAP databases for 1996, 2001 and 2006. When considering the NLCD databases, the total inundated area did vary considerably and consistently for every storm depending on the database year. Larger inundated areas were found when using the 1992 and the 2006 with respect to 2001. The residuals (difference from the mean) in inundated areas varied in the order of 100 square kilometers. On the other hand, the NWI led to the smallest inundation extents with respect to the other datasets, with a residual of at least 50 square kilometers from the

mean. When comparing the most recent coverage from each dataset (C-CAP 2006, NLCD 2006 and NWI 2011), the C-CAP dataset produced flooded extents that were very close to the mean value between the three datasets (residuals from -2 to 59 km^2), the NWI had the lowest flooded extents (residuals from -35 to -181 km2), and the NLCD resulted in the largest flooded extents (residuals from 38 to 124 km2).

We found a strong positive linear correlation between the mean maximum surge residuals and the inundated area residuals (Figure 3.8). When comparing the most recent datasets (C-CAP [2006], NLCD [2006] and NWI [2011]) we found that the inundated area residual can be represented by (Eq. 3.12):

$$\Psi_{residual} = 755.1 * \mu_{residual} + 23.56 \tag{3.12}$$

where $\Psi_{residual}$ is the flooded area extent residual in square kilometers and $\mu_{residual}$ is the mean surge residual in m, with an R^2 of 0.76 and a RMSE of 36.43 square kilometers considering a least squares linear interpolation.
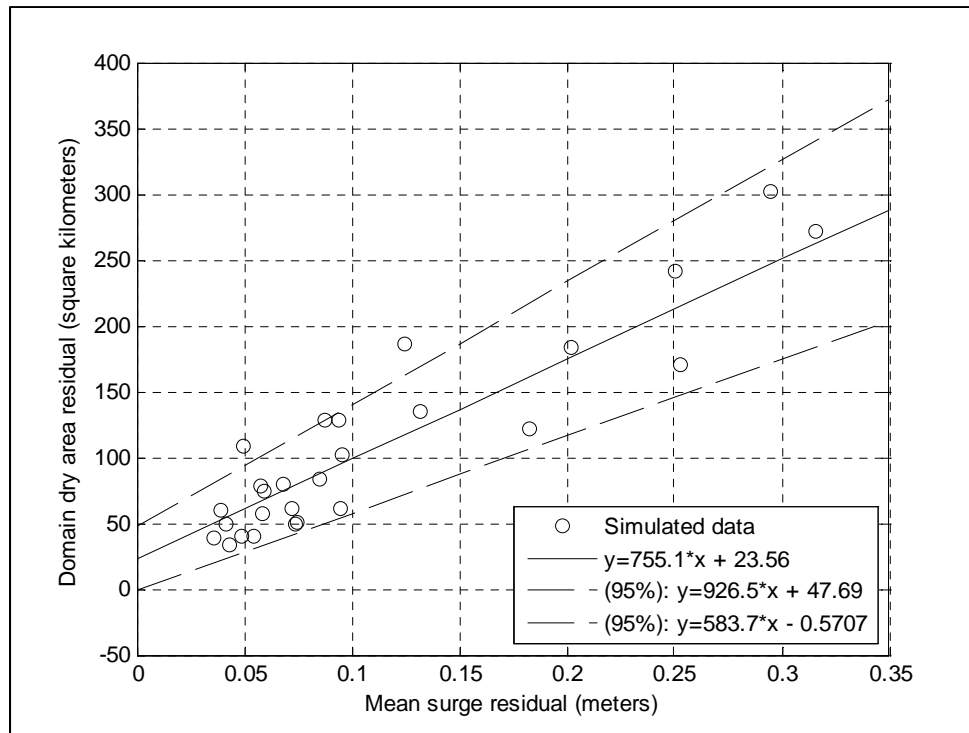
Figure 3.8: Linear relationship using least squares between the inundation residuals and the mean surge anomaly considering the C-CAP (2006), the NLCD (2006) and the NWI (2011) datasets.

Quantification of uncertainty

To quantify the estimated residual in the surge response, we calculated the difference between the maximum surges at each recording location for the most current year of each dataset. The mean residual is calculated based on (Eq. 3.13):

$$\mu_{residual} = \frac{\sum_1^k \sum_1^m \frac{\left|\zeta_{k(ccap)} - \zeta_{k(nlcd)}\right| + \left|\zeta_{k(ccap)} - \zeta_{k(nwi)}\right| + \left|\zeta_{k(nwi)} - \zeta_{k(nlcd)}\right|}{3}}{m*k}$$ (3.13)

where $\mu_{residual}$ is the mean surge residual; k is the number of recording locations; m is the number of storms; and $\zeta_{k(dataset)}$ is the surge level at a given location for a given land cover database.

The overall mean surge residual calculated using (Eq. 3.13), considering the 6003 data points, was 0.11 m with a standard deviation of 0.12 m. The surge residuals are extremely variable and strongly related to spatial location and meteorological conditions (Figure 3.9). The maximum anomaly is on the order of 1.00 m in a few locations, and several locations presented variations over 0.50 m.

A closer analysis of the surge residuals with respect to the meteorological forcing conditions reveals a strong correlation between the mean surge residual and the storm forward speed and central pressure. The larger mean residuals are associated with the lowest central pressure storms (B-37-930: μ=0.23m and σ=0.13m; A-37-930: μ=0.18m and σ=0.18m; C-37-930: μ=0.18m and σ=0.17m) with values much higher than the overall average. These are also in accordance with the mean surge significant differences found in the ANOVA analyses, being mostly caused by the lower central pressure storms. The fast moving storms yield mean surge residuals in alignment with the overall mean (A-37-960: μ=0.08m and σ=0.05m; B-37-960: μ=0.10m and σ=0.05m; C-37-960: μ=0.08m and σ=0.07m) and the slow moving storms resulted in a very low residual between the datasets (A-11-960: μ=0.05m and σ=0.04m; B-11-960: μ=0.04m and

σ=0.03m; C-11-960: µ=0.04m and σ=0.03m) even below the overall mean. From these analyses, we concluded that the lower pressure storms yielded surge residuals on the order of 0.2 m; the high pressure, fast moving storms yielded surge residuals on the order of 0.1 m; and the slow moving and high pressure storms, residuals on the order of 0.05 m.
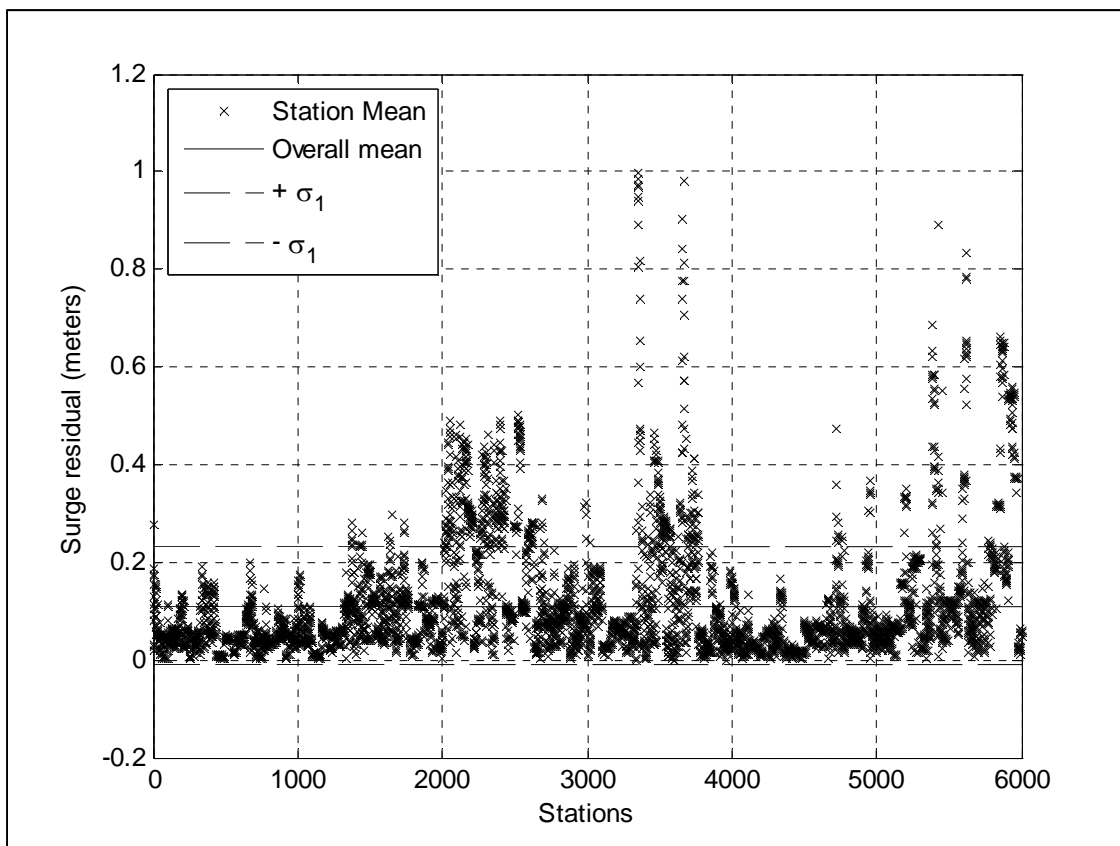
Figure 3.9: Mean maximum surge residuals considering all the recording stations and all storm conditions (6003).

Although the storm track did not significantly impact the mean maximum surge for the entire study area, the proximity to the storm eye had an impact on the mean maximum surges for the study sub-regions. The highest surge residuals always occurred close to the hurricane eye, with residuals greater than 0.5 m always located within 100 km of the hurricane eye. The greater residuals were located on the right side of the storms, whew highest wind surge typically occurs. Locations in a distance greater than 200 km from the storm eye did not present residuals greater than 0.2 m for any storm condition. Locations on the left hand side of the storm track also did not present residuals greater than 0.2 m for any storm condition. In summary, we found that for every simulation, the greater residuals were within 100 km distance from the right hand side of the storm track (Figure 3.10).

Considering the residuals spatial variation, the sub regions with higher sensitivity to land cover changes (surge anomalies > 0.5 m) were the Intercoastal Waterway, areas immediately behind the barrier islands, Corpus Christi Bay, Copano Bay and San Antonio Bay (Figure 3.11).
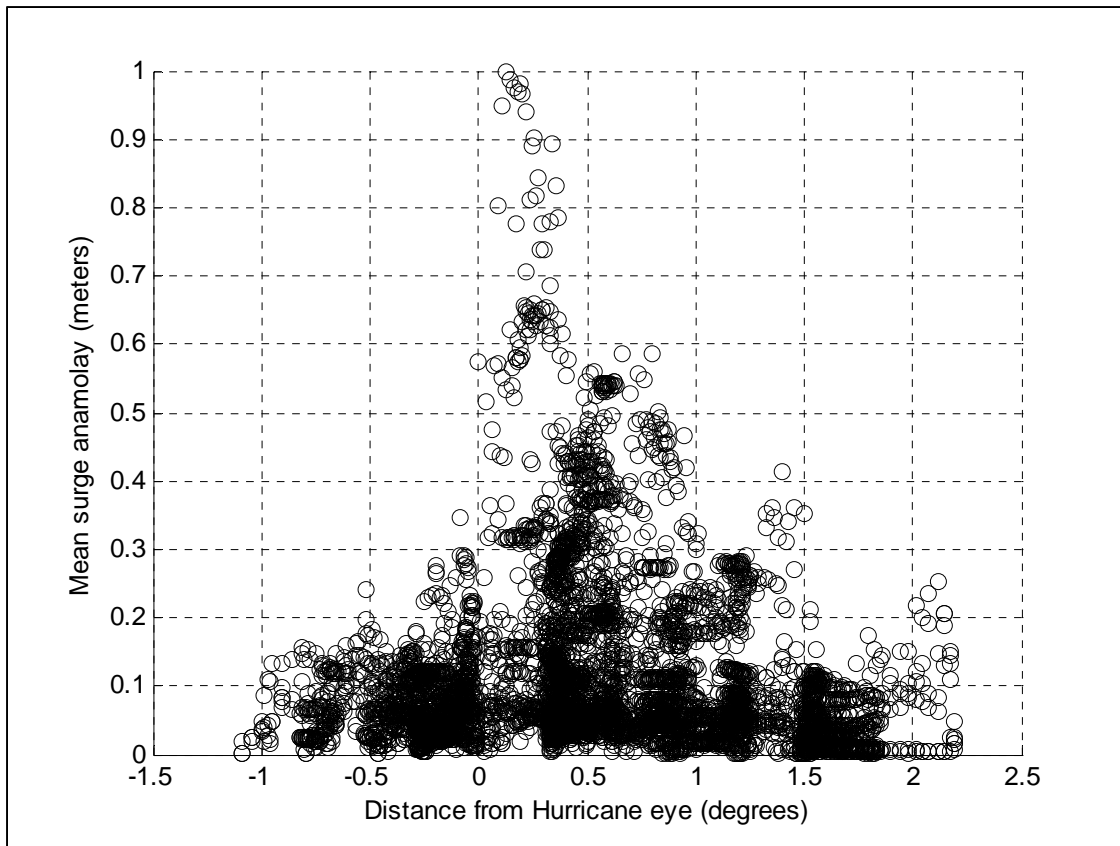
Figure 3.10: Effects of the distance from the hurricane eye to the recording location on the mean maximum surge anomalies considering the NLCD (2006), C-CAP (2006) and the NWI (2011) datasets. Negative values represent the left hand side of the storm.
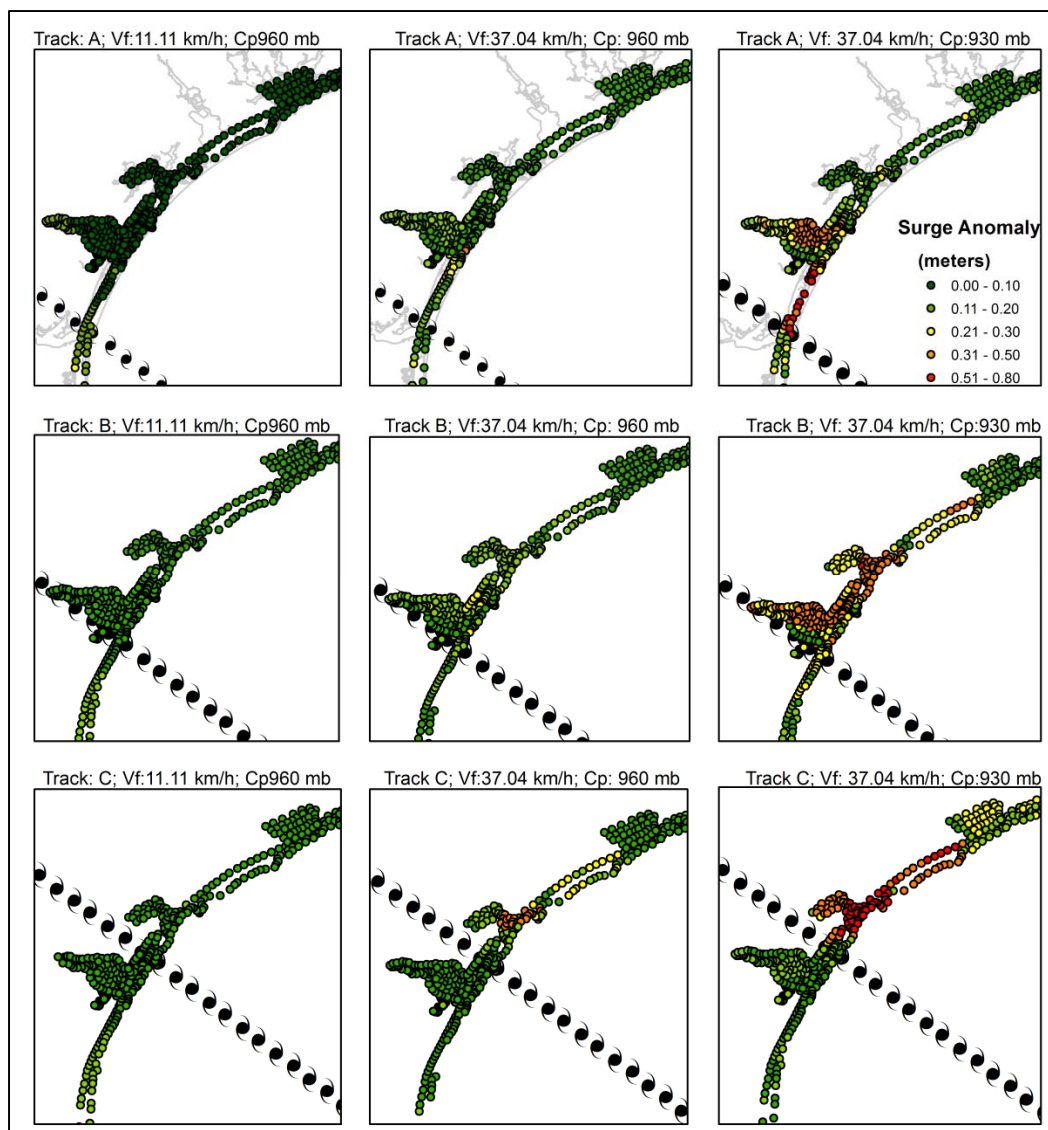
Figure 3.11: Spatial mean maximum surge residuals considering simulation using the NLCD (2006), C-CAP (2006) and the NWI (2011) datasets.

The highest residuals occurred in the sub region behind the barrier island, mostly due to the wide presence of wetlands (mapped differently in the different land cover datasets); these residuals reached values up to 1 m in the stronger storms. Although the Intercoastal Waterway sub region had an overall low mean residual, it presented a large variance and a strong presence of outliers (up to 1 m at selected recording points). Nueces Bay

presented residuals larger than Corpus Christi Bay for weaker storms but Corpus Christi Bay had larger residuals for stronger storms. Corpus Christi Bay is more sensitive to the storm intensity as it has a larger surface area than Nueces Bay. Also, larger residuals were found on the northeastern side of the bays when the storm track was located south of the bays. This trend is inverted to the southwest when the storm track was north of the bays. This can be explained by the change on the predominant wind direction, indicating that the residuals increase towards the wind direction inside the bays. The residuals at Oso Bay were always below 0.3 m indicating a low sensitivity to land cover in this area with respect to the neighboring bays (Corpus Christi and Nueces). We believe that the low sensitivity at Oso Bay is related to its relative small surface area, which does not allow for locally generated surge.

SUMMARY AND CONCLUSIONS

Land cover plays an important role in hurricane surge numerical modeling because of its impacts on the forcing and dissipation mechanisms of storm surge. Here we investigated the surge response in coastal bays from different land cover datasets (C-CAP [1996, 2001 and 2006], NLCD [1992, 2001 and 2006] and NWI [2011]) for a set of hypothetical storm meteorological conditions.

We found significant differences in the mean maximum surges when comparing all the datasets available for the region. The differences in land cover change over time captured by the C-CAP (1996-2006) dataset did not produce any significant difference

on the mean maximum surge response. On the contrary, when considering the NLCD dataset, we found significant changes in the mean maximum surge over the time period of the dataset (1992-2006). When comparing the most recent datasets from the C-CAP, NLCD and NWI datasets, we also found significantly different mean maximum surges. In contrast to the response in coastal bays, the land cover does not have a significant impact on the surge response for the locations along the open coast and Aransas Pass.

A case study considering Hurricane Bret demonstrated that there is no bias towards any dataset, and comparison with measured data resulted in a RMSE in the order of 0.10 m. The NLCD dataset for 2001 resulted in the lowest RMSE when compared to observations made during Hurricane Bret, which is in alignment with the nearly coincident times between the hurricane landfall (1999) and the dataset coverage (2001). This demonstrates the importance of having correct land cover representation for a given historical hurricane event for the case of accurate reconstruction of the historical surge. Although the NWI dataset has been updated from 1993 to 2011, it presented the second lowest RMSE. We attribute its lower RMSE to the higher accuracy of wetlands and coastal vegetation mapping.

The uncertainty in the surge response was quantified with an overall mean value of 0.11 m and a standard deviation of 0.12 m. We also found that the uncertainty is strongly correlated to the meteorological conditions. The higher uncertainties were found with the lowest central pressure storms, followed by the fast moving storms; Very low

uncertainties were associated with the slow moving and weak storms. Location also played an important role in the uncertainty range, with sub regions such as behind the barrier islands (with higher density of wetlands vegetation) having residuals as high as 1.00 m. Residuals greater than 0.50 m were also found in the Intercoastal Waterway, Corpus Christi Bay, Copano Bay and San Antonio Bay. The higher residuals were always on the right hand side of the storm, with residuals never greater than 0.20 m at locations distant over 100 km from the storm eye.

In this study, we demonstrate the impacts of land cover datasets selection on the surge response for coastal bays. We quantified the uncertainties expected for a set of meteorological conditions and locations. We concluded that on average, we can expect at least 0.1 m of uncertainties due to land cover, with values rising up to 1 m in selected location under certain storm conditions. These uncertainty ranges, among other sources of uncertainty (e.g., wind model, bathymetry, meteorology), can be used to provide guidance on estimating confidence intervals for hurricane storm surge design and planning. The uncertainty dependence on storm intensity is particularly important when considering the expected hurricane intensification with climate change and when considering storm probabilities or return periods.

Although the magnitude of our results is strongly related to our study location (i.e., land cover datasets variations, topography, meteorological conditions), we believe that the overall findings are transferable to other coastal bays. A careful analysis of different land

cover datasets prior to carrying out storm surge simulations might lead to a better understanding of the consequent uncertainty from dataset selection. This is especially important in areas without sufficient recorded historical data to model validation.

CHAPTER IV

EFFECTS OF SEA-LEVEL RISE ON HURRICANE STORM SURGE AND DAMAGE IN COASTAL BAYS

INTRODUCTION

Hurricanes are one of the most costly natural disasters impacting US coastal areas (Lott and Ross 2006). Recent studies point towards an increase in damages caused by hurricanes most likely because climate change, which combining sea-level rise (SLR), the predicted hurricane intensification due to a warmer climate (Knutson *et al.* 2010; Elsner *et al.* 2008), and increasing coastal populations (Emanuel 2005) could double the global financial losses from hurricanes by 2100 (Hallegatte 2012 and Mendelsohn *et al.* 2012). One of the most important factors of climate change that will impact coastal areas is the SLR, which in recent decades has a rate over 3 mm/year globally (Church *et al.* 2008). Thus, hurricane storm surge risk is expected to increase under climate change (Lin *et al.* 2012); therefore, it is critical to fully understand the effects of SLR on hurricane storm surge.

Many authors have investigated the vulnerability of hurricane prone coastal areas to the effects of SLR (Park *et al.* 2011; Frazier *et al.* 2010; Wu *et al.* 2002; Bjarnadottir *et al.* 2011), the future risks and impacts caused by SLR on storm surge inundation (Cooper *et al.* 2008 and Shepard *et al.* 2012), and the impact of SLR on extreme value statistics for peak surges during storm events (Warner and Tissot 2012; and Hunter 2010). The

current approach to incorporate the effects of SLR on hurricane flooding is to linearly add a given SLR amount to the results of hurricane storm surge simulations or present day statistics. However, Resio and Westerink (2008) demonstrate that the storm surge is also strongly dependent on water depth and shelf width, as well as forcing and dissipation mechanisms.

Although Lin *et al.* (2012) recognized the existence of non-linear effects of SLR on storm surge, they reported an insignificant effect of SLR on storm surge simulations for New York City. Smith *et al.* (2010) reported that the storm surges increased from 1 to 3 m in addition to SLR in wetland areas in southeast Louisiana. They also reported surge increases of double or triple the relative SLR over broad areas and as much as five times in others, warning of the risk of underestimating flood levels due to the non-linear nature of both surge generation and propagation and of wave breaking. Ratcliff and Smith (2011) reported significant storm surge variances due to the effects of SLR in numerical simulations for Chesapeake Bay, more specifically in marsh areas and locations protected by surrounding topography. Mousavi *et al.* (2011) found that although the effects of SLR on storm surge variance was negligible along the coast, they reported changes in the surge response inside coastal bays.

Besides geometrical changes in coastal bays (i.e., deeper water depth and larger surface area), SLR is also expected to have substantial impacts on the patterns and process of coastal wetlands (Michener *et al.* 1995); therefore, affecting surge generation and

propagation inside the bays. The impact of climate change and subsequent SLR on wetlands and coastal marshes has been investigated by Chu-Agor *et al.* (2011), Craft *et al.* (2009) and Galbraith *et al.* (2002). More specifically, Smith *et al.* (2010) investigated the impact of SLR on hurricane storm surges along the coast of Louisiana, incorporating the associated wetlands change.

The objective of this study is to quantify the effect of SLR on hurricane storm surge and damage in coastal bays. We are particularly interested in quantifying the impacts due to land cover changes caused by SLR on the mean maximum surge, its geospatial anomalies, inundation extent, and consequent buildings damage estimation, population and businesses affected.

METHODOLOGY

Study area

This study focuses on Texas central bays, including Matagorda Bay, Lavaca Bay, San Antonio Bay, Copano Bay, Corpus Christi Bay, Oso Bay and Baffin Bay (Figure 4.1). These bays are separated from the open coast by narrow barrier islands and are connected to the ocean by several tidal inlets. This region is home of the City of Corpus Christi with a population of approximately three hundred thousand people. It is the location of the Naval Air Station Corpus Christi and the 5th largest port in the nation, the Port of Corpus Christi, as well as the cities of Port Aransas, Rockport, Port Lavaca and

Aransas Pass. This area has faced a number of hurricanes (e.g., Hurricane Beulah in 1967, Hurricane Bret in 1999 and, most recently, Hurricane Alex in 2010).
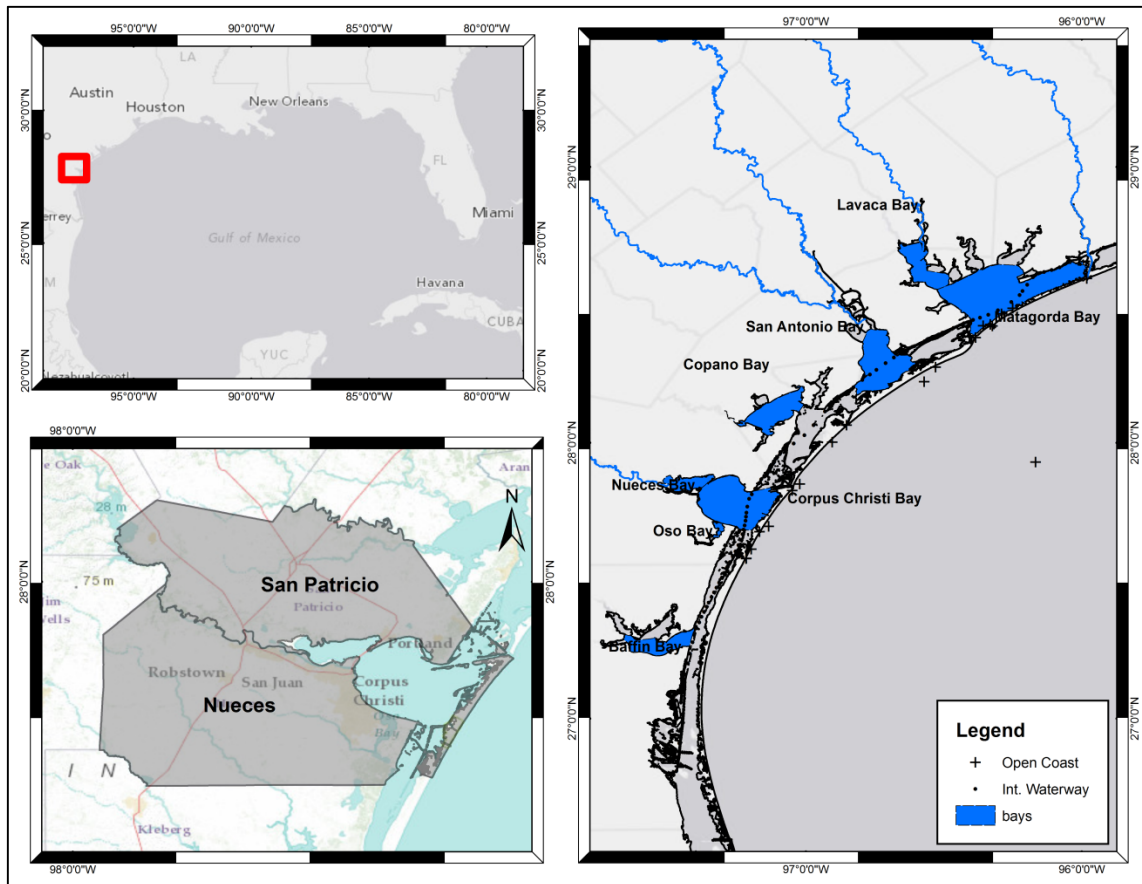
Figure 4.1: Location of the study within the Gulf of Mexico. Nueces and San Patricio county limits and the coastal bays of the Texas central coast.

We analyzed the impacts of SLR on the surge response due to changes in land cover caused by SLR, as well as the overall impact of SLR on the surge response in coastal bays. This analysis is based on storm surge simulation results at 686 recording points in various locations along the study area (Figures 4.1 and 4.2):
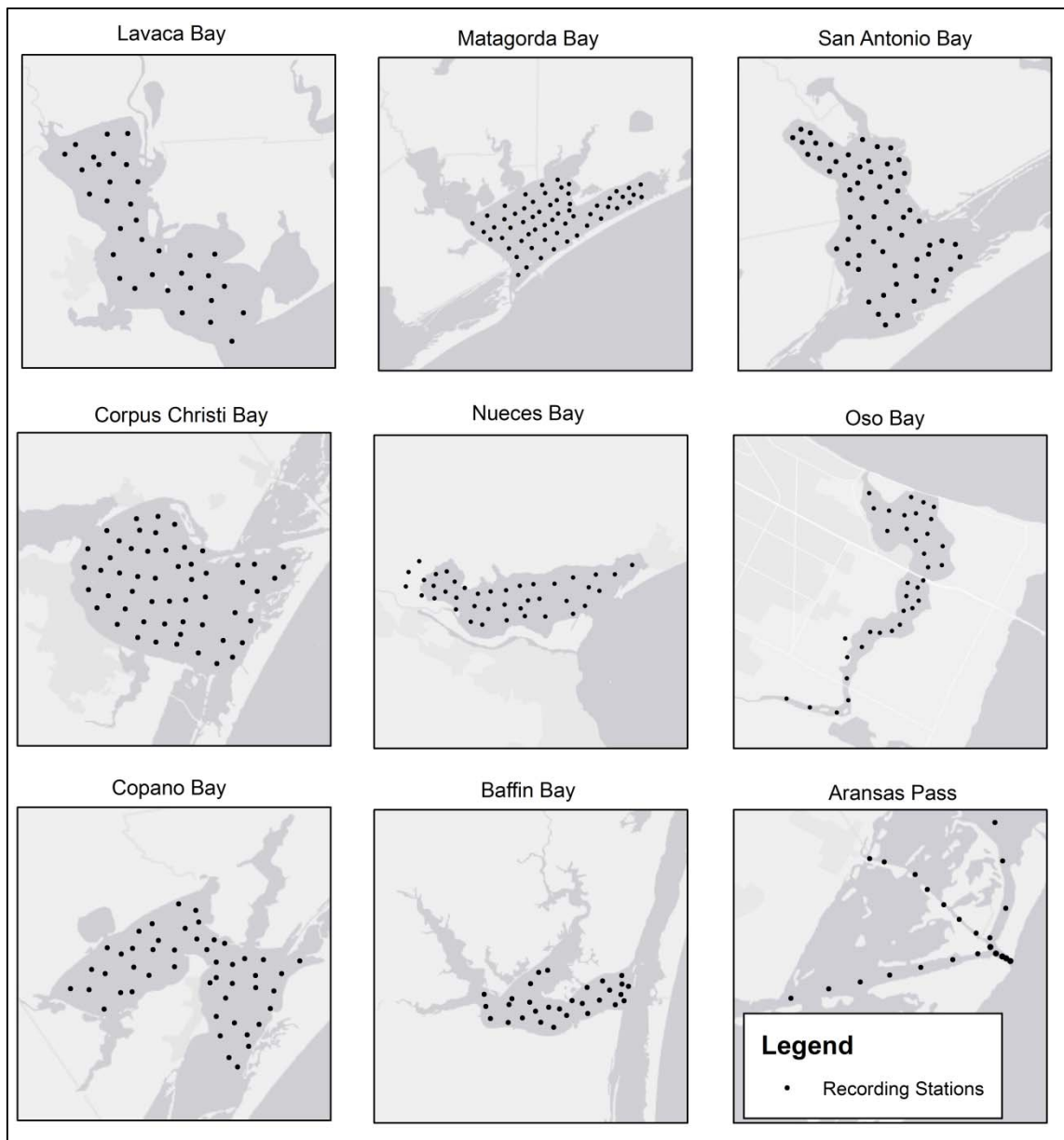
Figure 4.2: Placement of recording points within the coastal bays (b).

- the Intercoastal Waterway (90), Aransas Pass (28), Corpus Christi Bay (54), Nueces Bay (40), Oso Bay (36), immediately behind the barrier islands (102), the margins of Corpus Christi Bay (55), the margins of Nueces Bay (30), Matagorda

Bay (59), Copano Bay (48), Lavaca Bay (33), San Antonio Bay (60), Baffin Bay (29), and along the open coast (22). The stations immediately behind the barrier island and on the margins of the bays are not indicated in the Figures. They were placed equally spaced along its shorelines.

The damage analyses also included the Nueces and San Patricio Counties, both of which are located on the margins of Corpus Christi Bay and Nueces Bay. Nueces County has a population of approximately 340,000 (U.S. Census 2010) and is home to the City of Corpus Christi; San Patricio County has a population of approximately 64,000 people (U.S. Census 2010) and is home to the city of Port Aransas (Figure 4.1).

Numerical modeling

We applied the coupled version of the Advanced Circulation (ADCIRC) model and the wave model SWAN (Dietrich *et al.* 2011) to calculate hurricane storm surge. The ADCIRC model (Luettich and Westerink 2004) is a finite element, shallow water model that solves for water levels and currents at a range of scales and is widely used for storm surge modeling (*e.g.,* Irish *et al.* 2005; Westerink *et al.* 2008; Ebersole *et al.* 2010; Dietrich *et al.* 2010, Bunya *et al.* 2010, and Dietrich *et al.* 2011). SWAN is a third generation spectral wave model that computes random, short crested wind-generated waves, and waves transformation in the near shore and inland waters (Booij *et al.* 1999).

We used the two dimensional depth integrated version of ADCIRC that solves the vertically integrated mass balance equation (Eq. 4.1) and the momentum equations (Eq. 4.2):

$$\frac{\partial h}{\partial t} + \nabla_h \left(\vec{U} h \right) = 0 \tag{4.1}$$

$$\frac{\partial \vec{U}}{\partial t} + \left(U \bullet \nabla_h \right) \vec{U} = -g \nabla_h \left(\zeta + \frac{p(x,y)}{g\rho} \right) + f \hat{k} \times \vec{U} + \frac{\vec{\tau_s}}{h\rho} - \frac{\vec{\tau_b}}{h\rho} + \frac{\vec{\tau_w}}{h\rho} \tag{4.2}$$

where h is the water depth, t is the time, ζ is the surge elevation above mean sea-level (MSL), $\vec{U}$ is the depth-averaged horizontal velocity vector, p is the barometric pressure, f is the Coriolis force, $\hat{k}$ is a vertical unit vector, τ_s is the free-surface shear stress, τ_b is the bottom shear stress, τ_w is the wave radiation stress, and ρ is the water density. For wave modeling, SWAN uses the equation (Eq. 4.3):

$$\frac{\partial N}{\partial t} + \nabla_{\vec{x}} \left[\left(\vec{c_g} + \vec{C} \right) N \right] + \frac{\partial c_\theta N}{\partial \theta} + \frac{\partial c_\sigma N}{\partial \sigma} = \frac{S_{tot}}{\sigma} \tag{4.3}$$

where N is the wave action density spectrum, C_g is the wave group velocity, C_s is the propagation velocity, s is the relative frequency, θ is the wave direction, C_θ is the wave propagation velocity, S_{tot} is the wave growth caused by the wind, and C is the current velocity.

A more detailed discussion of the governing equations used in ADCIRC and SWAN can be found in Luettich and Westerink (2004) and Booij *et al.* (1999), respectively. The coupled version of ADCIRC and UNSWAN (Dietrich *et al.* 2011) uses the same unstructured finite element numerical grid for both models. The wave model is forced by wind, and the surge model is forced by wind and pressure fields.

We used a steady-state dynamical model, the TC96 developed by Thompson and Cardone (1996), to create the wind and pressure fields. The model computes wind stress, average wind speed and direction inside the Planetary Boundary Layer (PBL). The model assumes that the tropical cyclone structure changes slowly; thus, it can be represented using snapshots (e.g., 6 hours intervals) of its meteorological conditions: hurricane central pressure, radius of maximum speeds, storm track, Holland B parameter, and storm forward speed. The wind and pressure fields were generated every 15 min and interpolated between each snapshot. The model is based on the equation of horizontal momentum, vertically averaged through the depth of the PBL (Thompson and Cardone 1996) (Eq. 4.4):

$$f \, \hat{k} \times \left(\vec{V} - \overline{V_g} \right) = -\frac{1}{\rho_{air}} \nabla C_p - \frac{C_D}{H} \left| \vec{V} - \overline{V_c} \right| \left(\vec{V} - \overline{V_c} \right) \qquad (4.4)$$

where $\overline{V_g}$ is the geostrophic velocity vector at the low center, $\vec{V}$ is the averaged horizontal velocity vector, ρ_{air} is the air density, C_p is the pressure representing the

tropical cyclone, $\vec{V_c}$ is the velocity vector of the moving reference system, C_D is the drag coefficient, and *H* is the depth of the PBL layer. A more detailed description of the TC96 model can be found at Thompson and Cardone (1996).

We developed a high resolution computational mesh for the study area based on a regional scale validated mesh (Dietrich *et al.* 2011), which incorporated the study area. Our mesh has 1.3 million nodes and 2.5 million elements with resolution up to thirty meters in the study area and two kilometers in the Atlantic Ocean. The areas surrounding the Texas central bays were defined by using the high resolution information from the validated mesh. The new mesh was validated in several locations with a R^2 of 0.96 when compared to the original mesh (Chapter 2). The tide was neglected due to its small amplitude in the study area (*e.g.,* 0.17 m at NOAA station Port Ingleside in Corpus Christi Bay), and the river inflows were also neglected to simplify the analyses.

We reviewed the historical hurricane record (NOAA 2012c) and identified Hurricanes Bret (1999), Beulah (1967), Allen (1980) and Carla (1961) as indicative of typical hurricane meteorological conditions for the study area. Based on these storms, we selected key meteorological hurricane parameters (central pressure, forward speed and radius to maximum wind). The TC96 steady-state dynamical model, developed by Thompson and Cardone (1996), was used to develop nine hypothetical storms based on historical parameters. The hypothetical storms represent three landfall locations (Figure 4.3), considering two maximum forward speeds (11.11 and 37.04 km/h), two maximum

lower central pressure (930 and 960 mb) and one hurricane radius to maximum winds (31.48 km) (Table 4.1). These values represent common mid-range hurricane conditions for the study area (Resio *et al*. 2007). The storm ID represents its track, forward speed and central pressure.

Table 4.1: Meteorological parameters used to create the hypothetical storms (b).

ID	Track	Radius to maximum wind (km)	Forward Speed (km/h)	Central Pressure(mb)
A-11-960	A	31.48	11.11	960
A-37-960	A	31.48	37.04	960
A-37-930	A	31.48	37.04	930
B-11-960	B	31.48	11.11	960
B-37-960	B	31.48	37.04	960
B-37-930	B	31.48	37.04	930
C-11-960	C	31.48	11.11	960
C-37-960	C	31.48	37.04	960
C-37-930	C	31.48	37.04	930

Figure 4.3: Hurricane tracks in the Gulf of Mexico and Landfall locations.

Sea-level Rise scenarios

Church *et al.* (2008) demonstrated an increase in the rate of SLR based on gage data and remote sensing over the last century. Current research arguably points towards an increased rate of SLR projected for this century (e.g., Nichols and Cazenave 2010). The U.S. Army Corps of Engineers (USACE) recommends the consideration of SLR into civil works programs (USACE 2011). They estimated an upper bound of 2 m as a maximum expected SLR for 2100, based on several peer-reviewed publications (Jevrejeva 2010 [0.60~1.80 m]; Vermeer 2009 [0.75~1.90 m]; Pfeffer 2008 [0.80~2.00 m]; Horton *et al.* 2008 [0.55~0.85 m]; Rahmstorf 2007 [0.50~1.40 m]; International Panel on Climate Change 2007 [0.20~0.60]; National Research Council 1987 [0.50~1.50 m]).

More specific to our study area, the observed SLR rate based on the record from 1948 to 2006 at the Rockport, TX, National Oceanic and Atmosphere Administration (NOAA) station is 5.16 (+/- 0.67) mm/year (NOAA 2012d). Subsidence rates in the region are estimated to be approximately 2.9 mm/year (Frey *et al.* 2010). Based on the current rates, from 2006 to 2100, we could expect a SLR of 0.48 m in the study area. To cover the full range of possible SLR scenarios, we concentrated our analyses on equally spaced intervals of 0.50 m, considering four scenarios: 0.50, 1.00, 1.50 and 2.00 m. The effects of SLR on the raising mean sea level (MSL) are taken into account within the computational models by increasing the base water level above the current MSL (2000s)

for the entire model domain as an initial condition for the simulation. The effects of SLR on land cover are discussed below.

Wetland degradation

Wetlands and other coastal vegetation are represented in the numerical models through their influence on the forcing and dissipation mechanisms of hurricane storm surge. Its interference on the momentum transmitted to the water column by winds and the frictional drag at the sea bottom are taken into account in the computational models. The frictional resistance at the sea bottom is accounted for by using a non-linear bottom drag coefficient related to land cover surface roughness (Eq. 4.5):

$$\vec{\tau_b} = \frac{C_f \vec{U} |\vec{U}|}{h} \tag{4.5}$$

where C_f is dimensionless friction coefficient. We adopted the following non-linear quadratic formulation for calculating the friction coefficient (Eq. 4.6)

$$C_f = g * \frac{n^2}{h^{(1/3)}} \tag{4.6}$$

where g is the gravitational constant; and n is the Manning's n roughness coefficient. The friction coefficient is incorporated into the bottom shear stress formulation by (Eq. 4.5):

The influence of coastal vegetation on the wind stress and consequent effects on the momentum transfer to the water column is accounted for in two ways: 1) a directional wind reduction coefficient due to the frictional drag caused by the land cover surface; and 2) a complete blocking effect of momentum transfer in areas with dense canopy.

To characterize wetland types and define their spatial distribution along the coast, we used the National Wetlands Inventory (NWI) (U.S. Fish and Wildlife Service, 2012). The NWI was developed by the U.S. Fish and Wildlife Service from 1977 to the present, and is available at a 1:24.000 scale. The mapping is mostly performed by photo-interpretation and field work (Wilen and Tiner, 1989) and a dataset dated from 1993 are available for the study area. The land cover classification follows the Cowardin *et al.* (1979) system, which is hierarchical with five major groups, subsystems, classes and sub-classes. We used the raster format of the dataset with a resolution of approximately 30 m.

The creation of the current geospatial parameters is based on the methods published by Atkinson *et al.* (2011); Leuttich and Westerink (2004); Tsihrintz and Madiedo (2000); Dietrich *et al.* (2011); Wamsley *et al.* (2010); and Bunia *et al.* (2010). These methods are based on a relationship between the land cover types and the Manning's *n* parameter, wind blocking capacity and the directional wind reduction coefficient(land roughness length z_o) defined in the Federal Emergency Management Agency (FEMA) HAZUS

software program (Federal Emergency Management Agency 2012). A detailed description of these methods is provided in Chapter 3.

The effects of SLR on coastal vegetation are extremely complex and still a subject of active research (*e.g.,* Alongi 2007). For this study, we applied the criteria proposed by Smith *et al.* (2010) to relate the effects of SLR on coastal vegetation (drowning and upstream migration) by specifically determining changes to the frictional drag at the sea bottom and wind reduction for a given SLR scenario. The static water depths under SLR scenarios are spatially calculated using the National Elevation Dataset (NED) (USGS 2012) with a resolution of 30 m. We first calculate a constant water surface for the Mean High Water (MHW) and Mean Low Water (MLW) for each SLR scenario by adding/subtracting the assumed tidal amplitude (10 cm) (NOAA 2012d). A new geospatial parameter file is produced by comparing the land elevation to the MHW and MLW at each cell for a given SLR scenario, based on the following criteria (Smith *et al.* 2010):

- Elevation greater than MHW: The Manning's *n* and wind reduction parameters are kept as they were.

- Elevation lower than MLW: If Manning's *n* is currently greater than 0.1, it is divided by two; if it is lower than 0.1, it is set to 0.02 (open water) and the wind blocking effect is turned off.

- Elevation between MLW and MHW: If Manning's *n* is greater than 0.1, it is divided by two; if it is lower than 0.1, it is set to 0.035 (saline marsh) and the wind blocking effect is turned off.

For this study, the effects of sedimentation and erosion due to SLR were not included in order to simplify the analyses.

Impacts of sea-level rise on topography

Morphological responses of barrier islands to SLR are extremely complex and strongly related to the rate and acceleration of SLR (Titus 1990). Irish *et al.* (2010) discussed that, although the barrier islands in Corpus Christi Bay were able to form due to a slow SLR rate for the past 3000 to 7000 years, their future morphological response to SLR would greatly vary according to the SLR rate (e.g., SLR exceeding 0.1-0.2 m/year would cause them to break up and drown). On the other hand, with slow rates of SLR, the barrier island could became stable or migrate landward. Therefore it is extremely difficult to predict the exact response of the barrier island to SLR.

To simplify the analyses, here, we considered a constant topography/bathymetry and do not include any morphological changes to the coastal morphology due to SLR. However, the shoreline is changing with SLR (Figure 4.4) as the sea-level is rising (bathtub approach).
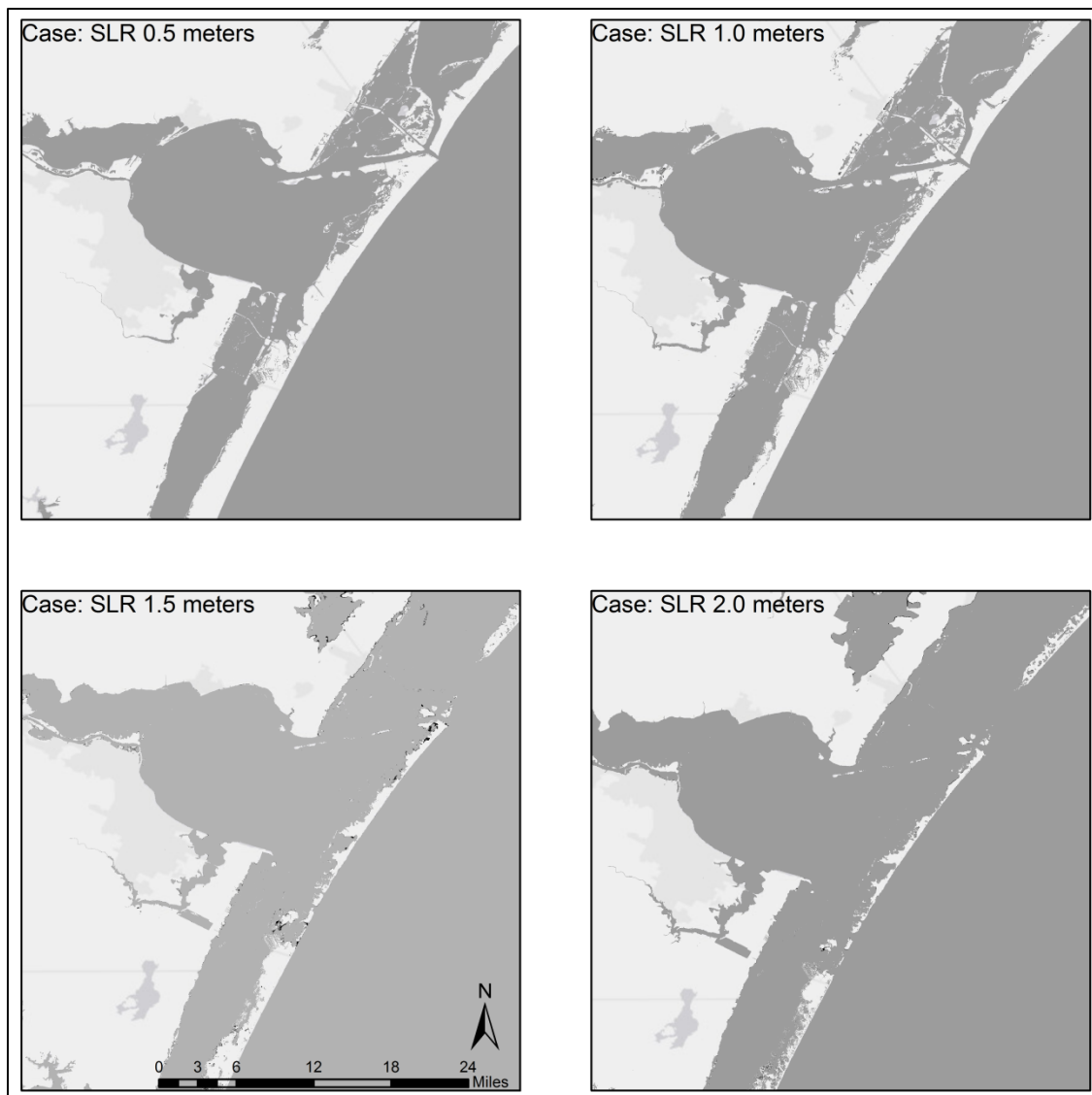
Figure 4.4: Simulated shoreline evolution due to SLR using a *'bathtub'* type model showing the barrier island breaching and submergence with SLR greater than 1.0 m.

In this simplified approach, an SLR of up to 1.0 m would not greatly affect the barrier island as it is today; however, SLRs greater than 1.0 m would significantly impact the shoreline and the barrier island. The barrier island would breach in several locations with

1.5 m of SLR and would almost be completely submerged for 2.0 m. We expect these effects to have a significant impact on the surge in the bays as the open coast surge can freely propagate inside.

Surge anomaly

Here, we define the surge as the increment of the water level above MSL caused by meteorological effects only, as described by (Eq. 4.7):

$$\zeta = h - MSL$$

(4.7)

where ζ the surge and *MSL* is the mean sea-level at the time of interest as defined by (Eq. 4.8).

$$MSL = MSL_{currentday} + \Phi_{SLR}$$

(4.8)

where $MSL_{currentday}$ is the reference MSL in 2000 and $\Delta\Phi_{SLR}$ is the SLR increment (Figure 4.5).
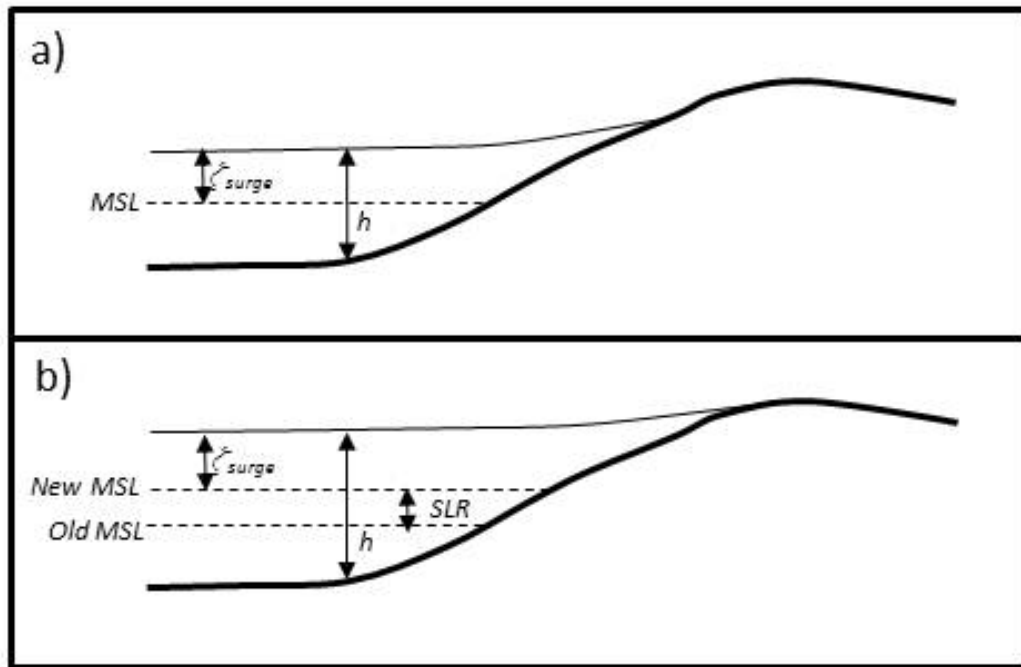
Figure 4.5: a) The total depth h is the final flood elevation; the surge is the difference between the h and the *MSL*. b) Surge under a SLR condition.

The impacts of SLR on the surge response for coastal bays are mostly related to alterations in the surge forcing and dissipation mechanisms, and to the bay's geometry. The forcing mechanisms are affected by the SLR due to changes in the wind stress and consequent reduction in the momentum transfer to the water column. The dissipation mechanisms are also greatly affected by changes in the frictional drag at the sea bottom. The changes in the land cover due to vegetation drowning or migration might significantly affect the frictional drag resistance to the wind, the shielding effect that the vegetation canopy might have, and reduce the frictional drag at the sea bottom. We expect these changes to increase surges, especially in faster storms (Chapter III). The geometric changes are mostly related to a water depth changes (MSL increase with SLR)

over the entire domain and an increase in the total water surface area, increasing the wind fetch. Theoretically, we expect surge to decrease with increasing water depth and expect surge to increase with increasing wind fetch (Resio and Westerink 2008) (Eq. 4.9). Thus, competing processes influence local surge generation in coastal bays as SLR.

$$\zeta \propto \left(\frac{\tau_s}{gh} \right) W_{fetch} \tag{4.9}$$

where W_{fetch} is the wind fetch. In figure 4.6, we present a schematic of the expected changes from SLR on the surge forcing and dissipation mechanisms, and the bay geometry.

The surge anomaly is calculated as follows (Eq. 4.10):

$$\lambda = \left(\zeta_{SLR} - \Delta\Phi_{SLR} \right) - \zeta_{MSL} \tag{4.10}$$

where λ is the surge anomaly, ζ_{SLR} is the surge calculated under SLR, and ζ_{MSL} is the surge calculated at $MSL_{currentday}$.
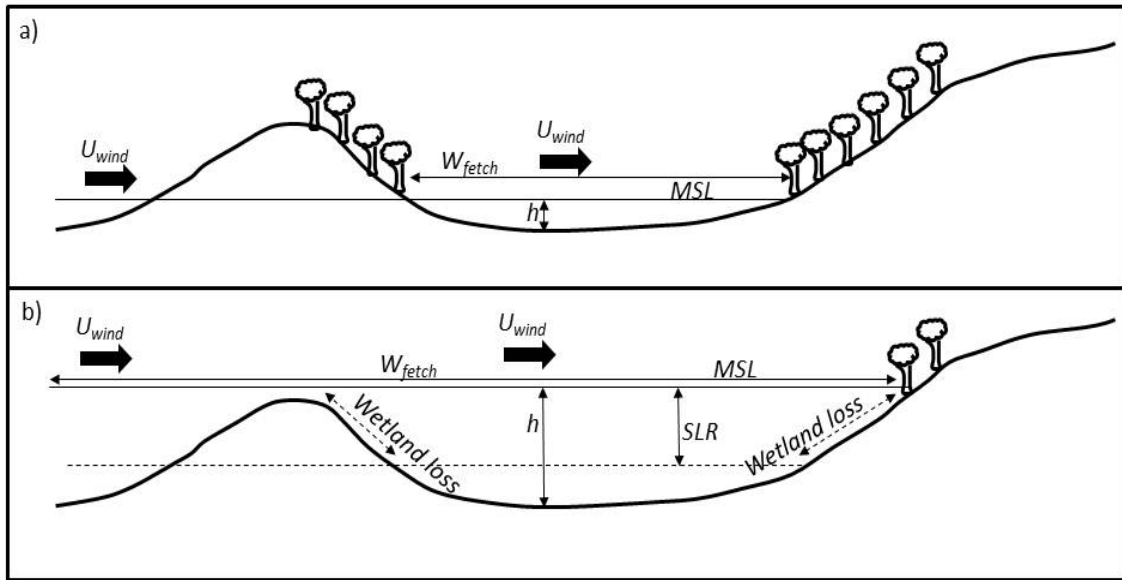
Figure 4.6: Schematic of the impact of SLR on hurricane storm surge forcing and dissipation mechanisms for coastal bays. a) Current MSL where the barrier island and coastal vegetation are above MSL. b) Hypothetical SLR scenario where the barrier island is submerged and the coastal vegetation was impacted by SLR. Note the changes in depth (h), the length of the fetch area for the wind (W_{fetch}) and the areas of wetland losses.

Damage, population and businesses affected

The most common method for evaluating damage from flooding is by using depth-damage functions. These functions relate flood depths to percent damage for a given structure and are derived from post-event surveys, analyses of insurance claims, and historical flood data analyses (Nadal *et al.* 2010). An application for damage estimation in the U.S. is the Hazards US Multi Hazard (HAZUS-MH), developed by the Federal Emergency Management Agency (FEMA) in 2004 (Schneider *et al.* 2006). Several applications of the above mentioned methods can be found in the literature (Schiller 2011; Jonkman *et al.* 2008; Frey *et al.* 2010; Brody *et al.* 2007; Elmer *et al.* 2010).

Here, we quantified the impacts, of SLR and related wetland loss, on hurricane surge physical damages to buildings, population and businesses. The impacts are spatially estimated by a relationship between the depth of flooding and an inventory geodatabase. The damage evaluation was carried out programmatically using PYTHON, FORTRAN and ArcPY in a GIS framework, built upon the basic functionality of HAZUS.

The hydrodynamic modeling of storm surge gives water levels for every node in the numerical mesh. The maximum surge level was extracted from the model results and converted to rasters using GIS. The water depths were calculated based on the National Elevation Dataset (USGS 2012) with a resolution of 10 m. The surges with respect to MSL from ADCIRC+SWAN were converted to the NAVD88 vertical datum and used with this reference from here on. For each storm meteorological condition and SLR scenario, a water depth raster was generated with a resolution of 10 m. According to Frey *et al.* (2010), the usual first floor elevation in the Corpus Christi area is 1 feet, thus we assumed the overall first floor elevation for both counties to be 1foot.

The population inventory is extracted from the US Census block data (US Census Bureau 2000). The representation of population by census block units inherits uncertainties to where the population is actually located. Although analyses of population at risk to storm surge distributed at a parcel level (e.g., Shepard *et al.* 2012 and Frey *et al.* 2010) have been carried out, here, we evaluated the relative impact, thus spatial uncertainties are similar for all scenarios considered. The population is

considered affected if for any given block the water depth is above the assumed first floor elevation (0.3 m).

We adopted the U.S. Businesses database from Reference USA (Infogroup 2012) as this study's business data source. This database provides data on economic activities within the counties, with the approximate location of each business, its revenue and other economic information. A total of 2,304 businesses from San Patricio county and 14,226 business from Nueces County were included in the analyses. We used the latitude and longitude from each business available in the database to create a point feature class within the geodatabase, assigning an estimated spatial location for each business.

The business damage was based on a classification scheme that represented the severity of the flooding based on the flood depth at the business point location (Frey et al. 2010). This classification is used to infer the total number of businesses affected between ranges of flood depths: 1) Nuisance flooding [depths below foundation]; 2) Minor flooding [depths between 0.0 and 0.9 m]; 3) Major flooding [depths between 0.9 and 1.5 m]; and 4) Catastrophic flooding [depths greater than 1.5 m]. Table 4.2 presents the relation between water levels and the flood index.

Table 4.2: Classification scheme for business flooding

Water Depth (m)	Definition
Below Foundation	Nuisance Flooding
0 ~ 0.9	Minor Flooding
0.9 ~ 1.5	Major Flooding
Greater than 1.5	Catastrophic Flooding

The built-environment inventory was taken from the HAZUS-MH (FEMA 2012) geodatabase. We adopted the census block unit for the physical direct damage analysis. Here, we considered the following occupancy classes: single family, manufactured housing, duplex, triplex, multi-dwellings (from 5-9, 10-19, 20-49, and 50+ units), temporary lodging, institutional dormitory, nursing home. A detailed description of each occupancy class is provided by FEMA (2012).

The physical direct damage analysis is based on the relationship between flood depth throughout the block and depth damage functions to compute damage to the building structures (Scawthorn *et al.* 2006). The damage curves were selected from the Federal Insurance Administration (FIA) fragility weighted curves and also from the U.S. Army Corps of Engineers (USACE) available with HAZUS (FEMA 2012). Within each building occupancy class, a depth-damage function is adopted according to the building type. The single family occupancy is divided into four groups: one floor (72%), two floors (23%), three or more floors (3%) and a split level (2%). These groups are further

classified in those with a basement (95%) and those without a basement (5%). The multifamily occupancy is divided in two groups: those with a sub-grade (5%) and those with a grade (95%). The other occupancy classes have a unique depth-damage function. In total, we adopted 22 depth-damage functions for this study. With these functions, we calculated the percentage of expected damage per occupancy class in each block.

We adopted the HAZUS (FEMA 2012) full replacement cost models published in Means Square Foot Costs (R. S. Means Company 2006), thus for each occupancy class, a full replacement cost is defined in terms of a cost per square foot. The estimated square-footage is aggregated by block units for each occupancy type. A detailed description of the replacement cost models for every occupancy class is presented in FEMA (2012).

The expected damage is calculated for each building occupancy class, from the estimated percentage of damage to the building, the estimated square footage area within the block and the estimated cost of replacement per square foot. The final value is aggregated by block.

RESULTS AND DISCUSSION

We performed an Analysis of Variance (ANOVA) test to verify the existence of a significant effect of SLR on the mean surge at each study location. The null hypothesis is that the mean surge does not change for the same meteorological conditions after removing the eustatic SLR. The hypothesis is rejected if at least one mean is different

$$H_o: \boldsymbol{\mu}_{present} = \boldsymbol{\mu}_{slr0.5} = \boldsymbol{\mu}_{slr1.0} = \boldsymbol{\mu}_{slr1.5} = \boldsymbol{\mu}_{slr2.0}$$

H_1: *At least one mean is different* ; ***Reject if:*** *p-value* < 0.05 [95%]).

The null hypothesis was rejected for every study location with a confidence of 95% for at least one meteorological condition, leading to the conclusion that the SLR significantly impacts the mean maximum surge inside the bays (Table 4.3).

Table 4.3: Results of the Analyses of Variance (ANOVA) tests (p-values) for the study area considering the 9 hypothetical storms. ($\boldsymbol{H_0}$: $\mu_{present} = \mu_{SLR0.5} = \mu_{slr1.0} = \mu_{slr1.5} = \mu_{slr2.0}$; $\boldsymbol{H_1}$: *At least one mean is different*; **Reject if:** p < 0.05) (p-values)

Storm / Location	A-11-960	A-37-960	A-37-930	B-11-960	B-37-960	B-37-930	C-11-960	C-37-960	C-37-930
Intercoastal Waterway	0.000	0.000	0.000	0.000	0.000	0.000	0.000	0.000	0.000
Aransas Pass	0.000	0.711	0.608	0.000	0.650	0.654	0.000	0.398	0.587
Corpus Christi Bay	0.000	0.000	0.000	0.000	0.000	0.000	0.000	0.000	0.000
Nueces Bay	0.000	0.000	0.000	0.000	0.000	0.000	0.000	0.000	0.000
Oso bay	0.000	0.544	0.454	0.313	0.001	0.177	0.233	0.000	0.283
Barrier Island	0.000	0.000	0.000	0.000	0.000	0.000	0.000	0.000	0.000
Margins	0.000	0.000	0.000	0.000	0.000	0.000	0.440	0.000	0.000
Nueces Bay Margins	0.000	0.000	0.000	0.000	0.000	0.000	0.070	0.000	0.000
Matagorda Bay	0.000	0.000	0.000	0.000	0.000	0.000	0.000	0.000	0.000
Copano Bay	0.000	0.000	0.000	0.000	0.000	0.000	0.000	0.000	0.000
Open coast	0.999	0.998	0.999	1.000	0.998	0.998	1.000	1.000	1.000
Lavaca Bay	0.032	0.000	0.000	0.004	0.000	0.000	0.000	0.000	0.000
San Antonio Bay	0.000	0.000	0.000	0.000	0.000	0.000	0.000	0.000	0.000
Baffin Bay	0.000	0.001	0.001	0.000	0.000	0.000	0.000	0.000	0.000

The null hypothesis could not be rejected on the open coast stations, which demonstrates the small significance of the impacts of SLR on storm surge on open coasts, in alignment with the findings of Mousavi *et al.* (2011) for the same study region and Lin (2012) for New York.

Effects of sea-level rise on Manning's n and wind reduction parameters

For SLR values of 0.5, 1.0, 1.5 and 2.0 m, the inundated areas were 700, 1000, 2500 and 3000 km^2 respectively. Although the 1.0 m SLR scenario did not significantly affect the mean Manning's *n*, higher SLR amounts did significantly impact the mean Manning's *n*. In fact, the permanent inundation of coastal vegetation in the study area resulted in a mean Manning's *n* reduction from 0.055 at present day to 0.040 for 2.0 m of SLR. The areas that currently provided wind shield were also affected by SLRs greater than 1.0 m, and were reduced by up to 150 km^2 for 2.0 m of SLR (Figure 4.7).

The geospatial representation of the changes in Manning's *n* due to SLR is presented in Figure 4.8. For 0.5 m of SLR, the changes are mostly less than 0.03 (Manning's *n*) and concentrated in the wetland areas behind the barrier islands, the margins of Baffin Bay and around Aransas Pass. For 1.0 m of SLR, the effects are also felt in the margins of all the bays within the study area and in some estuaries. For 1.5 m of SLR, the Manning's *n* changed over 0.05 in several locations and the effects of SLR are felt through the entire system, including upstream areas along rivers and estuaries. The barrier island is almost permanently inundated, and changes in the Manning's *n* can be seen all along the

islands. For 2.0 m of SLR, the changes in Manning's *n* are over 0.05 in almost all the

marginal areas, and the barrier island is submerged in several locations.
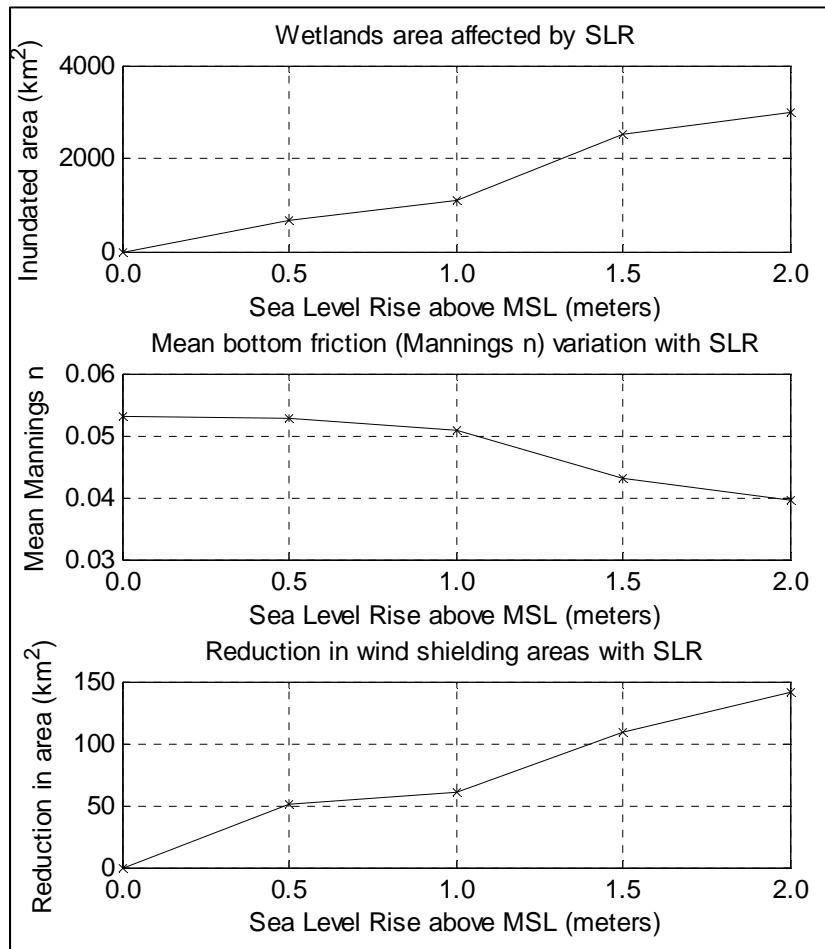
Figure 4.7: a) Flooded area extent by eustatic SLR affecting wetlands and other coastal vegetation. b) Mean Manning's *n* variation due to SLR in the study area. c) Reduction in wind shielding by dense vegetation quantified in aerial extent as a result of SLR.
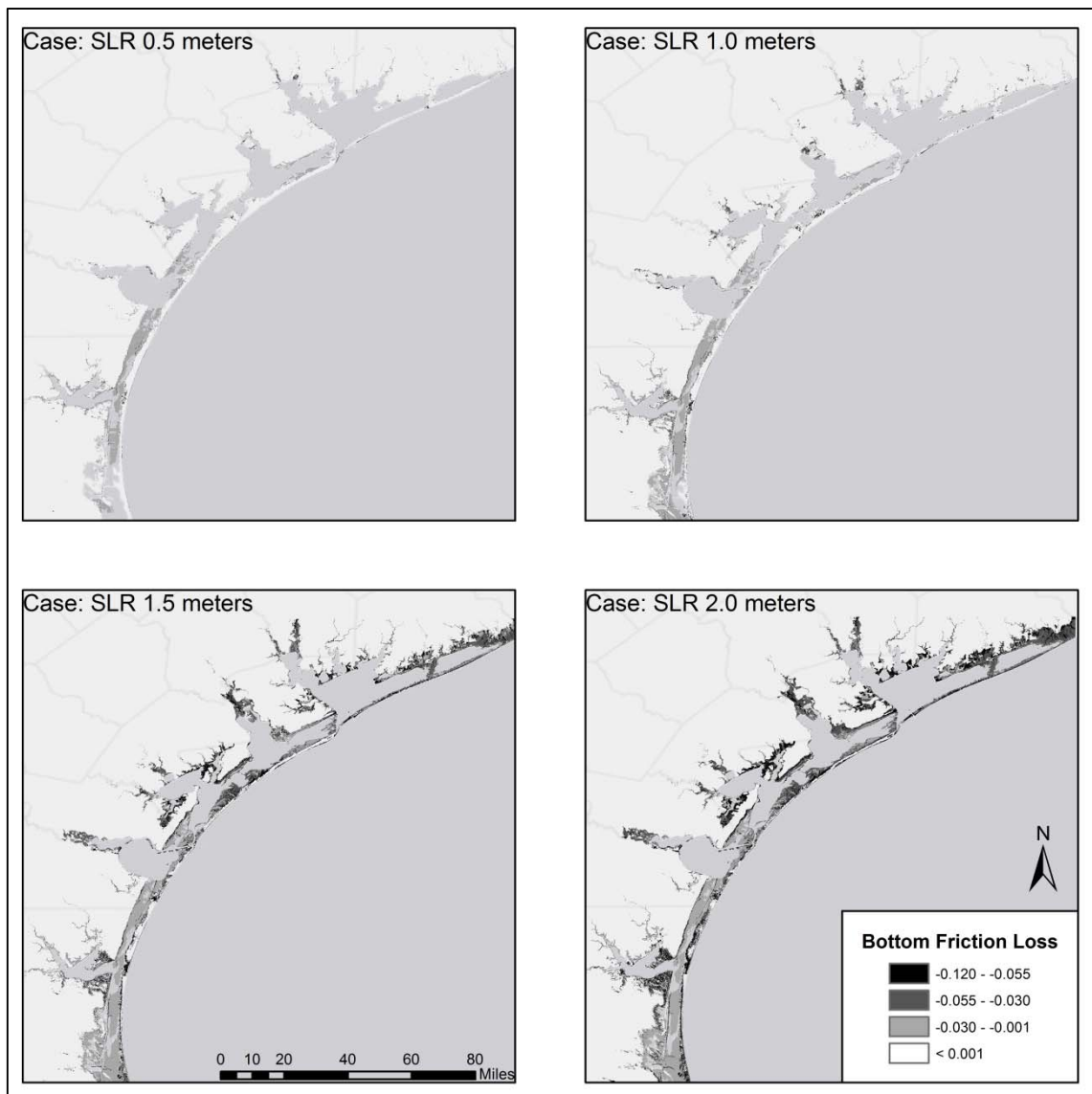
Figure 4.8: Geospatial impacts of SLR on frictional drag at sea bottom quantified by reduction in the Manning's *n* values: a) 0.5 m of SLR; b) 1.0 m of SLR; c) 1.5 m of SLR; and d) 2.0 m of SLR.

Effects of sea-level rise on surge when land cover changes are neglected

Neglecting the effects of land cover, the mean surge anomaly for all recording points for all storm conditions increased almost linearly with SLR (Figure 4.9). For 0.5 m of SLR

the overall mean surge anomaly was almost 0.10 m, for 1.0 m of SLR the overall mean

surge anomaly was almost 0.20 m, reaching up to 0.50 m for 2.0 m of SLR. The higher

mean surge anomaly was almost 0.90 m for the stronger storm (B-37-930) with 2.0 m of

SLR. The effects from SLR considered here led to an average surge increase of around

25% on top of the SLR.
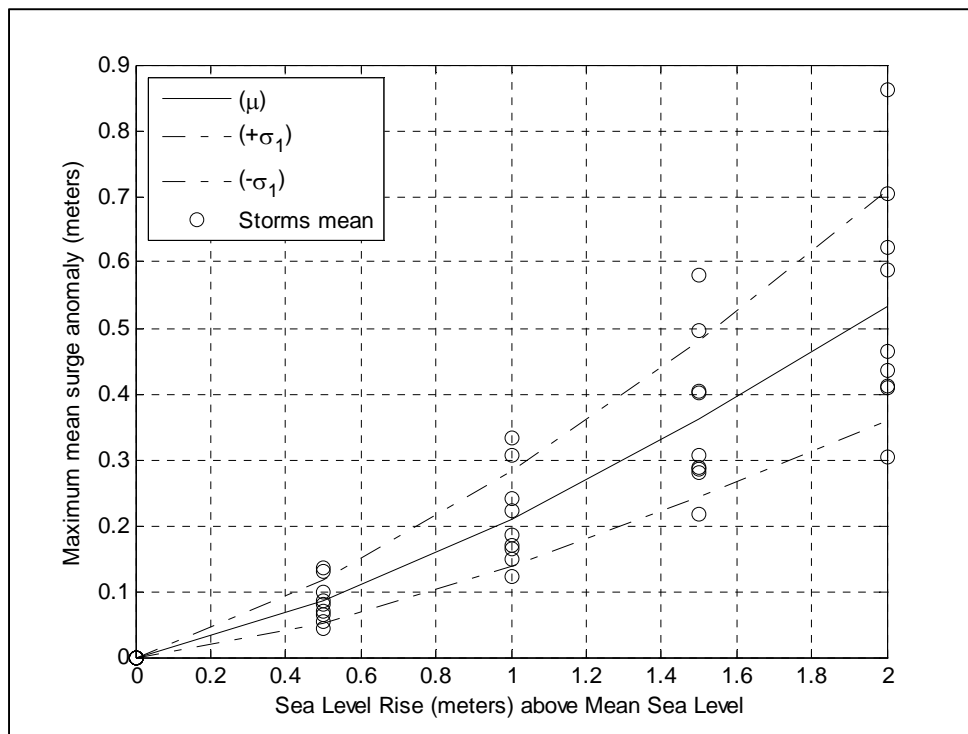
Figure 4.9: Impacts of SLR on the mean maximum surge anomaly neglecting land cover changes. Where μ is the mean surge for each storm condition and σ_1 is the standard deviation.

Here the mean maximum surge increased almost linearly with respect to SLR with an R^2

of 0.98 following the equation (Eq. 4.11):

$$\zeta_{mmsa} = 0.2698 * \Delta\Phi_{SLR} - 0.0308 \qquad\qquad (4.11)$$

where ζ_{mmsa} is the mean maximum surge neglecting land cover changes. The type of storm condition also significantly impacted the surge increase from SLR. The most intense and faster storm (i.e., *Vf:* 37.04 km/h; *Cp:* 930 mb) generated surge increases of up to almost 1.00 m on average. The weaker, but faster storm (i.e., *Vf:* 37.04 km/h; *Cp:* 960 mb) also resulted in above average surge increases for two tracks (B and C). The surge generated by the weaker and slower storms (*Vf:* 11.11 km/h; *Cp*: 960 mb) were less sensitive to SLR and resulted in surge increases of less than 0.4 m for the highest SLR scenario considered. These results were expected as the SLR is mainly impacting the forcing mechanism directly related to wind speed and dissipation mechanism related to water velocity.

Within the bays, Oso Bay presented the greater rate of increase on the mean maximum surge, with values up to 0.30 and 0.80 m for SLRs of 1.0 and 2.0 m, respectively. The influence of overtopping of the barrier islands was a significant contribution to surge in Corpus Christi, Nueces and Copano bays, where there was a variation on the mean maximum surge increase rate along the SLR intervals. On average, the mean maximum surge increase rate was also approximate 25% inside the bays (Eq. 4.11).

Effects of sea-level rise on surge when land cover changes are considered

Here, we analyze the effects of SLR on surge when land cover changes are considered in addition to the previously calculated effects of geometry changes. Following the small rates of change of Manning's *n* and wind blockage by vegetation for SLR scenarios of 1.0 m or less, the mean maximum surge increased no more than 0.05 m for all storm simulations This could be considered negligible given the model uncertainties. The most significant increase in the mean maximum surge is for SLR rise between 1.0 to 1.5 m, resulting in surge increases from 0.10 to 0.27 m. In this interval, we also identified a greater reduction in Manning's *n* and in wind shield areas. For SLR scenarios above 1.5 m the overall mean maximum surge increase is 0.20 m. When considering 2.0 m of SLR, although the mean maximum surge did not increase significantly, for some storm conditions, the mean maximum surge considering all locations were up to 0.35 m above the initial condition (Figure 4.10).

The mean maximum surge anomaly can be explained by the linear relationship presented Eq. 4.12, with a R^2 of 0.90:

$$\upsilon_{mmsa} = 0.1243 * \Delta\Phi_{SLR} - 0.01409 \tag{4.12}$$

where υ_{mmsa} is the mean maximum surge increment from land cover changes in meters. The mean maximum surge variation is also directly related to the storm properties. The larger mean maximum surge increase occurred for the strongest and fastest storms (i.e.,

Vf: 37.04 km/h; *Cp*: 930 mb) for the three tracks considered, followed by the weak and

fast storms (i.e., *Vf*: 37.04 km/h; *Cp*: 960 mb), leading to the conclusion that the storm

intensity played an important role in increasing the surge anomalies. We believe this is

directly related to the increased quantity of momentum transmitted to the water column

in the SLR conditions. For the weakest and slowest storm (i.e., *Vf*: 11.11 km/h; *Cp*: 960

mb), the mean maximum surge variation was always lower than 0.2 m (Figure 4.11).
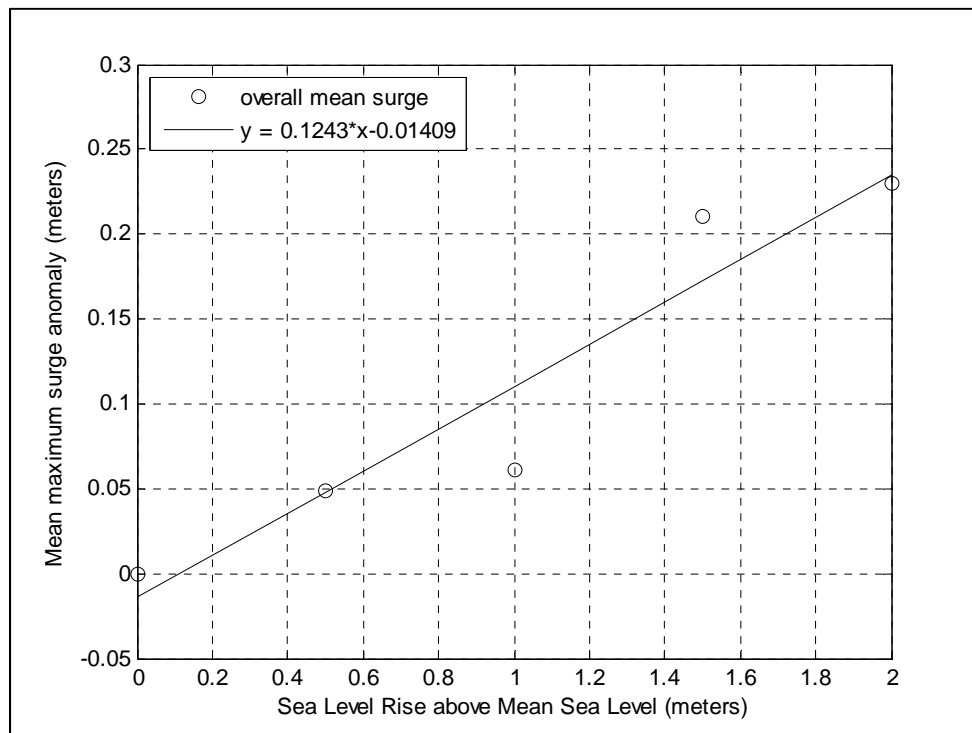
Figure 4.10: Linear model to represent the impact of land cover changes due to SLR on
the mean maximum surge anomaly.

In Figure 4.11, we can clearly observe the impact of SLR higher than 1.0 m on the surge anomaly. For every storm condition, the surge anomaly increased significantly for SLR above 1.0 m, following the land cover changes due to SLR trends showed in Figure 4.7.
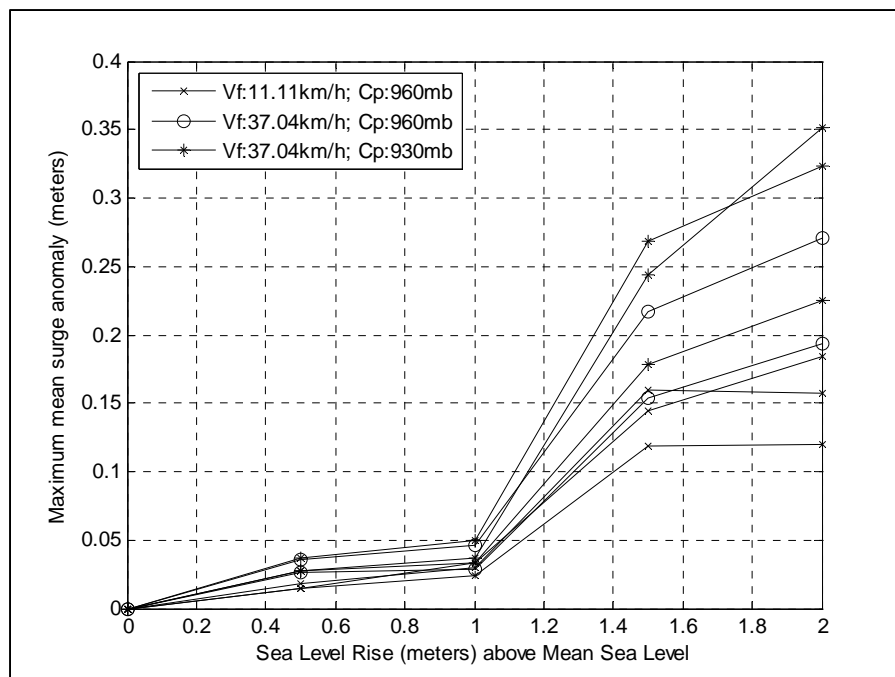
Figure 4.11: Impacts of land cover changes due to SLR quantified by the mean maximum surge anomaly for storm meteorological conditions. Each line represents a landfall location under given meteorological conditions.

We found a linear relationship between the mean Manning's *n* reduction due to SLR (Figure 4.12) and the mean maximum surge increase due to land cover changes only. Here, we provide an equation (Eq. 4.13) describing this relationship with an R^2 of 0.96 and RMSE of 0.02:

$$\mu_{mmsa} = -16.76 * \eta + 0.914 \tag{4.13}$$

where μ_{mmsa} is the mean maximum surge anomaly in m and η is the mean Manning's n

value for the study area.
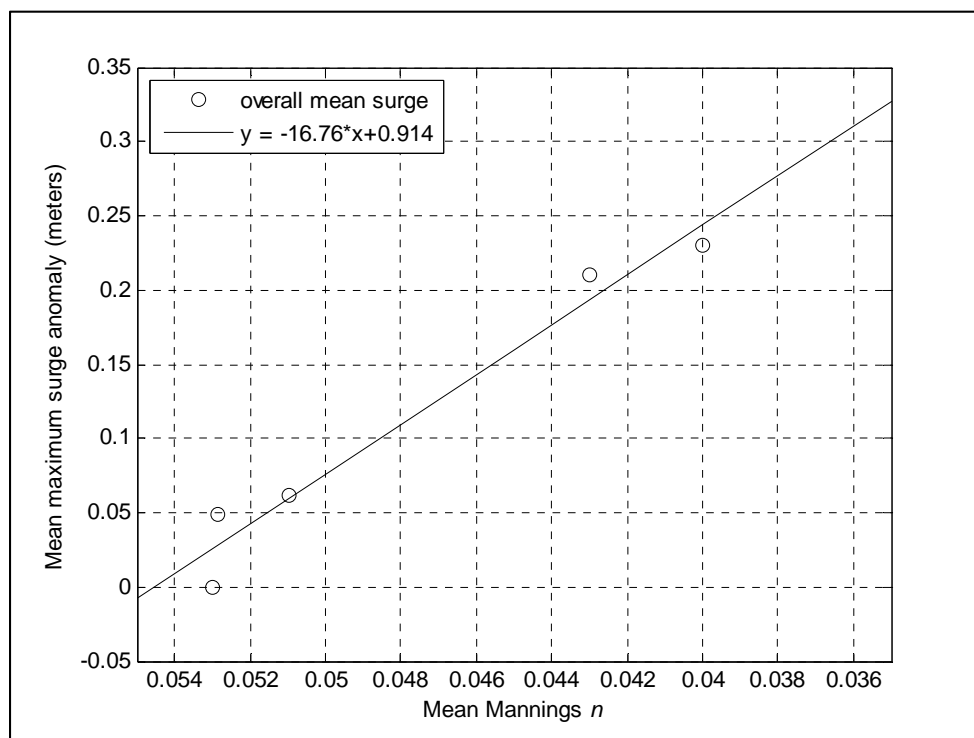
Figure 4.12: Linear model representing the relationship of Manning's *n* change due to SLR and the mean maximum surge anomaly.

Effects of sea-level rise on surge

The combined effects of SLR on surge considering geometry and land cover changes are

presented here. The overall impacts of SLR on surge are highly dependent on storm

conditions and specific locations within the study area. Figure 4.13 shows the mean

surge anomaly for each recording location in the study area, considering the four SLR
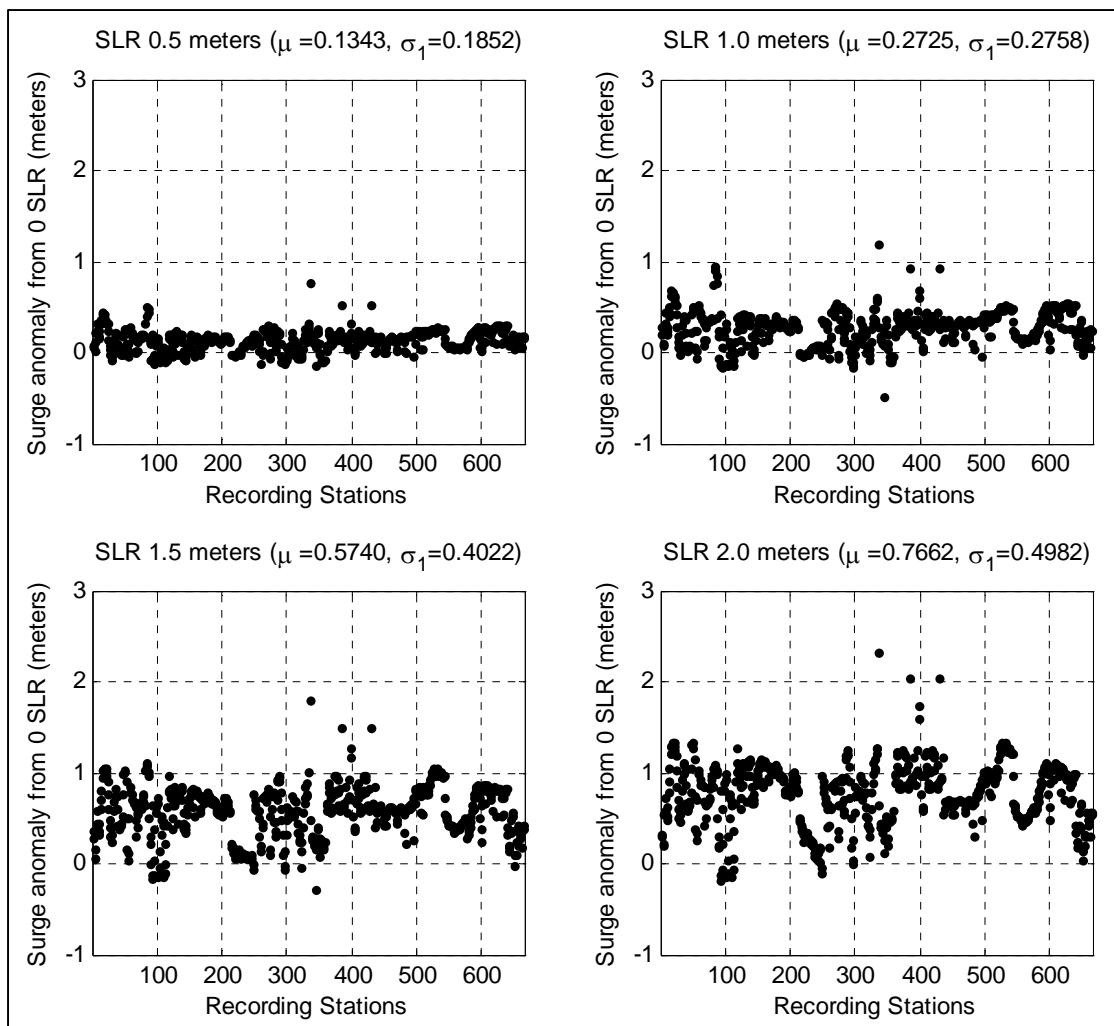
scenarios.

Figure 4.13: Maximum surge anomalies (departure from current MSL storm surge) for 688 locations due to SLR: a) 0.5 m of SLR; b) 1.0 m of SLR; c) 1.5 m of SLR; and d) 2.0 m of SLR.

The mean surge anomaly is positive and increases with SLR. The SLR scenario of 0.5 m caused a mean surge anomaly of 0.13 m, 1.0 m of SLR lead to a mean surge anomaly of 0.27 m, 1.5 m of SLR occasioned a mean surge anomaly of 0.57 m and the SLR scenario of 2 m resulted in a mean surge anomaly of 0.76 m. The standard deviation also increases for each SLR scenario from 0.18 m at 0.5 SLR to 0.49 m at 2.0 meters of SLR (Figure 4.14).
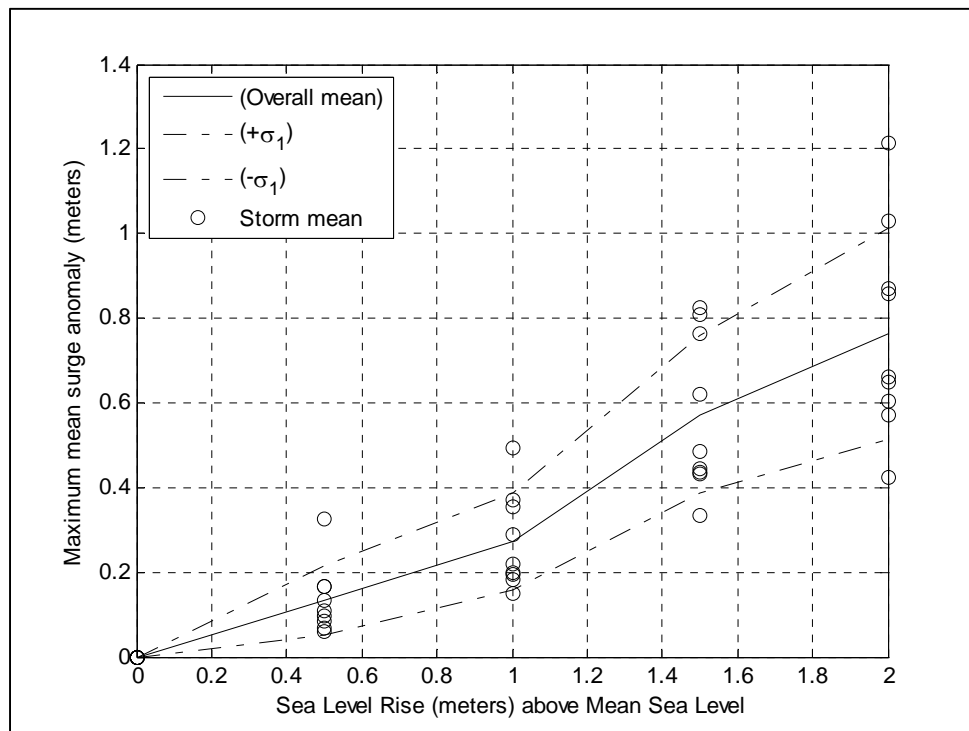
Figure 4.14: Overall impact of SLR on the mean maximum surge quantified by departure from the current MSL surge (anomaly).

These results contradict the findings of Ratcliff and Smith (2011) for Chesapeake Bay, where they found that the mean maximum surge decreased with an increase in SLR, but are in alignment with the results from Smith *et al.* (2010) for the Louisiana coast where they reported an increase in the mean maximum surge with SLR. We believe that local geometry similarity between our study area and the Louisiana coast, in terms of the presence of barrier islands and large areas of low lying topography contribute to this similarity. On the other hand, Chesapeake Bay is a very large water body on its own, which has a much greater average depth and only one connection to the open coast, resulting in a completely different interaction with the open coast surge that would be expected for shallower coastal bays separated from the ocean by low-lying barrier islands.

Although most locations follow the general trend of a mean maximum surge increase with SLR, at some locations there is no surge increase at all, with surge anomalies very close to zero, and at some stations there is a decrease in the mean maximum surge with SLR. The number of recording locations with lower surge anomalies (< 0.2 m) decreases as SLR increases with very few at the 2 m SLR scenario. Considering the four SLR scenarios, the negative outliers were never below 0.5 m of surge decrease with SLR. Conversely, positive surge anomalies reached up to 3 m in selected locations. Most of the negative surge anomalies were in the Intercoastal Waterway, Aransas Pass and directly behind the barrier islands. All of these recording stations are still under high influence of the open coast surge and are very close to the tidal inlets. We also found

small anomalies, but not negative, at specific sides of the bays, strongly related to the relative position of the bay with respect to landfall location (left side of landfall location).

The larger surge anomalies are less than the largest values reported by Smith *et al.* (2010), with increments of up to 3.00 m for only 1.0 m of SLR, mostly due to the stronger storm considered in our study. Similar to Smith *et al.* (2010), we also verified significant surge increases with SLR in areas where the bottom friction (Manning's *n*) was significantly reduced by SLR. Although we found increases much greater than Mousavi *et al.* (2011), we also verified geospatial changes similar to those reported by their study: slight decreases in the surge in the west parts of bays for storms that made landfall to the west of the bays, as well as the surge anomaly increase in the east side of these bays.

Our stronger storms (i.e., *Cp*: 930 mb) had similar forcing conditions as Mousavi *et al.* (2011) simulation of Hurricane Beulah (i.e., *Cp*: 924 mb), but with different tracks. As observed, the landfall location also plays an important role in the intensity of the surge anomalies from SLR, which could be a reason for the differences in surge anomalies ranges. Another important factor is the small range of SLR scenarios (up to 0.75 m) considered by Mousavi *et al.* (2011), with respect to the range of simulations we performed. In our simulations, the effects of the open coast surge are significantly felt in the bays with SLR, as the MSL rises above of the barrier island in several locations. In

the Mousavi *et al.* (2011) study, the barrier islands were represented in their model as vertical barriers, thus natural barriers islands overtopping and overflow was not simulated. Therefore, we conclude that the SLR will also increase the impacts of the open coast surges within the bays of our study area.

When analyzing the inundation extents, we found that the extent of the flooded areas increased from an average of 3,000 km^2 to 6,500 km^2 with SLR intervals of 2.0 m (Figure 4.15). For intense and faster storms (i.e., *Vf*: 37.04 km/h; *Cp*: 930 mb) the flooded extent reached areas almost up to 8,000 km^2 for SLR intervals of 2.0 m. The flooded areas caused by eustatic SLR had a significant increase with 1.5 m of SLR.

When combining the land cover changes and the geometry effects, the variation of the mean maximum surge anomaly with respect to SLR for the study area, considering the entire bay system, can be explained by a linear relationship (Eq. 4.14):

$$\mu_{mmsa} = 0.3933 * \Delta\Phi_{SLR} - 0.0448 \tag{4.14}$$

where the μ_{mmsa} is the overall mean maximum surge anomaly in m. This model has a R^2 of 0.97 and RMSE of 0.05 m (Figure 4.16). Note that, at this point, the meteorological conditions are grouped with each mean for a given SLR interval, considering all simulations results.
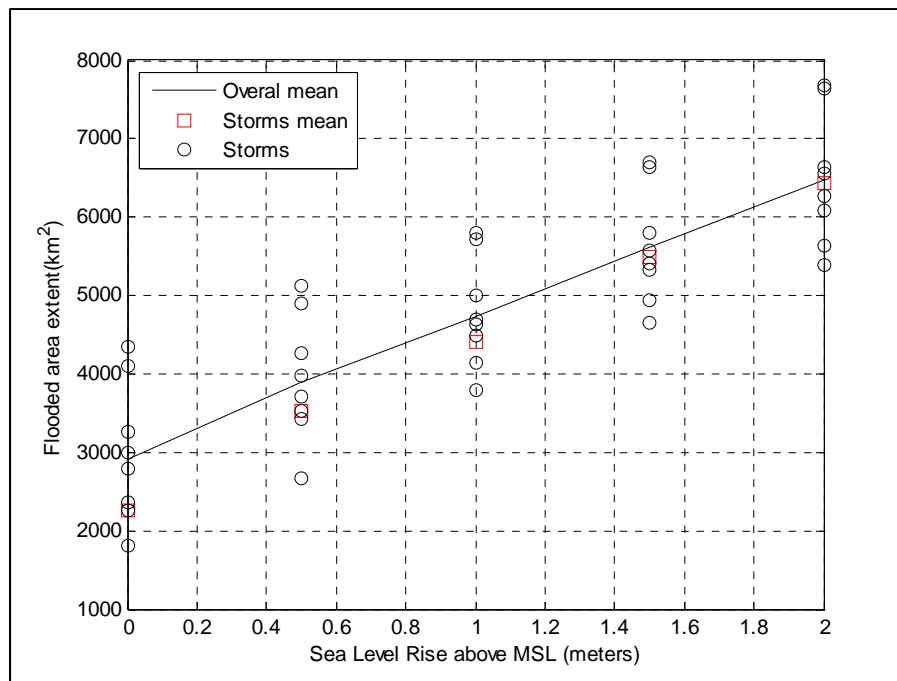
Figure 4.15: Impact of SLR on the storm surge flooding extent. Dashed line is the flooded area by eustatic SLR and black line is the overall mean flooded extent.
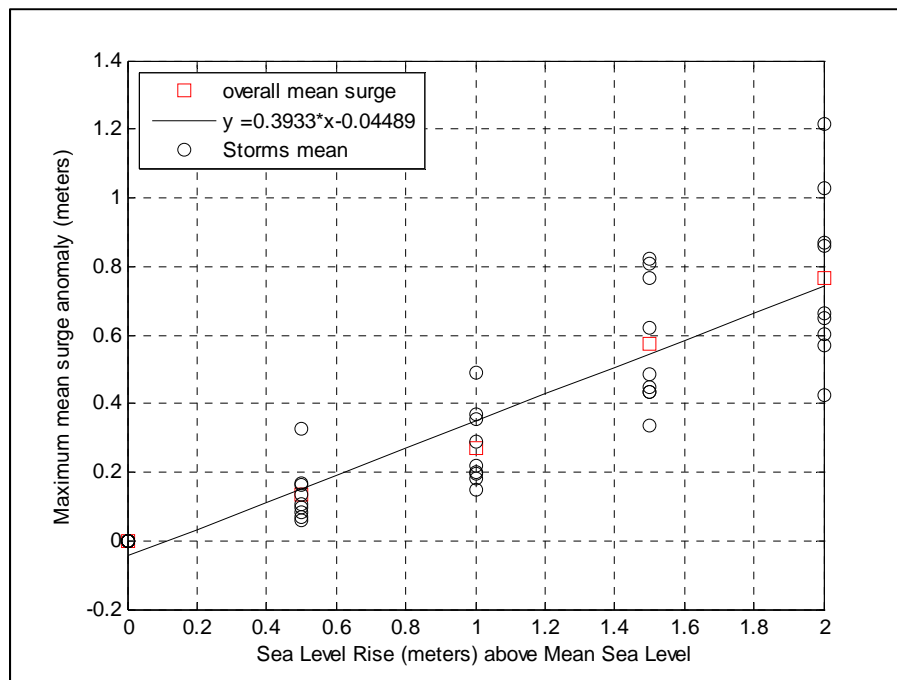
Figure 4.16: Linear model representing the relationship between the SLR and the mean maximum surge anomaly.

However, in this study, we also demonstrated that, although the mean maximum surge anomaly is a function of the SLR increase, it is also a function of the hurricane forward speed, hurricane central pressure and the mean Manning's *n,* and can be described by (Eq. 4.15):

$$\mu_{mmsa} = f(\Delta\Phi_{SLR}, C_p, V_f, \eta) + \Upsilon + e \tag{4.15}$$

where the *Vf* is the hurricane forward speed, Υ are model uncertainties due to other factors (*e.g.,* hurricane landfall location) and *e* is the prediction model error.

Here, we propose a model to predict the mean maximum surge anomalies for the study area based on SLR, hurricane forward speed, hurricane central pressure and the mean Manning's *n.* The multiple linear regression model is presented in (Eq. 4.16):

$$\mu_{mmsa} = 0.230058 * \Delta\Phi_{SLR} - 0.00141 * C_p + 0.01891 * V_f - 22.7682 * n + 2.39138 \tag{4.16}$$

where the μ_{mmsa} is the mean maximum surge anomaly in m, the $\Delta\Phi_{SLR}$ is the SLR increment in m, the *Cp* is the hurricane central pressure in mbars, the *Vf* is the hurricane forward speed in km/h and *n* is the mean Manning's *n* value. Our model has a R^2 of 0.85 and a RMSE of 0.12 m. We assume Υ is equal to zero to simplify the analysis, but it should be noted that are other factors also affect the mean maximum surge anomaly. The fitting of this model against the simulated data is presented in Figure 4.17. Certainly a

more rigorous analyses is needed to develop a robust model to predict mean surge anomalies (i.e., explore alternative statistical models, include a broader range of parameters space), but this model illustrates the predictive capacity of such analyses.

Sensitivity of the effects of land cover change due to sea-level rise on expected damages

Building damages

As expected, the estimated damage increases with SLR. Although the mean expected damage from the simulations neglecting land cover changes increases linearly with SLR, the mean expected damage from the simulations including land cover changes have a more non-linear increase with SLR (Figure 4.18). From this analysis, it is clear that the mean expected damage is increasing when land cover changes are considered. This demonstrates the importance of correctly representing wetland losses when simulating hurricane storm surge under SLR scenarios. While the mean expected damage neglecting land cover changes ranged from approximately 380 million dollars to 700 million dollars, the mean expected damage when land cover changes are considered ranged from approximately 380 million dollars to almost 1.200 billion dollars.
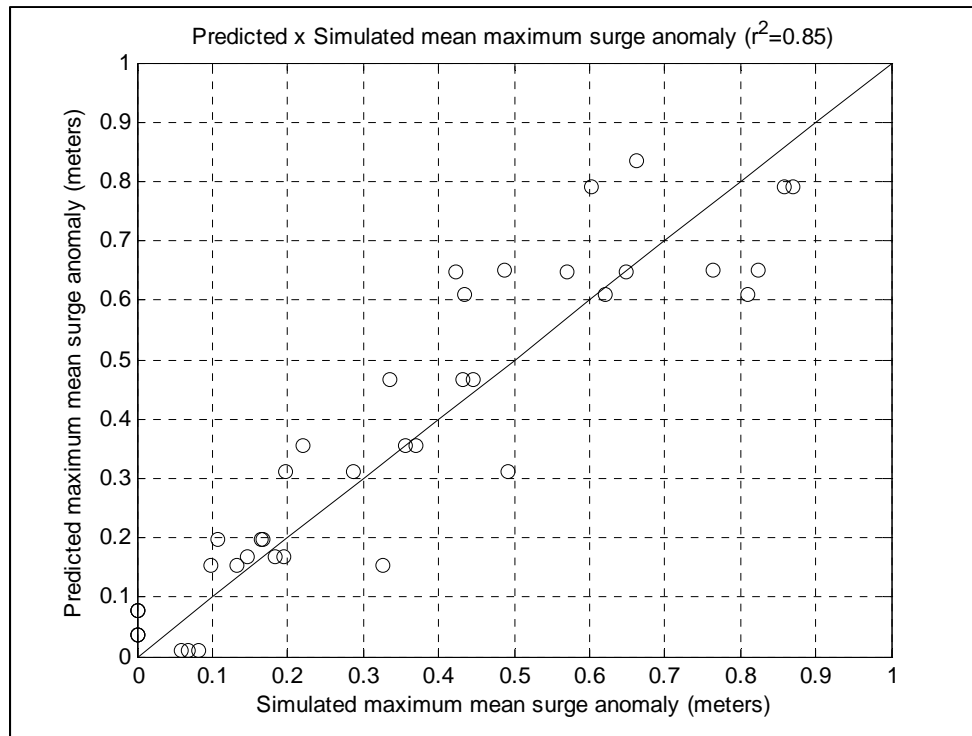
Figure 4.17: Validation of the mean maximum surge anomaly due to SLR predictive model.

When analyzing the expected damage from each individual storm, we verified the same trend of underestimating damages when the land cover changes were neglected. For example, storm A-11-960, which has similar meteorological characteristics as Hurricane Bret but with landfall much closer to the study area, caused an expected damage of 270 million of dollars considering the current MSL and land cover conditions. For SLR intervals of less than 0.5 m, the effects of neglecting land cover changes on damage were minimal. When considering 1.0 m of SLR, the expected damages differed by 74 million of dollars, and for 2.0 m of SLR, the differences reached 400 million dollars.
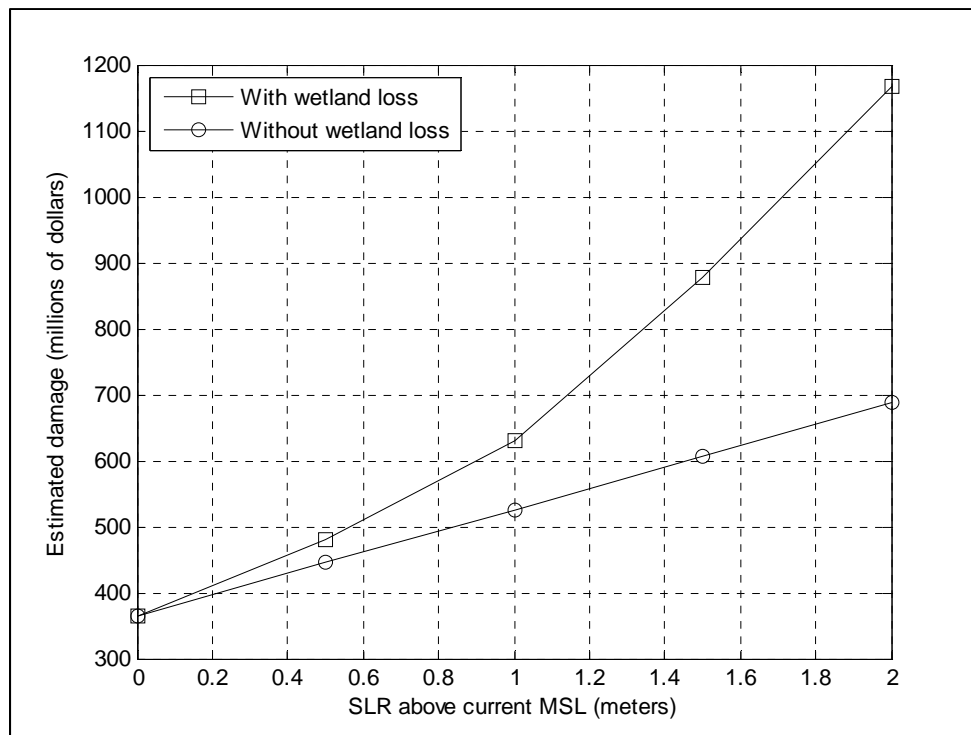
Figure 4.18: Expected mean losses from direct damages to building considering SLR.

Considering storm C-11-960, which has meteorological conditions similar to Hurricane Beulah, but with landfall much closer to the study area, the expected damages for current MSL were around 200 million dollars, which is 40% more than the damage estimated by Frey *et al.* (2010) for Hurricane Beulah at current MSL ($140 million). The estimated damage for Hurricane Beulah under climate change (i.e., *Cp*: 924 mb) and SLR of 0.8 m simulated by Frey *et al.* (2010) was approximately 500 million dollars, which is very close to the results from our storm C-37-930 of approximately 480 million dollars. In this case, when the land cover effects are taken into account, the expected damage for the same scenario raises up to 540 million dollars.

We calculated the mean residual from the building expected damage estimated for each storm, by comparing the expected damage when including and neglecting the land cover effects on surge. Although the residuals are minor for SLR increments of up to 0.5 m, the residuals increase significantly with SLR increments above 0.5 m (Figure 4.19). We expect this change to be related to the significant decrease in frictional resistance at the sea bottom and the increase of momentum penetration to the water column caused by the vegetation lost by a larger amount of SLR. A linear function can approximate the non-linear damage residual with respect to SLR for our study area with an R^2 of 0.91 and RMSE of 67.48 following (Eq.4.17):

$$\Omega_{building} = 238.7 * \Delta\Phi_{SLR} + 60.18 \tag{4.17}$$

where $\Omega_{building}$ is the expected direct damage to building residual in millions of dollars. This relationship is important for demonstrating the influence of changes in the dissipation and forcing mechanisms due to SLR on expected building damage. Note this relationship is specific to the study area topography and building types and layouts.
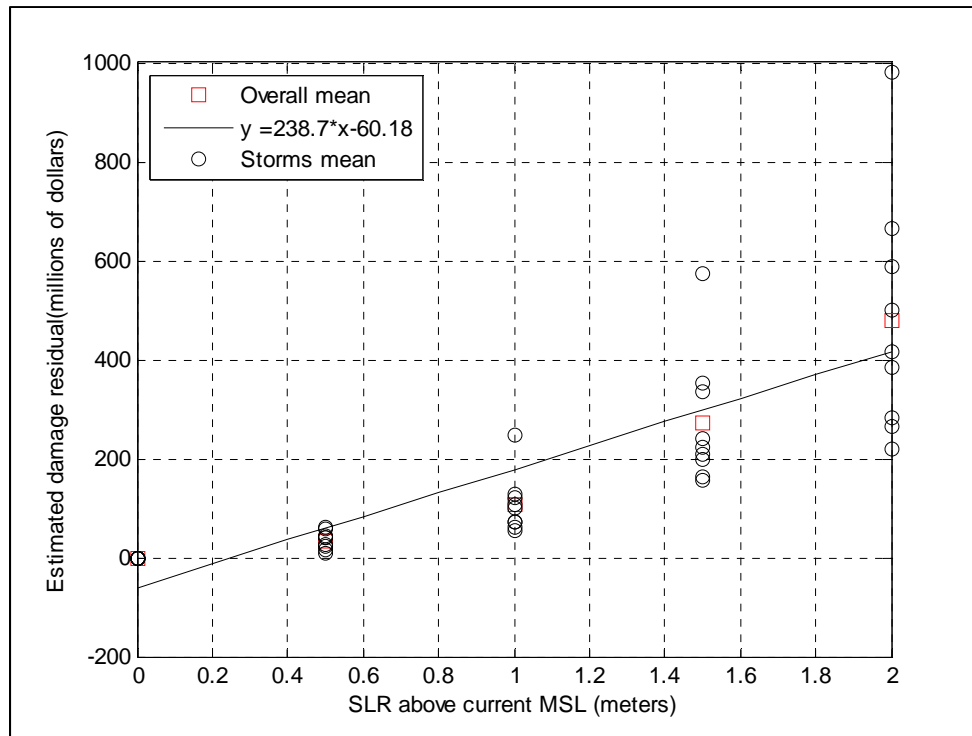
Figure 4.19: The mean expected residual (to direct building damage) when comparing simulations with and without land cover changes.

The damage residual is strongly correlated to the storms' meteorological conditions (Figure 4.20). We found that the intensification of central pressure increased the damage residual. This effect is particularly important for studies considering the intensification of hurricanes with climate change (e.g., Knutson *et al.* 2010; Elsner *et al.* 2008). This effect is negligible for SLRs less than 0.5 m, where the damage residual was almost zero. The SLR increment of 1.0 m led to a mean damage residual of approximately 40 million dollars, when comparing the central pressure of 930 mb to 960 mb. This difference increases to 130 million dollars for SLR increments of 2.0 m. The hurricane forward speed is also correlated to the damage residual, with faster storms increasing the

damage residual. Again, the residual is negligible for SLRs less than 0.5 m, but increases almost linearly with SLR, resulting in an approximately additional 40 million dollars in the faster storms for 2.0 m of SLR.
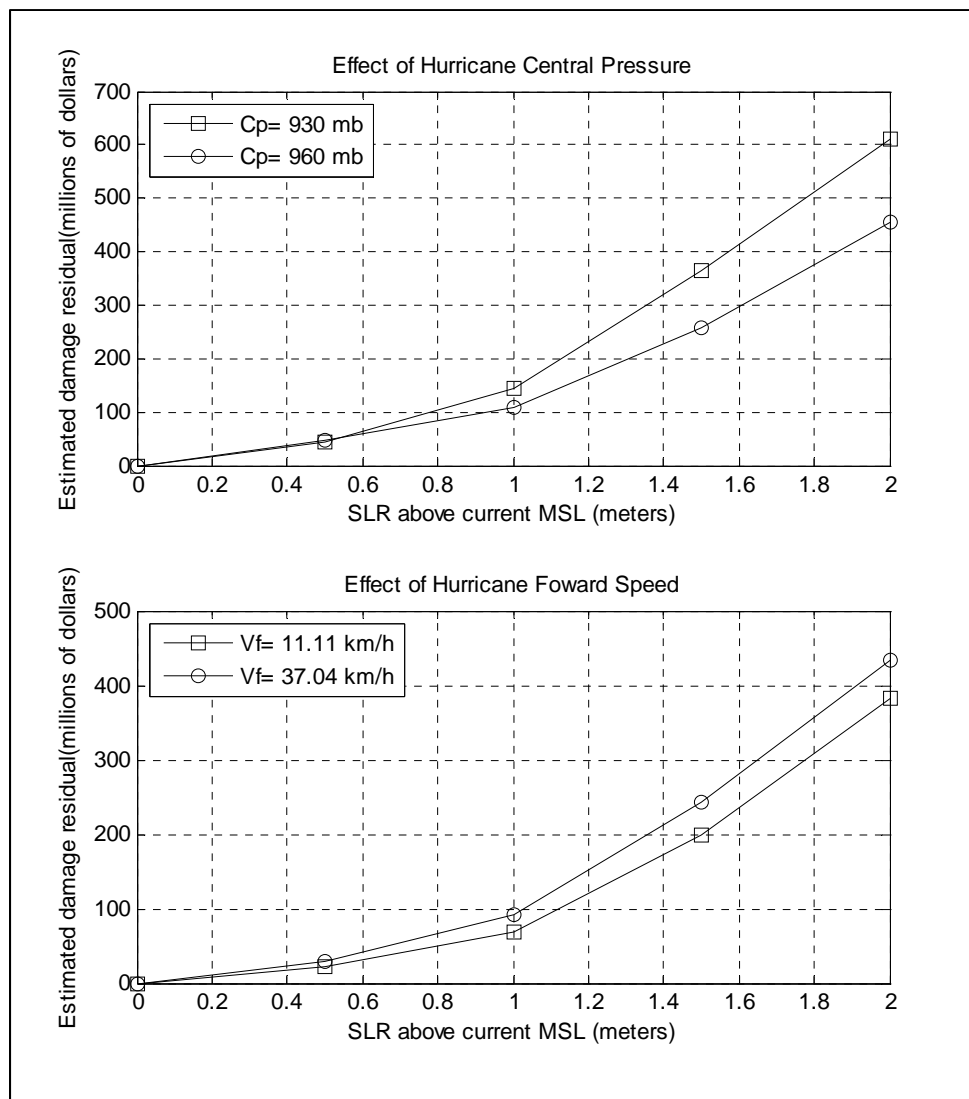
Figure 4.20: Effects of hurricane central pressure and forward speed on the expected building direct damage. Each line presents the average of 3 hurricane landfall locations.

Here we propose a model to estimate the relative increase in building damage due to land cover changes from SLR (Figure 4.21).
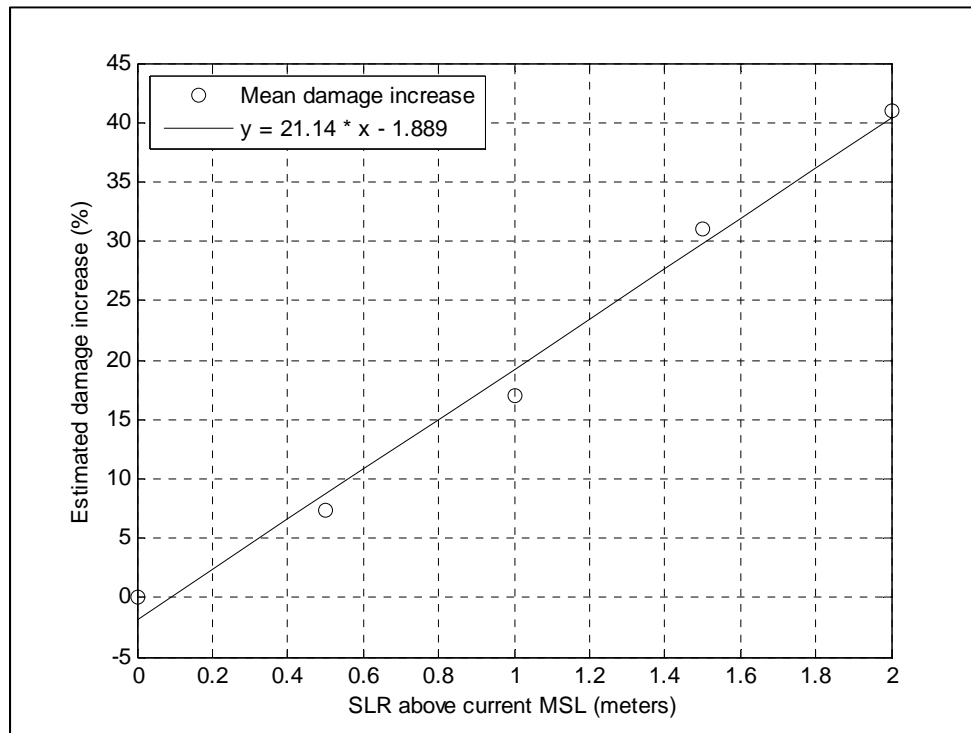
Figure 4.21: Estimated damage increase due to land cover changes from SLR.

In terms of percentage, the expected damage increases almost linearly with SLR, and can be described by (Eq. 4.18) with an R^2 of 0.98 and a RMSE of 2 %:

$$\Gamma_{\%} = 21.14 * \Delta\Phi_{SLR} - 1.889$$

(4.18)

where $\Gamma_{\%}$ is the estimated building damage increase in percentage due to land cover changes. This equation represents an approximation of the underestimation of calculated damage for simulations that do not consider the changes in land cover due to SLR. We can also associate the relative damage increase to the actual mean Manning's *n* reduction at the sea bottom (Figure 4.22) with a linear relationship (Eq. 4.19):

$$\Gamma_{\%} = -2692 * \eta + 148.4$$

(4.19)

where $\Gamma_{\%}$ is the estimated building damage increase in percentage due to land cover changes. This equation provides an estimate of the impact of land cover changes due to SLR quantified by changes in Manning's *n* to damage estimate with an R^2 of 0.94 for our study area, which can be used as a guide for other locations.

Population affected

Unlike the direct damage to buildings, when considering the population affected, the simulations with changes in the land cover by SLR and the simulations neglecting it, yielded very similar results for SLR increments up to 1.0 m. For both cases, the average population affected from the 9 storms was 35 thousand people for 0.5 SLR and 42 thousand people for 1.0 m of SLR. With 1.5 to 2.0 m of SLR, there was a mean difference of approximately 5 thousand people affected, where the simulations considering land cover changes led to the higher numbers.
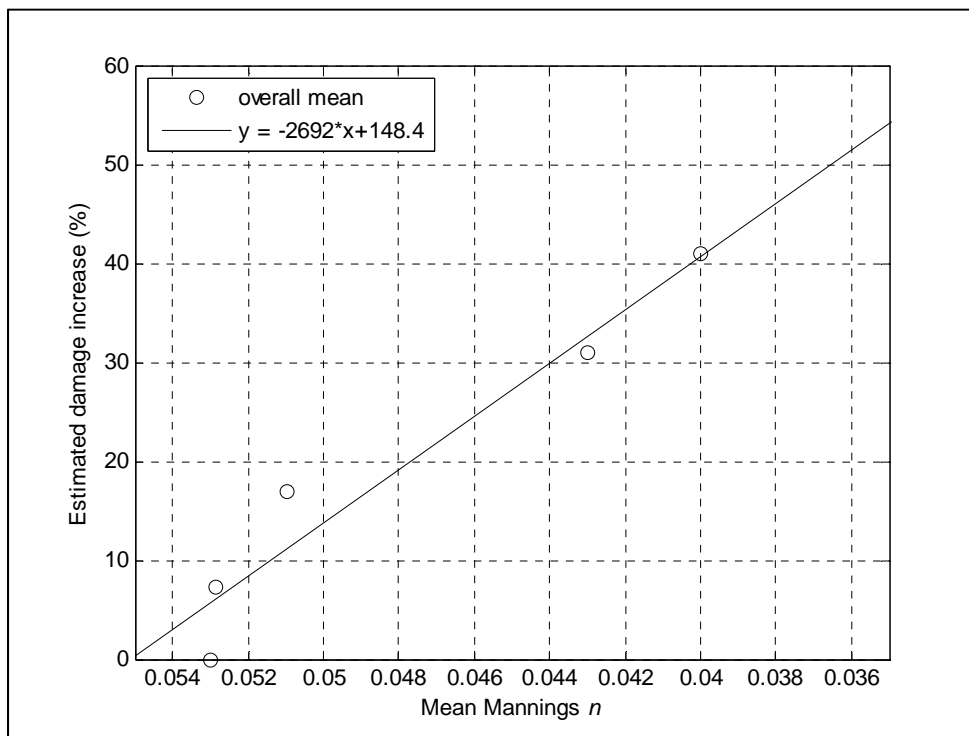
Figure 4.22: Relation between decreases in frictional drag at the sea bottom represented by the Manning's *n* and the estimated damage increase.

For SLR scenarios below 1.0 m, the residual was always less than 2 thousand people, which given model uncertainties, can be considered negligible (Figure 4.23). For some storms, we verified a small negative residual which is caused by different spatial flooding extents. Note that the population affected analyses does not take into consideration the depth variation within the block, which is one of the most significant impacts of SLR on the land cover changes of hurricane storm surge. The stronger and faster storms slightly increased the residuals, especially for SLR increments higher than 1.0 m.
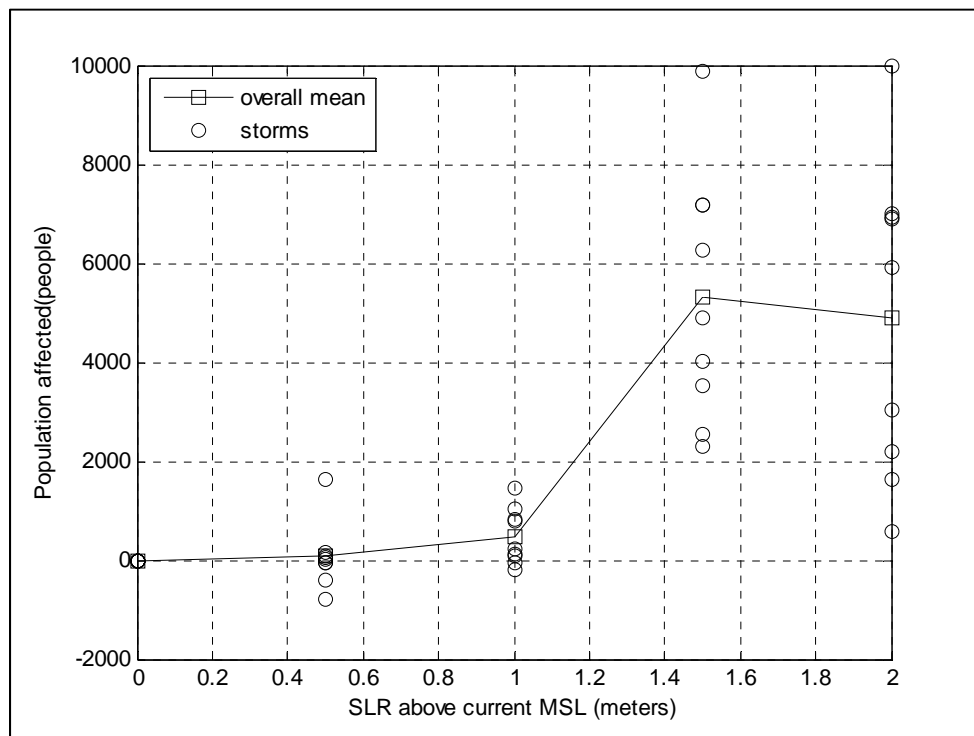
Figure4.23: The mean expected residual (to population affected) from comparing the simulations with and without land cover changes.

Irish *et al.* (2010) analyzed the impact of barrier island degradation due to SLR on population affected by hurricane storm surge in the City of Corpus Christi. They found that although there were some impacts of the barrier island degradation to the population affected, considering the simulated climate change scenario for the 2030s, the overall impact of the higher SLR considered for 2080s (0.87 m) was not significantly greater. Here, we also demonstrate that the population affected is not significantly impacted for SLR up to 1.0 m when changes in land cover are considered. A significant increase in

the population affected can be observed from 1.0 to 1.5 m of SLR, which was expected following the mean maximum surge residual increase due to land cover changes.

Businesses Impacted

Similar to the results for direct damage to buildings, integrating land cover changes did significantly affect surge impact on businesses. The numbers of businesses affected in each category (Table 4.2) per storm are presented in Table 4.4. Although there is no trend that could explain the variation of number of businesses in each category and SLR, the total number of businesses impacted increased with SLR. This is mostly due to the damage categorization scheme adopted. The business can move from one category to other depending on the severity (water depth) of the flood. The residual of the average number of businesses under nuisance flooding increases with up to 1.0 m of SLR but declines thereafter. The residuals are negligible for the minor, major and catastrophic categories for SLR increments up to 0.5 m. The residual of the number of businesses under minor flooding is approximately constant (around 200 businesses) from 1.0 m of SLR to 2.0 m of SLR. For major flooding, the residual is still negligible up to 1.0 m of SLR but increases thereafter. The residual in the catastrophic flooding category increases significantly from 100 businesses with 1.0 m of SLR to almost 700 with 2.0 m of SLR (Figure 4.24).

Table 4.4: Residual of the number of businesses affected.

Storm	Flooding	SLR (m)			
		0.5	1	1.5	2
A-11-960	Nuisance	269	350	-17	148
	Minor	-83	273	243	74
	Manor	-3	3	562	121
	Catastrophic	-1	34	285	1091
A-37-960	Nuisance	203	178	210	579
	Minor	104	247	42	231
	Manor	-5	151	240	141
	Catastrophic	-53	54	545	781
A-37-930	Nuisance	63	344	659	480
	Minor	-120	-4	218	588
	Manor	153	-136	70	278
	Catastrophic	77	440	347	571
B-11-960	Nuisance	147	254	108	-199
	Minor	19	321	212	111
	Manor	-5	96	373	371
	Catastrophic	4	3	289	808
B-37-960	Nuisance	219	76	51	-34
	Minor	-116	264	56	165
	Manor	86	-32	187	40
	Catastrophic	-17	99	473	745
B-37-930	Nuisance	125	87	114	359
	Minor	105	110	97	11
	Manor	51	26	20	209
	Catastrophic	-23	290	653	755
C-11-960	Nuisance	33	150	274	11
	Minor	-70	204	272	218
	Manor	-1	-127	300	326
	Catastrophic	0	-1	-64	277
C-37-960	Nuisance	155	155	190	-54
	Minor	62	112	125	123
	Manor	-2	145	358	203
	Catastrophic	0	-1	190	629
C-37-930	Nuisance	54	248	49	-79
	Minor	5	70	240	138
	Manor	-1	37	159	259
	Catastrophic	-3	-17	154	373

The effects of the storm meteorological conditions on the residual number of businesses are not as clear as with the direct damage to buildings. The stronger storms increased the residuals from 1.0 m of SLR but decreased the residual for SLR of 2.0 m. The effect of

forward speed is also almost negligible, as the only SLR interval with a different residual due to forward speed is the 1.5 SLR, with the fastest storms increasing the residual number.
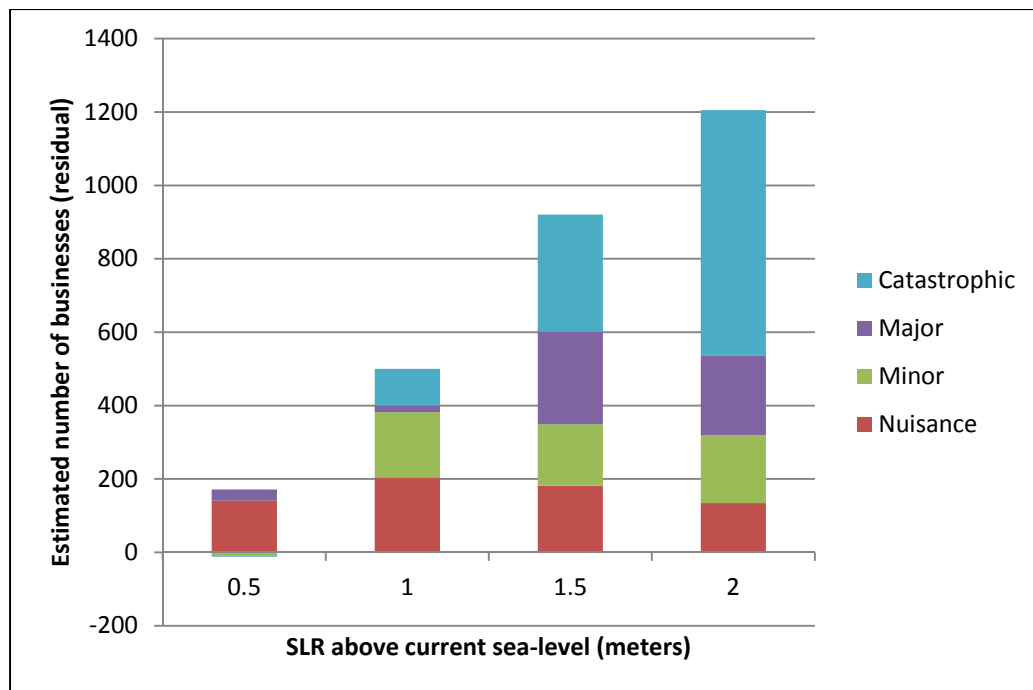
Figure 4.24: The mean expected residual (to businesses affected) from comparing the simulations with and without land cover changes.

Projected scenarios

To evaluate the sensitivity of damage estimation with respect to changes in land cover due to SLR ,we considered six SLR projections published in the literature to estimate the differences in expected direct damage to buildings, population affected and businesses under catastrophic flooding (Table 4.5). For the SLR estimates from the IPCC (2007),

the lower prediction (0.2 m) led to negligible residuals for building, population and businesses. The upper bound (0.6 m) resulted in a 10% increase in building damages, but minor changes in population affected or business under catastrophic flooding. The intervals proposed by Jevrejeva (2010), Vermeer (2009) and Pfeffer (2008) from 0.6 m to 2.0 m led to much greater residuals. The upper bound (2.0 m) resulted in building damage residuals of approximately 400 million dollars, representing an increase of approximately 35 % from the initial estimate. The population affected residual was approximately 5 thousand people and an additional 500 businesses affected under catastrophic flooding. When looking at the current SLR plus subsidence rate we found an increase in building damages of around 87 million dollars (15%), 374 people and 73 businesses under catastrophic flooding.

Table 4.5: Estimated residuals for residential damage, inundated areas and population affected by 2100 estimated Sea-level Rise scenarios.

Source	SLR estimate (m)		Building damage (Millions of US$)		Population Affected		Businesses under catastrophic flooding	
	min	max	min	max	min	max	minx	max
IPCC (2007)	0.2	0.6	4.9	40.8	30	155	0	19
Jevrejeva (2010)	0.6	1.8	40.8	387.0	155	5069	19	529
Vermeer (2009)	0.75	1.90	64.5	432.0	277	4990	49	599
Pfeffer (2008)	0.8	2.0	73.7	479.5	317	4911	59	670
Rahmstorf (2007)	0.5	1.40	28.1	231.8	75	4339	0	275

SUMMARY AND CONCLUSIONS

We analyzed the impacts of SLR on hurricane storm surge, building damage, population and businesses affected for coastal bays located on the Texas central coast. To evaluate the effects of SLR on surge elevation, we considered the impact of changes in land cover as well as changes in bay geometry caused by SLR. The effects of land cover change due to SLR were quantified by the changes in the frictional drag at the sea bottom and the changes in momentum transfer from the wind to the water column caused by vegetation losses. First, we evaluated the impacts of land cover changes due to SLR on the surge response. Second, we evaluated the impacts of neglecting land cover changes due to SLR on the surge response. Finally, we evaluated the overall effect of SLR on the mean maximum surge and the consequent extent of the flooded areas. The importance of considering the effects of wetland losses due to SLR on hurricane surge was quantified by the increase in the expected damages to buildings, population and business affected.

Understanding the effects of SLR on hurricane storm surge is crucial to correctly incorporate future climate variability in coastal design, planning and management. In this study, we showed that the mean maximum surge increases with SLR in addition to the expected SLR itself. The changes in geometry and land cover as a consequence of SLR play an important role in the resulting surge response. The variability of the surge response is also greatly affected by the storm meteorological conditions and the location of interest. Understanding this relationship is crucial to correctly estimate future hurricane storm surge risk under a changing climate. The practice of adding a SLR

increment to current storm surge simulations might severely underestimate surge risk in some areas.

Neglecting land cover changes due to SLR did significantly affect the expected damage for direct losses to buildings. The residual increased with SLR and was affected by the storm meteorological conditions. Stronger and faster storms were associated with increased residuals. Although there was an increase in the damage residual, for SLR below 0.5 m, this increase was almost negligible.

The impacts of land cover changes arising from SLR for damage estimation are important for SLR scenarios over at least 0.5 m. For example, when considering the SLR of 0.6 m from the IPCC (2007) high emission scenario, we demonstrated an increase of 10% on the building expected damage. The assimilation of land cover changes is especially important when calculating expected damages for SLR scenarios on the upper bound. For example, the SLR of 2.0 m proposed by Pfeffer (2008) led to an increase of 35% on the expected direct damage to buildings and to more than 500 businesses being affected under the catastrophic flooding category.

The methodology presented here can be easily applied to other coastal locations. Although the values and relationship presented are strongly related to local environment characteristics, it demonstrates the importance of incorporating land cover changes when simulating storm surges under climate changes. Also, a more sophisticated ecosystem

model could be applied to better represent the effects of SLR on coastal vegetation and

therefore leading to a more realistic future storm surge prediction.

CHAPTER V

SUMMARY AND CONCLUSIONS

Hurricanes are one of the most costly natural disasters in the US, being responsible for several billion dollars in damage, dramatic evacuations and loss of lives. Current climate research arguably is indicating an increase in the mean sea-level and a likely intensification of hurricanes in the next century. The sea-level rise (SLR) is one of the most dangerous processes of climate change threatening coastal communities. It is also expected that damage from hurricanes will significantly increase in the next century due to the combined effect of SLR and more intense hurricanes. Thus, it is crucial to understand how SLR affects hurricane storm surges and to enhance our capability to spatially predict coastal risks caused by climate change.

Numerical simulation of hurricane storm surge is an important tool to predict base flood elevations in coastal areas. Reliable simulations using very high resolution are currently carried out using High Performance Supercomputers (HPC). Here, we presented a novel framework to integrate Geographical Information Systems (GIS) and hurricane storm surge models. This framework is composed of a geodatamodel specifically designed to the requirements of hurricane storm surge modeling and a set of ArcGIS tools to pre- and post-process model input/output. We successfully designed the framework to perform with the SWAN+ADCIRC hurricane storm surge models, but it could be easily adapted to work with other hurricane models. Integrating geospatial technologies with

hurricane storm surge modeling is beneficial not only to take full advantage of geospatial data, but also to easily convert complex model results to maps and thereafter share hurricane risk information with stakeholders, government officials, or the general public, increasing the outreach of hurricane storm surge modeling. Current GIS web applications, servers, cloud functionality and web services are enhancing GIS outreaching capacity to any regular internet user.

An example of geospatial information crucial to hurricane storm surge modeling is land cover. The land cover is expected to impact the energy dissipation and forcing mechanisms of hurricane storm surge. The energy dissipation mechanisms are impacted by the frictional drag at the sea bottom, and the forcing mechanisms are impacted by the momentum transmitted to the water by the wind. There are several databases representing land cover in the US. We investigated the impact in the surge response from the datasets available from the National Land Cover (1992, 2001, and 2006), the Coastal Change Analyses Program (1996, 2001, and 2006) and the National Wetlands Inventory (2011). We also quantified the uncertainty expected from the different datasets. We found that the land cover has a significant impact on the surge response. We also found that the residuals are strongly dependent on location and meteorological conditions.

Quantifying uncertainties due to land cover is crucial for better representing model reliability among other uncertainties (e.g., wind forcing, bathymetry) and for providing an expected range of confidence in model results, and accordingly for coastal structure

design, floodplain delineation or coastal planning. We provided estimates that can be used as a baseline for other areas to quantify expected model uncertainties arising from land cover specifications. This information is especially important for: areas with scarce historical hurricane surge data, where model validation is almost impossible and choosing the appropriate land cover is almost a matter of best guess; when considering planning under changing climate, where hurricanes are expected to intensify; and to design structures in locations where the residuals are consistently high.

Given the expected rise in the mean sea-level in the next century, we also investigated the impact of land cover change due to SLR, especially wetlands and other coastal vegetation, on the surge response and consequent damage. The SLR is expected to affect the geometry of the bays in the sense that the water depth will increase and the surface area of the water will also increase. SLR is also expected to impact the forcing and dissipation mechanisms of hurricane storm surge due to changes in land cover (mainly drowning of coastal vegetation). Even when changes in land cover due to SLR are neglected, the mean storm surge increases with SLR. In other words, simply adding the SLR to current surges can lead to underestimation of future risks of coastal flooding under a changing climate in certain locations. We applied a simplified model to simulate wetland losses due to SLR and investigated the impacts of these losses on subsequent flooding and damage. We showed that the effects of considering land cover changes due to SLR significantly impact the maximum surge, especially for SLR increments over one m. Neglecting land cover changes also significantly impact estimated damage to

buildings and businesses. Although we applied a simplified model to represent wetland losses due to SLR, this methodology could be easily repeated with a more complex model or could include the effects of morphological changes due to SLR whenever they became better understood.

Future work from this research includes the investigation of the effects of future land cover changes on the surge response, optimizing wetland restoration projects to reduce surge damage and the application of dynamic models to quantify population at risk under climate change scenarios.

REFERENCES

Alongi, D. M. (2008) "Mangrove forests: Resilience, protection from tsunamis, and responses to global climate change." *Estuarine, Coastal and Shelf Science,* (76), 1-13.

Anderson, J.F.; Hardy, E.E.; Roach, J.T. and Witmer, R.E. (1976) *A land use and land cover classification system for use with remote sensor data.* U.S. Geological Survey Professional Paper *964, 28* pp. U.S. Geological Survey, Washington, District Columbia.

Aquaveo (2012) Surface Modeling System (SMS). http://www.aquaveo.com/sms Accessed 07 April 2011.

Arcement and Scneider (1989) *Guide for selecting Manning's roughness coefficients for natural channels and flood plains.* U.S. Geological Surver Water-Supply Paper 2339, U.S. Geological Survey, Denver, Colorado.

Atkinson, J., H. Roberts, S.C. Hagen, S. Zhou, P. Bacopoulos, S. Medeiros, J. Weishampel and Z. Cobell (2011) "Deriving Frictional Parameters and Performing Historical Validation for an ADCIRC storm surge model of the Florida gulf coast." *Florida Watershed Journal,* 4 (2), 22-27.

Bjarnadottir, S.; Li, Y. and Stewart, M. G. (2011). "Social vulnerability index for coastal communities at risk to hurricane hazard and a changing climate." *Natural Hazards,* 59(2), 1055-1075.

Blain, C. A.; Linzell, R., S. Massey, C.; and Chu, P. (2010) *Validation Test Report for the Advanced CIRCulation Model (ADCIRC) v45.11*. Naval Research Laboratory, United States Navy, Stennis Space Center, Slidell, Mississippi.

Booij, N. Ris, R. C. and Holthuijsen, L. H. (1999) A third generation wave model for coastal regions. Model Description and Validation. *Journal of Geophysical Research* (104) 7649-7666.

Brody, S.D., Zahran, S., *Highfield, Wesley E., Grover, H., Vedlitz, A. Identifying the Impact of the Built Environment on Flood Damage in Texas. (2007). *Disasters,* 32(1), 1-18.

Bunya, S., Dietrich, J., Westerink, J., Ebersole, B., Smith, J., Atkinson, J., Jensen, R., Resio, D., Luettich, R., Dawson, C., Cardone, V., Cox, A., Powell, M., Westerink, H., and Roberts, H. (2010). "A High-Resolution Coupled Riverine Flow, Tide, Wind, Wind Wave, and Storm Surge Model for Southern Louisiana and Mississippi. Part I: Model Development and Validation." *Monthly Weather Review*, 345-377.

Cardone, V., and Cox, A. (2009). "Tropical cyclone wind field forcing for surge models: critical issues and sensitivities." *Natural Hazards*, 29-47.

Chen, C., Liu, H., and Beardsley, R. (2003). "An unstructured grid, finite-volume, three-dimensional, primitive equations ocean model: Application to coastal ocean and estuaries." *Journal of Atmospheric and Oceanic Technology*, 159-186.

Chen, Q., Wang, L., Zhao, H., and Douglass, S. (2007). "Prediction of storm surges and wind waves on coastal highways in Hurricane-Prone areas." *Journal of Coastal Research*, 23(5) 1304-1317.

Chu-Agor, M., Munoz-Carpena, R., Kiker, G., Emanuelsson, A., and Linkov, I. (2011). "Exploring vulnerability of coastal habitats to sea level rise through global sensitivity and uncertainty analyses." *Environmental Modelling & Software*, 593-604.

Church, J.; White, N.; Aarup, T.; Wilson, W. S.; Woodworth, P.L.; Domingues, C.M.; Hunter, J.R. and Lambeck, K. (2008). "Understanding global sea levels: past, present and future." *Sustainability Science,* 3(1), 9-22.

Cooper, M., Beevers; M. and Oppenheimer, M (2008). "The potential impacts of sea level rise on the coastal region of New Jersey, USA." *Climatic Change,* 90(4), 475-492.

Cowardin, L. M.; Carter, V.; Golet, F.C.; and LaRoe, E.T. (1979) *Classification of Wetlands and Deepwater Habitats of the United States*. U.S. Fish and Wildlife Service. FWS/OBS-79/31. 130pp Washington District Columbia.

Craft, C., Clough, J., Ehman, J., Joye, S., Park, R., Pennings, S., Guo, H., and Machmuller, M. (2009). "Forecasting the effects of accelerated sea-level rise on tidal marsh ecosystem services." *Frontiers in Ecology and the Environment*, 73-78.

Dietrich, J., Bunya, S., Westerink, J., Ebersole, B., Smith, J., Atkinson, J., Jensen, R., Resio, D., Luettich, R., Dawson, C., Cardone, V., Cox, A., Powell, M., Westerink, H., and Roberts, H. (2010). "A High-Resolution Coupled Riverine Flow, Tide, Wind, Wind Wave, and Storm Surge Model for Southern Louisiana and Mississippi. Part II: Synoptic Description and Analysis of Hurricanes Katrina and Rita." *Monthly Weather Review*, 378-404.

Dietrich, J., Zijlema, M., Westerink, J., Holthuijsen, L., Dawson, C., Luettich, R., Jensen, R., Smith, J., Stelling, G., and Stone, G. (2011). "Modeling hurricane waves and storm surge using integrally-coupled, scalable computations." *Coastal Engineering*, 45-65.

Dobson, J.E.; Bright, E.A.; Ferguson, R.L. ; Field, D.W. ; Wood, L.L.; Haddad, K.D.; Iredale, H.; Jensen, J.R.;Klemas, V.V. ; Orth, R.J. and Thomas, J.P. (1995). *NOAA Coastal Change Analysis Program (C-CAP): guidance for regional implementation*,

NOAA Technical Report NMFS 123, U.S. Department of Commerce, Seattle, Washington.

Ebersole, B., Westerink, J., Bunya, S., Dietrich, J., and Cialone, M. (2010). "Development of storm surge which led to flooding in St. Bernard Polder during Hurricane Katrina." *Ocean Engineering*, 91-103.

Elmer, F., Thieken, A., Pech, I., and Kreibich, H. (2010). "Influence of flood frequency on residential building losses." *Natural Hazards and Earth System Sciences*, 2145-2159.

Elsner, J.; Kossin, J.P. and Jagger, T.H. (2008). "The increasing intensity of the strongest tropical cyclones." *Nature*, 92-95.

Emanuel, K. (2005). "Increasing destructiveness of tropical cyclones over the past 30 years." *Nature,* 436(7051), 686-688.

Environmental Systems Research Institute (2012a) Data models. http://support.esri.com/en/downloads/datamodel Accessed 9 March 2011.

Environmental Systems Research Institute (2012b) Fundamentals of TIN triangulation in ArcGIS. http://help.arcgis.com/en/arcgisdesktop/10.0/help/index.html#//00600000000z000000.htm Accessed 9 March 2011.

Federal Emergency Management Agency (2012) Hazards U.S. - Multi-Hazard (HAZUS-MH) http://www.fema.gov/plan/prevent/hazus/ Accessed 02 March 2011.

Frazier, T.; Wood, N.; Yarnal, B. and Bauer, D.H. (2010). "Influence of potential sea level rise on societal vulnerability to hurricane storm-surge hazards, Sarasota County, Florida." *Applied Geography,* 30(4), 490-505.

Frey, A., Olivera, F., Irish, J., Dunkin, L., Kaihatu, J., Ferreira, C., and Edge, B. (2010). "Potential impact of climate change on hurricane flooding inundation, population affected and property damages in Corpus Christi." *Journal of the American Water Resources Association*, 1049-1059.

Fry, J., Xian, G., Jin, S., Dewitz, J., Homer, C., Yang, L., Barnes, C., Herold, N., and Wickham, J., 2011. "Completion of the 2006 National Land Cover Database for the Conterminous United States", *Photogrammetric Engineering & Remote Sensing*, 77(9),858-864.

Galbraith, H., Jones, R., Park, R., Clough, J., Herrod-Julius, S., Harrington, B., and Page, G. (2002). "Global climate change and sea level rise: Potential losses of intertidal habitat for shorebirds." *Waterbirds*, 173-183.

Glennon, A. (2010). "Creating and Validating Object-Oriented Geographic Data Models: Modeling Flow within GIS." *Transactions in GIS*, (14)23–42.

Goodchild, M. F. (2005) *Spatial Modeling with GIS*. in Longley P A, Maguire D J, Goodchild M F, Rhind D (eds.) *Geographical information systems and science*. John Wiley & Sons, New York, New York.

Hallegatte, S. (2012). "Economics: The rising costs of hurricanes." *Nature Climate Change,* 2(3), 148-149

Homer, C. C. Huang, L. Yang, B. Wylie and M. Coan. (2004). "Development of a 2001 National Landcover Database for the United States". *Photogrammetric Engineering and Remote Sensing*, 70(7) 829-840.

Horton, R.; Herweijer, C.; Rosenzweig, C.; Liu, J.; Gomitz, V. and Ruane, A., C. (2008) "Sea level rise projections for current generation GCMs based on the semi empirical model" *Geophysical Research Letters*, (35), L02715.

Huang, Y., Weisberg, R. H., and Zheng, L. Y. (2010). "Coupling of surge and waves for an Ivan-like hurricane impacting the Tampa Bay, Florida region." *Journal of Geophysical Research-Oceans*, (115), C12009.

Hunter, J. (2010) "Estimating sea-level extremes under conditions of uncertain sea-level rise" *Climatic Change,* (99), 331-350.

Infogroup (2012) Reference USA. http://www.referenceusa.com/Home/Home Accessed 23 July 2011

Intergovernmental Panel on Climate Change, (2007) *Climate Change 2007: The Physical Science Basis. Contribution of Working Group I to the Fourth Assessment Report of the Intergovernmental Panel on Climate Change* [Solomon, S., D. Qin, M. Manning, Z. Chen, M. Marquis, K.B. Averyt, M.Tignor and H.L. Miller (eds.)]. Cambridge University Press, Cambridge, United Kingdom and New York, New York.

Irby, D., Mohammadi-Aragh, M., Moorhead, R., and Amburn, P. (2009). "Improving the Understanding of Hurricanes: Visualizing Storm Surge." *Oceans*, (1-3), 1442-1445.

Irish, J., Williams, B., Militello, A., and Mark, D. (2005). "Regional-scale storm-surge modeling of Long Island, New York, USA." *Coastal Engineering*, (1-4), 1565-1577.

Irish, J., L.; Frey, A., E.; Rosati, J., D.; Olivera, F.; Dunkin, L., M.; Kaihatu, J., M.; Ferreira, C., M.; Edge, B., L. (2010) "Potential Implications of global warming and barrier island degradation on future hurricane inundation, property damages and population impacted" *Ocean and Coastal Management* (53), 645-657.

Jelesnianski, C. P., J. Chen, and W. A. Shaffer, (1992) *SLOSH: Sea, lake, and overland surges from hurricanes*. National Oceanic and Atmospheric Administration, Tech. Report NWS 48, 71 pp. [Available from NOAA/AOML Library, 4301 Rickenbacker Cswy., Miami, Florida 33149.]

Jevrejeva, (2010) "How will sea level respond to changes in natural and anthropogenic forcing by 2100" *Geophysical Research Letter*, (37) L07703.

Jonkman, S., Kok, M., and Vrijling, J. (2008). "Flood risk assessment in the Netherlands: A case study for dike ring South Holland." *Risk Analysis*, 1357-1373.

Knutson, T.;. McBride J.; Chan, J.; Emanuel, K.; Holland, G.; Landsea, C.; Held, I.; Kossin, J.P.; Srivastava, A.K. and Sugi, M. (2010). "Tropical cyclones and climate change." *Nature Geoscience,* 3(3), 157-163.

Lin, N., Emanuel, K.; Smith, J. A. and Vanmarcke, E. (2010). "Risk assessment of hurricane storm surge for New York City." *Journal of Geophysical Research-Atmospheres,* (115) D18121.

Lin, N.; Emanuel, K.; Oppenheimer, M. and Vanmarcke, E. (2012). "Physically based assessment of hurricane surge threat under climate change." *Nature Climate Change*. In press.

Loder, N., Irish, J., Cialone, M., and Wamsley, T. (2009). "Sensitivity of hurricane surge to morphological parameters of coastal wetlands." *Estuarine Coastal and Shelf Science*, 625-636.

Lott, N and Ross, T. (2006) Tracking and Evaluating U.S. Billion Dollar Weather Disasters, 1980-2005. National Climatic Data Center (NCDC) http://www1.ncdc.noaa .gov/pub/data/papers/200686ams1.2nlfree.pdf Accessed 12 July 2011

Luettich, R. and Westerink, J. (2004). *Formulation and numerical implementation of a 2D/3D ADCIRC Finite Element Model Version 4.46.* http://adcirc.org/adcirc_theory_2004_12_08.pdf. Accessed 13 November 2010

Maidment, D. R., ed. (2002) *Arc Hydro: GIS for water resources*. Redlands, California: ESRI Press.

Mattocks, C., and Forbes, C. (2008). "A real-time, event-triggered storm surge forecasting system for the state of North Carolina." *Ocean Modelling*, 95-119.

Means, R.S. (2006) Means Square Foot Costs. http://rsmeans.reedconstructiondata.com/ Accessed 12 July 2011

Mendelsohn, R., Emanuel, K.; Chonabayashi, S. and Bakkensen, L. (2012). "The impact of climate change on global tropical cyclone damage." *Nature Climate Change* 2(3), 205-209.

Michener, W. K.; Blood, E. R.; Bildstein, K. L.; Btinson, M. M. and Gardner, L R. (1997) "Climate change, hurricanes and tropical storms, and rising sea level in coastal wetlands." *Ecological Applications*, (7),770-801

Mousavi, M., Irish, J., Frey, A., Olivera, F., and Edge, B. (2011). "Global warming and hurricanes: the potential impact of hurricane intensification and sea level rise on coastal flooding." *Climatic Change*, 575-597.

Nadal, N., Zapata, R., Pagan, I., Lopez, R., and Agudelo, J. (2010). "Building Damage due to Riverine and Coastal Floods." *Journal of Water Resources Planning and Management*, 327-336.

National Oceanic and Atmosphere Administration (2012a) The Coastal Change Analyses Program (C-CAP) http://www.csc.noaa.gov/digitalcoast/data/ccapregional Accessed 23 March 2011.

National Oceanic and Atmospheric Administration (2001) Preliminary Report: Hurricane Bret. http://www.nhc.noaa.gov/1999bret.html Accessed 05 January 2010.

National Oceanic and Atmospheric Administration (2011) NOAA Coastal Change Analysis Program (C-CAP) Regional Land Cover Database. Data collected 1995-present. Charleston, SC: National Oceanic and Atmospheric Administration (NOAA) Coastal Services Center. Data accessed at www.csc.noaa.gov/landcover. Accessed 5 March 2011.

National Oceanic and Atmospheric Administration (2012b) Atlantic basin hurricane database (HURDAT). http://www.aoml.noaa.gov/hrd/hurdat/ Accessed 08 July 2011.

National Oceanic and Atmospheric Administration (2012c) Historical Hurricane Tracks. http://www.csc.noaa.gov/hurricanes/# Accessed 23 January 2011.

National Oceanic and Atmospheric Administration (2012d) Tides and currents. http://tidesandcurrents.noaa.gov/ Accessed 15 July 2011.

National Research Council (2009). Mapping the zone: Improving flood map accuracy. The National Academy Press, Washington, District Columbia.

National Research Council, (1987) *Responding to changes in Sea Level: Engineering Implication*s. National Academy Press: Washington, District Columbia.

Ng, S., Wai, O., Li, Y., Li, Z., and Jiang, Y. (2009). "Integration of a GIS and a complex three-dimensional hydrodynamic, sediment and heavy metal transport numerical model." *Advances in Engineering Software*, 391-401.

Nicholls, R. and Cazenave, A. (2010). "Sea-Level Rise and Its Impact on Coastal Zones." *Science,* 328(5985), 1517-1520.

Park, J.; Obeysekera, J.; Irizarry, M.; Barnes, J.; Trimble, P. and Park-Said, W. (2011). "Storm surge projections and implications for water management in South Florida." *Climatic Change,* 107(1-2), 109-128.

Pfeffer, W. T.; Harper J. T.; O'Neel, S. (2008) "Kinematic Constrains on Glacier Contributions to 21st Century Sea Level Rise." *Science,* (321), 1340-1343

Rahmstorf, S. (2007) "A semi-empirical approach to projecting future sea level rise" *Science*, (315), 368-370.

Ratcliff, J. and Smith, J. M. (2011) "Sea level rise impacts to military installations in lower Chesapeake Bay" Proc*., Solutions to Coastal Disasters*, ASCE, Reston, Virginia, 740-752

Rego, J., and Li, C. (2010). "Storm surge propagation in Galveston Bay during Hurricane Ike." *Journal of Marine Systems*, 265-279.

Resio, D. and J. Westerink (2008). "Modeling the physics of storm surges." *Physics Today* 61(9): 33-38.

Resio, D. T.; Irish, J. L.; Westerink, J. J.; and Powell, N. (2012) "The effect of uncertainty on estimates of hurricane surge hazards" *Natural Hazards*, under review.

Resio, D.; Boc, S.; Borgman, L.; Cardone, V.; Cox, A. et al. (2007) "White paper on Estimating Hurricane Inundation Probabilities" White paper published by the U.S. Army Corps of Engineers Coastal & Hydraulics Laboratory, 125pp, Vicksburg, Mississippi.

Schiller, A. (2011). "The impact of a storm surge on business establishments in the Houston MSA." *Natural Hazards,* 56(1), 331-346.

Schneider, P. J. and Schauer, B. A. (2006). HAZUS---Its Development and Its Future. *Natural Hazards Review.* (7), 40-44.

Shepard, C.; Agostini, V. ; Gilmer, B.; Allen, T.; Stone, J.; and Brooks, W and Beck, M.W. (2012). "Assessing future risk: quantifying the effects of sea level rise on storm surge risk for the southern shores of Long Island, New York." *Natural Hazards,* 60(2), 727-745.

Smith, J., Cialone, M., Wamsley, T., and McAlpin, T. (2010). "Potential impact of sea level rise on coastal surges in southeast Louisiana." *Ocean Engineering*, 37-47.

Tanaka, S.; Bunya, S.; Westerink, J. J.; Dawson, C. and Luettich, R. A. (2011). "Scalability of an Unstructured Grid Continuous Galerkin Based Hurricane Storm Surge Model." *Journal of Scientific Computing*, 329-358.

Thompson, E. F. and Cardone, V. J. (1996) Practical modeling of hurricane surface wind field. *Journal of Waterway, Ports, Coastal and Ocean Engineering,* 122(4), 195-205.

Titus, J. G. (1990) "Greenhouse effect, sea level rise, and barrier islands: case study of. Long Beach Island, New Jersey". *Coastal Management,* (18)65-90.

Tsihrintzis, V., and Madiedo, E. (2000). "Hydraulic resistance determination in marsh wetlands." *Water Resources Management*, 285-309.

U. S. Army Corps of Engineers (2011) *Sea level change considerations for civil works programs.* Department of the Army, Washington, District of Columbia.

U.S. Census Bureau (2000) 2000 Census. http://www.census.gov/main/www/cen2000.html Accessed 13 August 2011.

U.S. Census Bureau (2010) 2010 Census. http://2010.census.gov/2010census/ Accessed 13 August 2011.

U.S. Fish and Wildlife Service (2012) 3) The National Wetlands Inventory (NWI) http://www.fws.gov/wetlands/ Accessed 04 May 2011.

USGS (2005) Hurricane Hazards: A National Threat. Fact Sheet. http://pubs.usgs.gov/fs/2005/3121/ Accessed 09 March 2011

U.S. Geological Survey (2011a) Gap Analysis Program (GAP). http://gapanalysis.usgs.gov/ Accessed 13 August 2011.

U.S. Geological Survey (2011b) The National Land Cover Dataset (NLCD) http://www.mrlc.gov/ Accessed 13 August 2011.

U. S. Geological Survey (2012) National Elevation Dataset. http://ned.usgs.gov/ Accessed 04 August 2011.

Vermeer, M. and Rahmstorf, S. (2009) "Global sea level linked to global temperatures" Proc., *National Academy of Sciences, Early Edition*, 6pp. National Academy Press: Washington, District of Columbia.

Vogelmann, J.E., S.M. Howard, L. Yang, C. R. Larson, B. K. Wylie, and J. N. Van Driel, (2001). "Completion of the 1990's National Land Cover Data Set for the

conterminous United States." *Photogrammetric Engineering and Remote Sensing,* (67) 650-662.

Wamsley, T.; Cialone, M.; Smith, J. M.; Atkinson, J. H. and Rosati, J. D. (2009). "Influence of landscape restoration and degradation on storm surge and waves in southern Louisiana." *Natural Hazards*, 207-224.

Wamsley, T.;Cialone, M.; Smith, J.M.; Ebersole, B.A. and Grzegorzewski, A. S. (2010). "The potential of wetlands in reducing storm surge." *Ocean Engineering*, 59-68.

Warner, N. N. and Tissot, P. E.(2012) "Storm flooding sensitivity to sea level rise for Galveston Bay, Texas" *Ocean Engineering*, (44), 23-32

Westerink, J., Luettich, R., Feyen, J., Atkinson, J., Dawson, C., Roberts, H., Powell, M., Dunion, J., Kubatko, E., and Pourtaheri, H. (2008). "A basin- to channel-scale unstructured grid hurricane storm surge model applied to southern Louisiana." *Monthly Weather Review*, 833-864.

Wilen, B. O. and Tiner, R. W. (1989) "The national wetlands inventory – The first 10 years" *Proc., Symposium on Wetlands: Concerns and successes*. American Water Resources Association, Bethesda, Maryland.

Wong, D., Camelli, F., and Sonwalkar, M. (2007). "Integrating computational fluid dynamics (CFD) models with GIS: An evaluation on data conversion formats." *Geospatial Information Science,* (1, 2), 75312-75312.

Wright D J, Blongewicz M J, Halpin P N, and Breman J (2007) *Arc Marine: GIS for a Blue Planet*. Redlands, California: ESRI Press.

Wu, S.; Yarnal, B. and Fisher, A. (2002). "Vulnerability of coastal communities to sea-level rise: a case study of Cape May County, New Jersey, USA." *Climate Research,* 22(3), 255-270.

Xu, H. Z., Zhang, K. Q., Shen, J. A., and Li, Y. P. (2010). "Storm surge simulation along the U.S. East and Gulf Coasts using a multi-scale numerical model approach." *Ocean Dynamics*, 60(6), 1597-1619.

Yu, F. J., Zhang, Z. H., and Lin, Y. H. (2001). "A storm surge numerical forecast system based on GIS", *Proc., XXIX International Association of Hydraulic Engineering and Research Congress.* Tsinghua University Press, Beijing.

Zerger, A., and Wealands, S. (2004). "Beyond modelling: Linking models with GIS for flood risk management*." Natural Hazards*, 191-208.

Zhang, Y. L., and Baptista, A. M. (2004). "Benchniarking a new open-source 3D circulation model (ELCIRC)." *Computational Methods in Water Resources*, Vols 1 and 2, C. T. Miller, M. W. Farthing, W. G. Gray, and G. F. Pinder, eds., 1791-1800.

APPENDIX A

GEODATABASE DICTIONARY

A-1: Arc StormSurge Feature Classes

Feature Classes				
{Feature Dataset}	[FeatureClass]	<Field Name>	Field Description	Type
Atmospheric	hurricaneEyePath	shape	point	geometry
		stormID	unique identifier	integer
		date	date and time of record	date
		fowardSpeed	hurricane speed	float
		centralPressure	hurricane central pressure	float
	hurricaneTrack	shape	line	geometry
		stormID	unique identifier	integer
		year	hurricane year of landfall	date
		category	hurricace Safir-Simpson category	integer
	WeatherStation	shape	point	geometry
		stationID	unique identifier	integer
		stationDescription	brief description	text
		source	data source	text
Coastal	Bathymetry	shape	point	geometry
		<xcoord>	point coordinate	float
		<ycoord>	point coordinate	float
		<zcoord>	elevation	float
	CoastalStation	shape	point	geometry
		StationID	unique identifier	integer
		Source	data source	text
		Name	station name	text
		Type	station type	text
		DateStart	initial time of monitoring	date
		DateEnd	end time of monitoring	date
	ShoreLine	shape	point	geometry
		source	data source	text
		date	date of surveying	date
		type	shoreline type	text

A-1: Continued

Feature Classes				
{Feature Dataset}	[FeatureClass]	<Field Name>	Field Description	Type
FEMMesh	MeshNode	shape	point	geometry
		nodeID	unique identifier	integer
		Bathymetry	elevation positive below MSL	float
		Elevation	elevation positive above MSL	float
		xcoord	point coordinate	float
		ycoord	point coordinate	float
	meshEdge	shape	line	geometry
		fromNodeID	unique identifier	integer
		toNodeID	unique identifier	integer
		size	edge length	float
	meshElement	shape	polygon	geometry
		node1	unique identifier	integer
		node2	unique identifier	integer
		node3	unique identifier	integer
		elementID	unique identifier	integer
		area	area of each element	float
	boundaryNode	shape	point	geometry
		nodeID	unique identifier	integer
		type	type of boundary	text
	boundaryLine	shape	line	geometry
		type	type of boundary	text
	meshDomain	shape	polygon	geometry
		area	domain area	float
		description	brief description	text
	island	shape	polygon	geometry
		islandID	unique identifier	integer
		area	each island area	float
	HPCsubdomains	shape	polygon	geometry
		domainID	unique identifier	integer
recording Points	stWaterLevel	shape	point	geometry
		pointID	unique identifier	integer
		description	brief description	text
		xcoord	point coordinate	float
		ycoord	point coordinate	float

A-1: Continued

Feature Classes				
{Feature Dataset}	[FeatureClass]	<Field Name>	Field Description	Type
recording Points	stVelocity	shape	point	geometry
		pointID	unique identifier	integer
		description	brief description	text
		xcoord	point coordinate	float
		ycoord	point coordinate	float
	stWaveDir	shape	point	geometry
		pointID	unique identifier	integer
		description	brief description	text
		xcoord	point coordinate	float
		ycoord	point coordinate	float
	stWaveHt	shape	point	geometry
		pointID	unique identifier	integer
		description	brief description	text
		xcoord	point coordinate	float
		ycoord	point coordinate	float
	stWaveP	shape	point	geometry
		pointID	unique identifier	integer
		description	brief description	text
		xcoord	point coordinate	float
		ycoord	point coordinate	float
	stAtmo	shape	point	geometry
		pointID	unique identifier	integer
		description	brief description	text
		xcoord	point coordinate	float
		ycoord	point coordinate	float
floodMap	floodArea	shape	polygon	geometry
		floodID	unique identifier	integer
		description	brief description	text
	floodZone	shape	polygon	geometry
		floodClass	zone classification	text
		area	area of each polygon	float
		floodID	unique identifier	integer
	crossSection	shape	line	geometry
		sectionID	unique identifier	integer

A-2: Arc StormSurge Table Sets

TABLE SETS				
{Table Set}	[Table]	<Field Name>	Field Description	Type
NodeParam	surfaceSubState	nodeID	unique identifier	integer
		value	parameter value	float
	z0Land	nodeID	unique identifier	integer
		value (x12)	parameter value	float
	surfaceCanopy	nodeID	unique identifier	integer
		value	parameter value	integer
	manningN	nodeID	unique identifier	integer
		value	parameter value	float
	seaHeight	nodeID	unique identifier	integer
		value	parameter value	float
	tau0	nodeID	unique identifier	integer
		value	parameter value	float
	eddy	nodeID	unique identifier	integer
		value	parameter value	float
	waveRefrac	nodeID	unique identifier	integer
		value	parameter value	float
Friction	nlcd	code	landcover code	integer
		description	landcover type description	text
		manningN	parameter value	float
		surfaceCanopy	parameter value	integer
		z0	parameter value	float
	cccap	code	landcover code	integer
		description	landcover type description	text
		manningN	parameter value	float
		surfaceCanopy	parameter value	integer
		z0	parameter value	float
	nwi	code	landcover code	integer
		description	landcover type description	text
		manningN	parameter value	float
		surfaceCanopy	parameter value	integer
		z0	parameter value	float
modelSetup	numericalSetup	runID	unique identifier	integer
		Nday	simulation duration	float
		DT	time step	float
		ICS	coordinate system	integer
		NRAMP	ramp	float

A-2: Continued

TABLE SETS				
{Table Set}	[Table]	<Field Name>	Field Description	Type
modelSetup	boundaryType	code	boundary code	integer
		description	boundary type description	text
model results	meshVelocity	nodeID	unique identifier	integer
		date	time step	date
		xcomp	velocity x component	float
		ycomp	velocity y component	float
		magnitude	total velocity	float
		dir	direction from north	float
	meshWater	nodeID	unique identifier	integer
		date	time step	date
		ws	water levels	float
	meshWind	nodeID	unique identifier	integer
		date	time step	date
		xcomp	velocity x component	float
		ycomp	velocity y component	float
		magnitude	total velocity	float
		dir	direction from north	float
	meshPressure	nodeID	unique identifier	integer
		date	time step	date
		p	pressure	float
	meshWaveDir	nodeID	unique identifier	integer
		date	time step	date
		dir	direction from north	float
	meshWaveHs	nodeID	unique identifier	integer
		date	time step	date
		hs	wave height	float
	meshWaveP	nodeID	unique identifier	integer
		date	time step	date
		wp	wave period	float
	pointVelocity	pointID	unique identifier	integer
		date	time step	date
		xcomp	velocity x component	float
		ycomp	velocity y component	float
		magnitude	total velocity	float
		dir	direction from north	float

A-2: Continued

TABLE SETS				
{Table Set}	[Table]	<Field Name>	Field Description	Type
model results	pointWater	pointID	unique identifier	integer
		date	time step	date
		ws	water levels	float
	pointWind	nodeID	unique identifier	integer
		date	time step	date
		xcomp	velocity x component	float
		ycomp	velocity y component	float
		magnitude	total velocity	float
		dir	direction from north	float
	pointPressure	pointID	unique identifier	integer
		date	time step	date
		p	pressure	float
	pointWaveDir	pointID	unique identifier	integer
		date	time step	date
		dir	direction from north	float
	pointWaveHs	pointID	unique identifier	integer
		date	time step	date
		hs	wave height	float
	pointWaveP	pointID	unique identifier	integer
		date	time step	date
		p	wave period	float
model Max	meshMAXVelocity	nodeID	unique identifier	integer
		xcomp	velocity x component	float
		ycomp	velocity y component	float
		magnitude	total velocity	float
		dir	direction from north	float
	meshMAXWater	nodeID	unique identifier	integer
		ws	water levels	float
	meshMAXWind	nodeID	unique identifier	integer
		xcomp	velocity x component	float
		ycomp	velocity y component	float
		magnitude	total velocity	float
		dir	direction from north	float
	meshMAXPressure	nodeID	unique identifier	integer
		p	pressure	float
	meshMAXWaveDir	nodeID	unique identifier	integer
		dir	direction from north	float

A-2: Continued

\{Table Set\}	[Table]	<Field Name>	Field Description	Type
TABLE SETS				
model Max	meshMAXWaveHs	nodeID	unique identifier	integer
		hs	wave height	float
	meshMAXWaveP	nodeID	unique identifier	integer
		p	wave period	float
	pointMAXVelocity	pointID	unique identifier	integer
		xcomp	velocity x component	float
		ycomp	velocity y component	float
		magnitude	total velocity	float
		dir	direction from north	float
	pointMAXWater	pointID	unique identifier	integer
		ws	water levels	float
	pointMAXWind	pointID	unique identifier	integer
		xcomp	velocity x component	float
		ycomp	velocity y component	float
		magnitude	total velocity	float
		dir	direction from north	float
	pointMAXPressure	pointID	unique identifier	integer
		p	pressure	float
	pointMAXWaveDir	pointID	unique identifier	integer
		dir	direction from north	float
	pointMAXWaveHs	pointID	unique identifier	integer
		hs	wave height	float
	pointMAXWaveP	pointID	unique identifier	integer
		p	wave period	float
	meshMAXDepth	pointID	unique identifier	integer
		depth	water depth	float

A-2: Continued

TABLE SETS				
{Table Set}	[Table]	<Field Name>	Field Description	Type
modelInput	tidesTB	date	time step	date
		ws	measured water level	float
	currentTB	date	time step	date
		xcomp	measured velocity x component	float
		ycomp	measured velocity y component	float
	waveHsTB	date	time step	date
		whs	measured wave heigth	float
	wavePTB	date	time step	date
		wp	measured wave period	float
	waveDirTB	date	time step	date
		wdir	measured wave direction	float
	windTB	date	time step	date
		xcomp	velocity x component	float
		ycomp	velocity y component	float
	pressureTB	date	time step	date
		p	pressure	float

A-3: Arc StormSurge Raster Sets

Raster Sets				
{Raster Set}	[Raster]	variable	description	Type
surfaces	surfWaterLevel	water level	raster catalog - model results	time aware raster catalog
	surWaterDepth	water depth	raster catalog - model results	time aware raster catalog
	surfWaveH	wave height	raster catalog - model results	time aware raster catalog
	surfWaveP	wave period	raster catalog - model results	time aware raster catalog
	surfMaxWaterLevel	max water level	maximum from simulation	
	surfMAXWaterDepth	max water depth	maximum from simulation	
	surfMAXWaveH	max wave height	maximum from simulation	
	surfMAXWaveP	max wave period	maximum from simulation	
surfparameter	surfSubState	Submergence state	geospatial parameter	
	surfz0Land	z0	geospatial parameter	
	surfCanopy	surface canopy	geospatial parameter	
	surfMan	manning's N	geospatial parameter	
	surfSea	sea surface	geospatial parameter	
	surfTau	tau 0	geospatial parameter	
	surfEddy	eddy viscosity	geospatial parameter	
	surfRefrac	wave refraction	geospatial parameter	
	meshResolution	average edge length	mesh resolution	

A-4: Arc StormSurge Relationship Classes

Relationship Classes				
|relationshipClass|	from [table]	to [featureclass]	<attribute>	Type
parameterToNode	surfaceSubState	meshNode	nodeID	one to one
	z0Land	meshNode	nodeID	one to one
	surfaceCanopy	meshNode	nodeID	one to one
	manningN	meshNode	nodeID	one to one
	seaHeight	meshNode	nodeID	one to one
	tau0	meshNode	nodeID	one to one
	eddy	meshNode	nodeID	one to one
	waveRefrac	meshNode	nodeID	one to one
resultsTomesh	meshVelocity	meshNode	nodeID	one to one
	meshWater	meshNode	nodeID	one to one
	meshWind	meshNode	nodeID	one to one
	meshPressure	meshNode	nodeID	one to one
	meshWaveDir	meshNode	nodeID	one to one
	meshWaveHs	meshNode	nodeID	one to one
	meshWaveP	meshNode	nodeID	one to one
resultsToPoint	stationVelocity	stwaterLevel	pointID	one to one
	stationWater	stVelocity	pointID	one to one
	stationWind & Pressure	stAtmo	pointID	one to one
	stationWaveDIR	stWaveDir	pointID	one to one
	stationWaveHt	stWaveHt	pointID	one to one
	stationWaveP	stWaveP	pointID	one to one
maxToMesh	meshMAXVelocity	meshNode	nodeID	one to one
	meshMAXWater	meshNode	nodeID	one to one
	meshMAXWind	meshNode	nodeID	one to one
	meshMAXPressure	meshNode	nodeID	one to one
	meshMAXWaveDir	meshNode	nodeID	one to one
	meshMAXWaveHs	meshNode	nodeID	one to one
	meshMAXWaveP	meshNode	nodeID	one to one

A-4: Continued

Relationship Classes				
|relationshipClass|	from [table]	to [featureclass]	\<attribute\>	Type
maxToPoint	pointMAXVelocity	stwaterLevel	pointID	one to one
	pointMAXWater	stVelocity	pointID	one to one
	pointMAXWind & Pressure	stAtmo	pointID	one to one
	pointMAXWaveDIR	stWaveDir	pointID	one to one
	pointMAXWaveHt	stWaveHt	pointID	one to one
	pointMAXWaveP	stWaveP	pointID	one to one
boundaryToCode	boundaryType	boundaryNode	code	one to one
dataToStation	{modelInput}	{Atmospheric} & {Coastal}	stationID	one to one

APPENDIX B

ARC STORM SURGE TOOLS

B-1: Arc StormSurge Tools

	Tool Name	Input	Output	Description
1	Create Arc StormSurge	---	ArcStormSurge.gdb	Creates a complete Arc StormSurge geodatabase with empty features classes
2	Import Nodes	\fort.14\	[meshNode]	Creates a point feature class and populates the fields <xcoord>, <ycoord>, <nodeID>, <bathymetry> and <elevation>
3	Import Edges	\fort.14\	[meshEdges]	Creates a line feature class and populates the <FromNodeID>, <ToNodeID>, and <Size>
4	Import Boundary Nodes	\fort.14\	[boundaryNode]	Creates a point feature class and populates the fields <NodeID> and <Type>
5	Create Elements	[meshNode] & [meshEdges]	[meshElements]	Creates a polygon feature class and populates the <Node1>, <Node2>, <Node3> (<NodeID> values of the nodes that form each element), <ElementID> and <Area>
6	Create Boundary Lines	[boundaryNode]	[boundaryLine]	Creates a line feature class based on the attribute <type>
7	Create Island Polygons	[boundaryNode]	[island]	Creates a polygon feature class based on the attribute <type> and assigns an <islandID>
8	Create Land Boundary	[boundaryNode]	[land]	Creates a line feature class based on the attribute <type>
9	Create domain	[meshNode]	[domain]	Creates a polygon feature class based on the mesh spatial domain
10	Update Bathymetry	\fort.14\ & [bathymetry]	\fort.14\	Updates the bathymetry values of an existing mesh

B-1: Continued

	Tool Name	Input	Output	Description
11	TIN to mesh	TIN	[meshNode], [meshEdges], [boundaryNode]	Extracts the TIN nodes to [meshNode], creates the [meshEdges] and the [boundayNodes]
12	Create Finite Element Mesh	[meshNode], [boundaryNode] and [meshElements]	\fort.14\	Creates a new mesh
13	Mesh Resolution	[meshEdges]	[meshResolution]	Creates a raster representing the average distance between the mesh nodes
14	Import Geospatial Parameters	\fort.13\	[surfaceSubState], [z0Land], [surfaceCanopy], [manningN], [seaHeight], [tau0], [eddy], [waveRefrac]	Populates the fields <nodeID> and <value> (surface submergence state, roughness directional length (12), eddy viscosity, wave refraction, surface canopy, manning's n, tau0, water surface above geoide)
15	Create Frictional Raster	[nodeParam], [meshNode] & |parametersToNode|	{surfParameter}	Creates a raster surface representing a spatial interpolation of any geospatial parameter
16	Friction to nodes	[landcover], {Friction} & [meshNode]	{nodeParam}	Runs the algorithm to extract frictional factors from land cover dataset and creates a table
17	Update fort.13	{nodeParam} & \fort.13\	\fort.13\	Updates an existing \fort.13\
18	Create \fort.13\	{nodeParam}	\fort.13\	Creates a new \fort.13\
19	Import Recording Points	\fort.15\	[stWaterLevel], [stVelocity], [stWaveDir], [stWaveHt], [stWaveP], [stAtmo]	Creates a point feature class and populates the attributes <pointID>, <description>, <xcoord> and <ycoord>

B-1: Continued

	Tool Name	Input	Output	Description
20	Update Recording Points	\fort.15\ & {recordingStations}	\fort.15\	Update an existing /fort.15/
21	Import Model Setup	\fort.15\	[numericalSettings]	populates the attributes <time step>, <coordinates>, <simulationtime>, <ramp>
22	Read HURDAT	\hurdatfile\	[hurricaneEyePath]	creates a point feature class and populates the <stormID>, <date>, <forwardSpeed> and <centralPressure> attributes
23	Create Track	[hurricaneEyePath]	[HurricaneTrack]	create a line feature class
24	Import Wind Pressure	\fort.221\ & \fort.222\	[windTB] & [pressureTB]	populates the [windTB] and [pressureTB] tables
25	Import Mesh Water Level	\fort.63\	[meshWater]	populates the <ws>, <date> and <nodeID> fields
26	Import Mesh Velocity	\fort.64\	[meshVelocity]	populates the <nodeID>, <date>, <xcomp>, <ycomp>, <magnitude> & <dir> fields
27	ImportMeshWave	\swan_DIR.63\	[meshWaveDir]	populates the <dir>, <date> and <nodeID> fields
28	ImportMeshWave	\swan_HS.63\	[meshWaveHs]	populates the <hs>, <date> and <nodeID> fields
29	ImportMeshWave	\swan_TM01.63\	[meshWaveP]	populates the <wp>, <date> and <nodeID> fields
30	ImportMeshAtmospheric	\fort.73\	[meshWind]	populates the <nodeID>, <date>, <xcomp>, <ycomp>, <magnitude> & <dir> fields
31	ImportMeshAtmospheric	\fort.74\	[meshPressure]	populates the <p>, <date> and <nodeID> fields
32	Import Point Water Level	\fort.61\	[meshWater]	populates the <ws>, <date> and <pointID> fields

B-1: Continued

	Tool Name	Input	Output	Description
33	Import Point Velocity	\fort.62\	[meshVelocity]	populates the <pointID>, <date>, <xcomp>, <ycomp>, <magnitude> & <dir> fields
34	Import Point Wave	\swan_fort.71\	[meshWaveDir]	populates the <dir>, <date> and <pointID> fields
35	Import Point Wave	\swan_fort.71\	[meshWaveHs]	populates the <hs>, <date> and <pointID> fields
36	Import Point Wave	\swan_fort.71\	[meshWaveP]	populates the <wp>, <date> and <pointID> fields
37	Import Point Atmospheric	\fort.71\	[meshWind]	populates the <pointID>, <date>, <xcomp>, <ycomp>, <magnitude> & <dir> fields
38	Import Point Atmospheric	\fort.72\	[meshPressure]	populates the <p>, <date> and <pointID> fields
39	Extract mesh MAX ws	[meshWater]	[meshMAXWater]	populates the <ws>, <date> and <nodeID> fields
40	Extract mesh MAX vel	[meshVelocity]	[meshMAXVelocity]	populates the <nodeID>, <date>, <xcomp>, <ycomp>, <magnitude> & <dir> fields
41	Extract mesh MAX whs	[meshWaveH]	[meshMAXWaveHs]	populates the <hs>, <date> and <nodeID> fields
42	Extract mesh MAX wp	[meshWaveP]	[meshMAXWaveP]	populates the <wp>, <date> and <nodeID> fields
43	Extract mesh MAX wind	[meshWind]	[meshMAXWind]	populates the <nodeID>, <date>, <xcomp>, <ycomp>, <magnitude> & <dir> fields
44	Extract mesh MAX pre	[meshPressure]	[meshMAXPressure]	populates the <p>, <date> and <nodeID> fields
45	Extract Point MAX ws	[stationWater]	[meshMAXWater]	populates the <ws>, <date> and <pointID> fields
46	Extract Point MAX vel	[stationVelocity]	[meshMAXVelocity]	populates the <pointID>, <date>, <xcomp>, <ycomp>, <magnitude> & <dir> fields

B-1: Continued

	Tool Name	Input	Output	Description
47	Extract Point MAX whs	[stationWaveHs]	[meshMAXWaveHs]	populates the \<hs>, \<date> and \<pointID> fields
48	Extract Point MAX wp	[stationWaveP]	[meshMAXWaveP]	populates the \<wp>, \<date> and \<pointID> fields
49	Extract Point MAX wind	[stationWind]	[meshMAXWind]	populates the \<pointID>, \<date>, \<xcomp>, \<ycomp>, \<magnitude> & \<dir> fields
50	Extract Point MAX pre	[stationPressure]	[meshMAXPressure]	populates the \<p>, \<date> and \<nodeID> fields
51	Calculate MAX water depth	[meshMAXWater]	[meshMAXDepth]	runs the depth calculation algorithm and populates \<nodeID> and \<depth>
52	Create Surface	[meshNode], |resultsTomesh|, |maxTomesh|, {modelResults}	[surfWaterLEvel], [surfWaterDepth], [surfWaveP], [surfMaxWaterLevel], [surfMAXWaterDepth], [surfMAXWaveH], [surfMAXWaveP]	creates surface rasters for a given variable and time step
53	Delineate Flood Polygons	[DEM], [meshMAXWater], [meshNode], |resultsTomesh|, [meshMAXdepth]	[floodArea]	runs the flooded areas algorithm and creates a polygon feature class
54	Classify flood zones	[floodArea], [meshMAXWaveHs], [meshNode], |resultTomesh|	[floodZone]	runs the flood zone classification algorithm and creates a polygon feature class

APPENDIX C

ARC STORMSURGE FIGURES
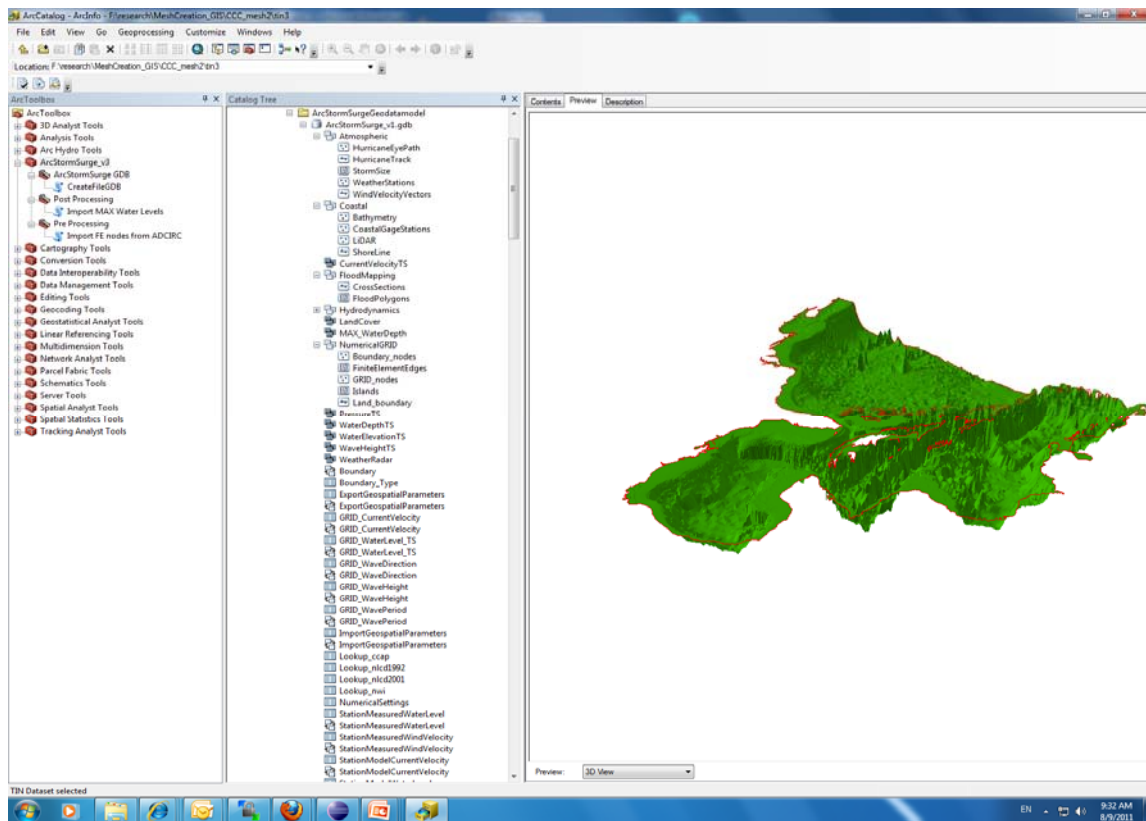
C-1: Arc StormSurge geodatabase in Arc Catalog
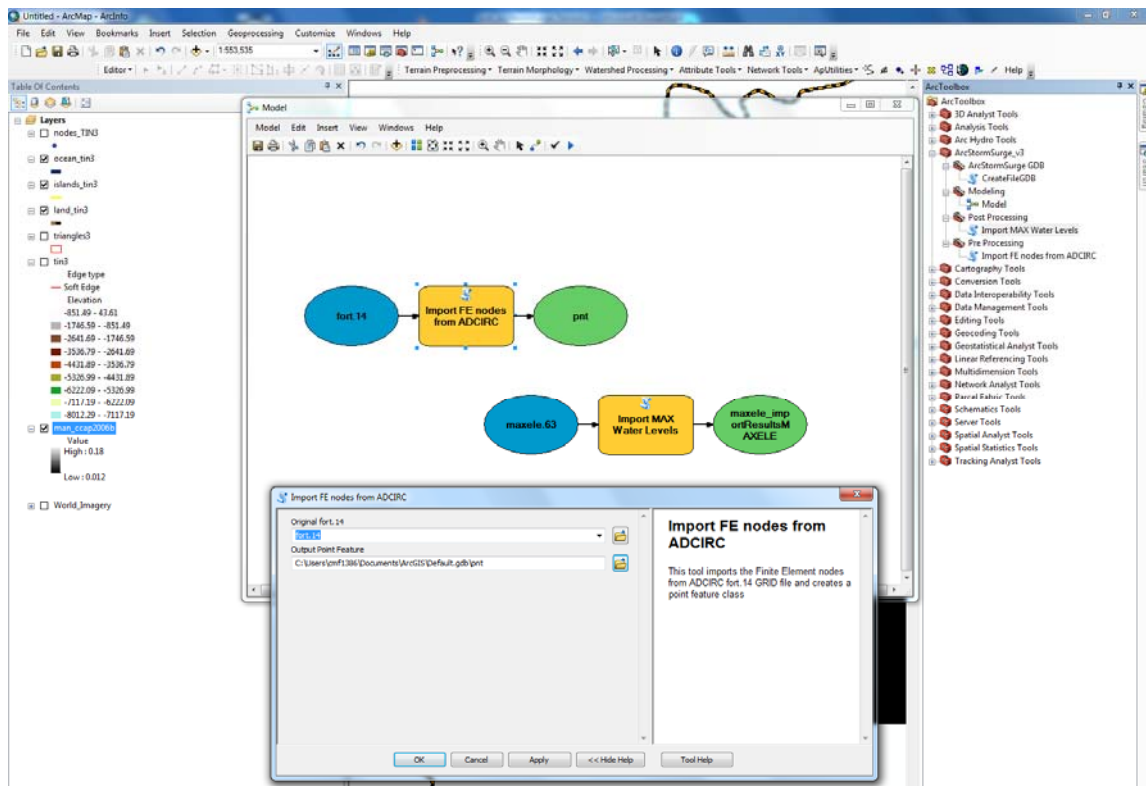
C-2: Arc StormSurge Tool interface in ArcGIS10.
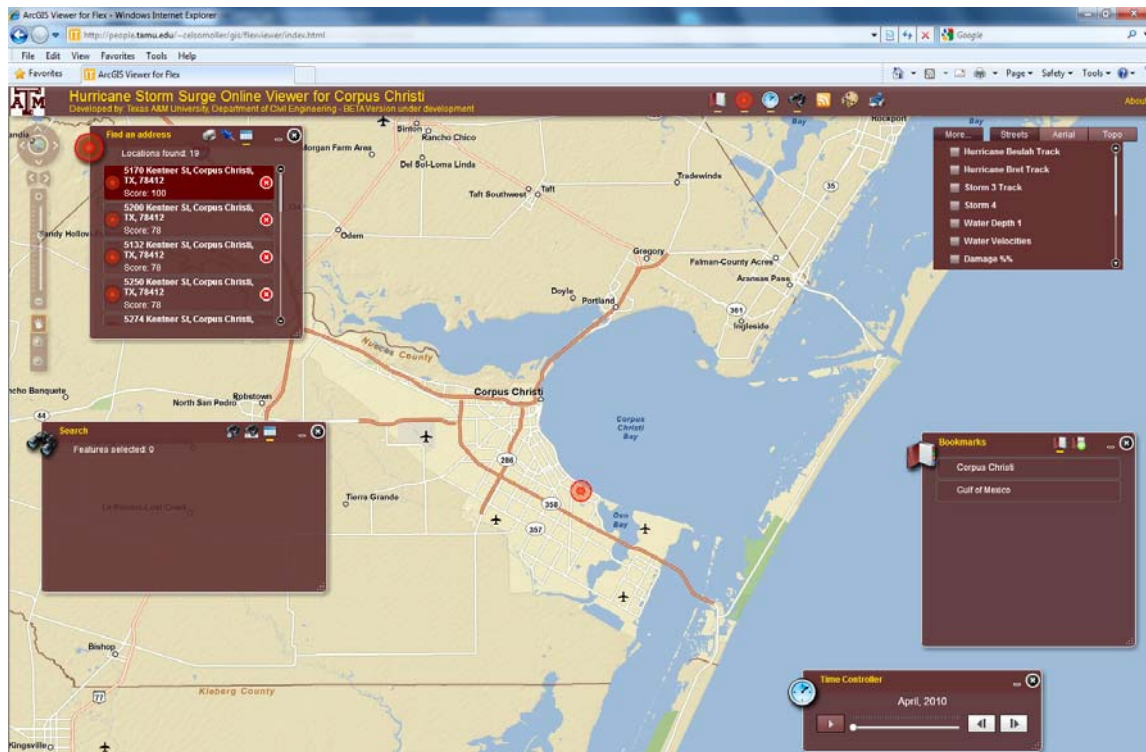
C-3: Example of web interface for publishing Arc StormSurge data.

APPENDIX D

LAND COVER CONVERSION PARAMETERS

D-1: Manning's *n* values, Surface Canopy coefficient and Z_0 coefficient for the C-CAP databases of 1996, 2001 and 2006. This study is equal to Dietrich *et al.*, 2011.

Class	Description	Manning's n	Surface Canopy	Z_0
2	High intensity developed	0.12	0	0.373
3	Medium intensity developed	0.12	0	0.373
4	Low intensity developed	0.12	0	0.373
5	Developed open space	0.035	1	0.055
6	Cultivated land	0.1	0	0.298
7	Pasture / hay	0.05	1	0.111
8	Grassland	0.035	1	0.055
9	Deciduous Forest	0.16	0	0.522
10	Evergreen forest	0.18	0	0.597
11	Mixed Forest	0.17	0	0.559
12	Scrub / shrub	0.08	0	0.223
13	Palustrine forested wetland	0.15	0	0.485
14	Palustrine scrub/shrub wetland	0.075	0	0.205
15	Palustrine emergent wetland	0.06	1	0.149
16	Estuarine forested wetland	0.15	0	0.485
17	Estuarine scrub/shrub wetland	0.07	0	0.186
18	Estuarine emergent wetland	0.05	1	0.111
19	Unconsolidated shore	0.03	1	0.037
20	Bare Land	0.03	1	0.037
21	Open Water	0.025	1	0.018
22	Palustrine aquatic bed	0.035	1	0.055
23	Estuarine aquatic bed	0.03	1	0.037

D-2: Manning's *n* values, Surface Canopy coefficient and Z_0 coefficient for the NLCD database of 1992.

Class	Description	This study			Atkinson, *et al.* (2011)	Wamsley, *et al.* (2010)	Bunia, *et al.* (2010).
		Manning's n	Surface Canopy	Z_0	Manning's n	Manning's n	Manning's n
11	open water	0.02	1	0.010	0.02	0.02	0.02
12	ice/snow	0.01	1	0.012	0.022		0.022
21	low residential	0.12	0	0.350	0.12	0.07	0.12
22	high residential	0.15	0	0.550	0.121	0.14	0.121
23	commercial	0.1	0	0.440	0.05	0.05	0.05
31	bare rock/sand	0.04	1	0.100	0.04	0.04	0.04
32	gravel pit	0.06	1	0.140	0.06		0.06
33	transitional	0.1	0	0.150	0.1		0.1
41	deciduous forest	0.16	0	0.550	0.16	0.12	0.16
42	evergreen forest	0.18	0	0.560	0.18	0.15	0.18
43	mixed forest	0.17	0	0.550	0.17	0.12	0.17
51	scrubland	0.07	0	0.100	0.07	0.05	0.07
61	orchard/vineyard	0.1	0	0.250	0.1	0.1	0.1
71	grassland	0.035	1	0.040	0.035	0.034	0.035
81	pasture	0.033	1	0.040	0.033	0.03	0.033
82	row crops	0.037	1	0.060	0.04	0.035	0.04
83	small grains	0.035	1	0.040	0.035	0.035	0.035
84	fallow	0.032	1	0.030	0.032	0.03	0.032
85	recreational grass	0.03	1	0.070	0.03	0.025	0.03
91	woody wetland	0.14	0	0.500	0.14	0.1	0.14
92	emergent herbaceous wetland	0.045	1	0.100	0.035	0.04	0.035
95	cypress forest	0.145	0	0.550	0.145	0.1	

D-3: Manning's *n* values, Surface Canopy coefficient and Z_0 coefficient for the NLCD database of 2001.

Class	Description	This study			ADCIRC (2012)
		Manning's n	Surface Canopy	Z_0	Manning's n
11	Open water	0.02	1	-0.000646	0.02
12	Perennial Ice/Snow	0.01	1	-0.037973	0.01
21	Open space	0.02	1	-0.000646	0.02
22	Low Intensity	0.05	1	0.111335	0.05
23	Medium Intensity	0.1	0	0.29797	0.1
24	High Intensity	0.15	0	0.484605	0.15
31	Barren land	0.09	0	0.260643	0.09
32	Unconsolidated shore	0.04	1	0.074008	0.04
41	Deciduous forest	0.1	0	0.29797	0.1
42	Evergreen forest	0.11	0	0.335297	0.11
43	Mixed forest	0.1	0	0.29797	0.1
51	Dwarf Scrub	0.04	1	0.074008	0.04
52	Scrub/shrub	0.05	1	0.111335	0.05
71	Grassland/Herbaceous	0.034	1	0.0516118	0.034
72	Sedge Herbaceous	0.03	1	0.036681	0.03
73	Lichens	0.027	1	0.0254829	0.027
74	Moss	0.025	1	0.0180175	0.025
81	Pasture / Hay	0.033	1	0.0478791	0.033
82	Cultivated crops	0.037	1	0.0628099	0.037
90	Woody wetlands	0.1	0	0.29797	0.1
91	Palustrine forested wetland	0.1	0	0.29797	0.1
92	Palustrine scrub/shrub	0.048	1	0.1038696	0.048
93	Estuarine forested wetland	0.1	0	0.29797	0.1
94	Estuarine scrub/shrub	0.048	1	0.1038696	0.048
95	Emergent herbaceous wetland	0.045	1	0.0926715	0.045
96	Palustrine emergent wetland	0.045	1	0.0926715	0.045
97	Palustrine emergent wetland	0.045	1	0.0926715	0.045
98	Palustrine aquatic bed	0.015	1	-0.0193095	0.015
99	Estuarine Aquatic bed	0.015	1	-0.0193095	0.015

D-4: Manning's *n* values, Surface Canopy coefficient and Z_0 coefficient for the NLCD database of 2006.

Class	Description	Manning's n	Surface Canopy	Z_0
11	open water	0.02	1	0.000
12	ice/snow	0.01	1	0.000
21	Developed, open space	0.05	1	0.111
22	Developed, Low Intensity	0.1	0	0.298
23	Developed, Medium Intensity	0.12	0	0.373
24	Developed, High Intensity	0.15	0	0.485
31	barren land(rock/sand/clay)	0.03	1	0.037
41	deciduous forest	0.16	0	0.522
42	evergreen forest	0.18	0	0.597
43	mixed forest	0.17	0	0.559
51	Dwarf Scrub	0.04	1	0.074
52	Shrub / Scrub	0.08	0	0.223
71	grassland / herbaceous	0.034	1	0.052
72	Sedge/Herbaceous	0.03	1	0.037
73	Lichens	0.027	1	0.025
74	Moss	0.025	1	0.018
81	pasture/hay	0.033	1	0.048
82	Cultivated crops	0.037	1	0.063
90	woody wetland	0.14	0	0.447
95	emergent herbaceous wetland	0.045	1	0.093

D-5: Manning's *n* values, Surface Canopy coefficient and Z_0 coefficient for the NWI database.

Class		Description	Manning's n	Surface Canopy	Z_0
	1	Upland	0.12	0	0.373
	2	Forested wetland	0.15	1	0.485
	3	Shrub wetland	0.07	1	0.186
	4	Palustrine marsh	0.055	0	0.130
	5	Bald cypress forest	0.16	0	0.522
	6	open water	0.022	1	0.007
	7	Floating vegetation	0.045	0	0.093
	8	Flats	0.035	1	0.055
	9	Impounded area	0.03	1	0.037
	10	Submerged vegetation	0.035	0	0.055
	12	Farmed wetland	0.035	1	0.055
	13	Estuarine Marsh	0.065	1	0.167
	14	Estuarine shrub	0.07	0	0.186
	16	Inundated margin	0.04	1	0.074
	17	Beach	0.03	1	0.037
	18	Oyster reef	0.065	1	0.167
	19	Algal vegetation	0.027	1	0.025
	20	Mangrove marsh	0.08	0	0.223

VITA

Celso Moller Ferreira is originally from Sao Paulo, Brazil. He received his Bachelor of Sciences degree in Civil Engineering with a major in Sanitary and Environmental Engineering from the Federal University of Santa Catarina in 2003. He has a Master's of Science degree in Environmental Engineering from the Federal University of Santa Catarina (2007) and a Masters of Engineering degree in Hydrology from the CEDEX in Spain (2006). Mr. Ferreira is now beginning his career as an Assistant Professor at George Mason University in the Civil, Environmental and Infrastructure Department. Mr. Ferreira can be reached at the Volgenau School of Engineering, Nguyen Engineering Building, 4400 University Dr., MSN 6C1, Fairfax, VA 22030. His email is cferrei3@gmu.edu.